

# CANMET

## REPORT 79-6

Canada Centre  
for Mineral  
and Energy  
Technology

Centre canadien  
de la technologie  
des minéraux  
et de l'énergie

### HEAT-AFFECTED-ZONE TOUGHNESS OF WELDED JOINTS IN MICRO-ALLOY STEELS

D.W.G. WHITE AND K. WINTERTON — EDITORS

ELLIOT LAKE LABORATORY  
CANMET, E.M.R.

NOV 27 1979

W. J. O'NEILL

MINERALS RESEARCH PROGRAM  
PHYSICAL METALLURGY RESEARCH LABORATORIES



Energy, Mines and  
Resources Canada

Énergie, Mines et  
Ressources Canada

JANUARY 1979



© Minister of Supply and Services Canada 1979

Available in Canada through

Authorized Bookstore Agents  
and other bookstores

or by mail from

Canadian Government Publishing Centre  
Supply and Services Canada  
Hull, Quebec, Canada K1A 0S9

CANMET  
Energy, Mines and Resources Canada,  
555 Booth St.,  
Ottawa, Canada K1A 0G1

or through your bookseller.

Catalogue No. M38-13/79-6

ISBN 0-660-10413-X

Canada:\$5.75

Other countries:\$6.90

Price subject to change without notice.

© Ministre des Approvisionnements et Services Canada 1979

En vente au Canada par l'entremise de nos

agents libraires agréés  
et autres librairies

ou par la poste au:

Centre d'édition du gouvernement du Canada  
Approvisionnement et Services Canada  
Hull, Québec, Canada K1A 0S9

CANMET  
Énergie, Mines et Ressources Canada,  
555, rue Booth  
Ottawa, Canada K1A 0G1

ou chez votre libraire.

Nº de catalogue M38-13/79-6

ISBN 0-660-10413-X

Canada:\$5.75

Hors Canada:\$6.90

Prix sujet à changement sans avis préalable.

HEAT-AFFECTED-ZONE TOUGHNESS OF WELDED

JOINTS IN MICRO-ALLOY STEELS

by

A.B. Rothwell<sup>1</sup>, J.T. McGrath<sup>2</sup>, A.G. Glover<sup>3</sup>,  
B.A. Graville<sup>3</sup> and G.C. Weatherly<sup>4</sup>

Edited and compiled

by

D.W.G. White\* and K. Winterton\*\*

CANMET REPORT 79-6

MINERALS RESEARCH PROGRAM

PHYSICAL METALLURGY RESEARCH LABORATORIES

---

<sup>1</sup>Noranda Research Centre (now with AGTL)

<sup>2</sup>Canadian Welding Development Institute (now with CANMET)

<sup>3</sup>Canadian Welding Development Institute

<sup>4</sup>Department of Metallurgy & Material Sciences, University of Toronto

---

\*Manager, MDL, \*\*Section Head, Physical Metallurgy Research Laboratories,  
CANMET, Energy, Mines and Resources, Canada, Ottawa

## FOREWORD

The work presented in this report is the result of a 3-year contract funded through the Minerals Research Program of the Canada Centre for Mineral and Energy Technology (CANMET). The topic was inspired by the then Physical Metallurgy Sub-Committee of the National Advisory Committee on Mining and Metallurgical Research, a committee structure drawn from industry and the universities, which evaluates and comments on CANMET's R and D policies and programs.

Noranda Research Centre jointly with Dominion Bridge Co. Ltd. responded to the original call for proposals. In the first phase of the work, the expertise of the Canadian Welding Development Institute was co-opted, and its resources were drawn on again in later stages of the contract. At this time, work on electron microscopy was subcontracted to the University of Toronto.

In the realm of physical metallurgy at CANMET, this has been a pioneering experience whose success is largely attributable to the spirit of cooperation which pervaded the work from the start. May we hope it proves an augury for the future.

The format of this CANMET report reflects two facts. First, that the final report from the principals was delivered in five separate sections at different times during 1978. Second, in collating these separate reports into a single CANMET report, effort has been made to minimize delays in editorial treatment and printing so that the report can be distributed while its results remain topical. Thus, the format of five sections has been preserved and presented as four self-contained "chapters" - each, for example, with its own introduction, tables and figures - plus an appendix. Essentially, editorial treatment has been limited to rewriting the introduction to Part I, and to rendering the sections consistent in pagination, enumeration and, in places, style.

D.W.G. White

K. Winterton

Scientific Authorities for

Contract OSQ77-00055

Ottawa, February 1979



## AVANT-PROPOS

Le travail présenté dans ce rapport est le fruit d'un contrat de trois ans accordé par le Programme de recherche sur les minéraux du Centre canadien de la technologie des minéraux et de l'énergie (CANMET). Le sujet a été suggéré par l'ancien Sous-comité sur la métallurgie physique du Comité consultatif national sur la recherche métallurgique et minière dont les membres proviennent de l'industrie et des universités et ont comme tâche d'évaluer et de critiquer les politiques et les programmes de R et D du CANMET.

Le Centre de recherche Noranda en coopération avec le Dominion Bridge Co. Ltd. ont répondu à l'appel d'offre. A la première étape des travaux, les spécialistes de l'Institut canadien de développement de la soudure ont été cooptés ainsi que dans des étapes subséquentes du contrat. A ce moment, les travaux au microscopique électronique avaient été sous-traités par l'Université de Toronto.

Dans le domaine de la métallurgie physique à CANMET, le succès de cette première expérience est principalement dû à l'esprit d'équipe qui a régné depuis le début du projet. Espérons qu'il s'agit là d'un augure pour les travaux futurs.

Le format de ce rapport CANMET reflète deux points importants. Premièrement, le rapport définitif a été expédié en cinq sections séparées à différents temps durant 1978. Deuxièmement, en collationnant tous les rapports séparés en un seul rapport CANMET, l'auteur a tenté d'accélérer les processus de rédaction et de tirage pour que ce rapport soit acheminé au moment où les données sont pertinentes. Les cinq sections sont donc présentées en quatre chapitres indépendants, chacun comprenant une introduction, des tableaux et des figures, et un annexe. Les fonctions de correction ont essentiellement été limitées à réécrire la partie I et à assurer l'uniformité du numérotage des pages, les énumérations et, à certains endroits, du style.

D.W.G. White

K. Winterton

Autorités scientifiques pour

Contrat OSQ77-00055

Ottawa, février 1979

HEAT-AFFECTED-ZONE TOUGHNESS OF WELDED JOINTS IN  
MICRO-ALLOY STEELS

by

A.B. Rothwell, J.T. McGrath, A.G. Glover,  
B.A. Graville and G.C. Weatherly\*

ABSTRACT

The principal objective of this work was to evaluate the effect of chemical composition and cooling rate on the notch toughness of the heat-affected-zone of welded micro-alloy (HSLA) steel plate. Limited work was carried out on the effect of stress relieving heat treatment on notch toughness. Specimens were prepared by making submerged arc welds over a range of heat inputs on HSLA steel plates containing various amounts of niobium, vanadium and molybdenum.

The notch toughness of the heat-affected-zone was measured on precracked specimens as a function of temperature by the instrumented Charpy impact test. Tests recorded the initiation of fracture in terms of load and time over a temperature range that covered the transition from ductile to brittle fracture.

Because toughness is related to microstructure, the heat-affected-zone microstructures of specimens were identified. To help in evaluating the microstructures, continuous cooling transformation diagrams were established for all steel compositions.

The results indicate that for submerged arc welding, cooling times between 800 and 500°C of 40 seconds or less do not give rise to toughness-related problems in the heat-affected-zone of single pass welds in typical micro-alloy steels. In this range of cooling rates, toughness increases with increasing rate. The associated microstructural characteristics are fine prior austenite grain size leading to small bainite colony size and an absence of coarse lath boundary carbides or martensite/austenite particles. In practice, a cooling time of 40 seconds corresponds approximately to a heat input of 2.4 kJ/mm in a 12-mm plate or more than 8 kJ/mm in a 50-mm plate.

Higher heat inputs result in cooling times of more than 40 seconds. The heat-affected-zone toughness suffers, and at the same time precipitated micro alloy carbides and nitrides are detectable in the microstructure. Loss of toughness in niobium-containing steels stress relieved after welding appears to be particularly serious.

---

\*For author affiliations see inside title page

# RESISTANCE DE LA ZONE AFFECTEE THERMIQUEMENT DES ARTICULATIONS SOUDEES DANS LES ACIERS MICRO-ALLIES

par

A.B. Rothwell, J.T. McGrath, A.G. Glover,  
B.A. Graville and G.C. Weatherly\*

## RESUME

Le but principal de cette étude était d'évaluer l'effet de la composition chimique et de la vitesse de refroidissement sur la résistance à l'entaille de la zone thermiquement affectée d'une plaque soudée d'acier micro-allié. Des travaux de base ont été effectués sur les effets du traitement thermique de relaxation des contraintes sur la résistance à l'entaille. Les éprouvettes sont préparées en effectuant des soudures à l'arc submergées à toute une gamme de température sur les plaques d'acier faiblement allié à haute résistance ayant des teneurs variées de niobium, de vanadium et de molybdène.

La résistance à l'entaille, en fonction de la température, d'une zone thermiquement affectée a été déterminée sur des éprouvettes fendues d'avance par les essais sur l'impact de Charpy. Les essais ont permis d'enregistrer l'amorçage de la rupture en rapport avec la charge et le temps sur une gamme de température couvrant la transition de l'étape de rupture ductile à l'étape de rupture casante.

Comme la résistance correspond à la microstructure, les microstructures des zones thermiquement affectées ont été identifiées. Afin de faciliter l'évaluation des microstructures, des diagrammes de transformation du refroidissement continu ont été déterminés pour toutes les compositions de l'acier.

Les résultats indiquent que, pour la soudure à l'arc submergée, les temps de refroidissement de 40 secondes ou moins entre 800 et 500°C ne créent pas de problèmes de résistance dans la zone thermiquement affectée du soudage en une passe dans les aciers micro-alliés typiques. Dans cette gamme de vitesse de refroidissement, la résistance augmente en rapport direct avec la vitesse de refroidissement. La microstructure correspondante est caractérisée de grains de fine dimension précédant l'austénite suivis de colonies de bainite de petite dimension et une absence de carbures de limite grossiers ou de particules martensite/austénite. En pratique, un temps de refroidissement de 40 secondes correspond approximativement à une admission de chaleur de 2.4 kJ/mm dans une plaque de 12 mm et de plus de 8 kJ/mm dans une plaque de 50 mm.

On peut obtenir une plus grande admission de chaleur lorsque les temps de refroidissement sont de plus de 40 secondes. La résistance de la zone thermiquement affectée en souffre et au même moment, les carbures et les nitrides micro-alliés précipités sont décelables dans la microstructures. La perte de résistance des aciers à teneur de niobium ayant subis une relaxation des contraintes après le soudage semble être particulièrement sérieuse.

---

\*Consulter la page couverture pour les affiliations des auteurs



## CONTENTS

	<u>Page</u>
FOREWORD .....	i
AVANT-PROPOS .....	ii
ABSTRACT .....	iii
RESUME .....	iv
PART I: RESULTS OF INSTRUMENTED IMPACT TESTS .....	1
Introduction .....	1
Experimental details .....	1
Materials .....	1
Welding, heat treatment and testpiece preparation .....	1
Instrumented impact testing .....	3
Results and discussion .....	5
As-welded condition .....	5
Stress-relieved condition .....	7
Conclusions .....	8
Acknowledgements .....	8
References .....	8
PART II: CONTINUOUS-COOLING TRANSFORMATION CHARACTERISTICS ...	9
Introduction .....	9
Experimental details .....	9
Results and discussion .....	11
Conclusions .....	34
Acknowledgements .....	35
References .....	35
PART III - SECTION "A": METALLOGRAPHIC ANALYSIS OF HAZ	
MICROSTRUCTURES .....	37
Introduction .....	37
Experimental .....	37
Metallographic analysis .....	37
Materials .....	37
Metallographic techniques .....	37
COD fracture toughness testing .....	38
Results .....	39
Metallographic analysis .....	39
Stress-relieved HAZ structures .....	53
COD fracture toughness data .....	64
Summary of results .....	65
Acknowledgements .....	66
References .....	66
PART III - SECTION "B": PRECIPITATION EFFECTS .....	67
Introduction .....	67
Experimental procedure .....	68
Results .....	68
Discussion .....	72
Acknowledgements .....	78
References .....	78

## CONTENTS (cont'd.)

	<u>Page</u>
PART IV: GENERAL DISCUSSION .....	79
Introduction .....	79
Discussion .....	79
Dilatometry .....	79
Toughness, hardness and microstructure in as-welded and stress-relieved HAZ's .....	83
Summary of microstructural effects .....	90
General conclusions .....	91
References .....	91
APPENDIX A - INSTRUMENTED IMPACT TRANSITION CURVES .....	93

## TABLES

I-1	Composition of experimental steels, wt % .....	2
I-2	Welding parameters .....	2
I-3	Yield-load transition temperature, as-welded condition .....	5
I-4	Yield-load transition temperature, stress-relieved condition .....	8
II-1	Ac <sub>1</sub> and Ac <sub>3</sub> temperatures for experimental steels .....	12
II-2	Microstructure of dilatometer samples .....	31
III-1	Compositions of experimental steels, wt % .....	38
III-2	Welding parameters .....	38
III-3	Prior austenite grain size .....	39
III-4	HAZ constituents in weldments subjected to cooling rate I .....	48
III-5	Maximum HAZ hardness of stress-relieved welds .....	64
III-6	COD results for heat-affected zone .....	65
III-7	Ductile/brittle transition temperature .....	65
III-8	Samples examined for microalloy precipitation .....	68

## FIGURES

I-1	Details of testpiece preparation - schematic .....	3
I-2	Typical oscillograms: steel A, 2.4 kJ/mm .....	4
I-3	Typical fracture transition curve .....	5
I-4	Variation of yield load fracture transition temperature with cooling time (800-500°C), steels A-D .....	6
I-5	Variation of yield load fracture transition temperature with cooling time (800-500°C), steels E-H .....	6
I-6	Effect of niobium on yield load fracture transition temperature, as-welded condition .....	7
I-7	Effect of niobium and stress-relief on yield load fracture transition temperature .....	7

## CONTENTS (cont'd.)

	<u>Page</u>
II-1 Thermal cycles used in dilatometric investigation ....	10
II-2 Typical dilatometric curve and construction for obtaining percentage transformation .....	11
II-3 Continuous-cooling transformation diagram, steel A ...	12
II-4 Continuous-cooling transformation diagram, steel B ...	12
II-5 Continuous-cooling transformation diagram, steel C ...	12
II-6 Continuous-cooling transformation diagram, steel D ...	13
II-7 Continuous-cooling transformation diagram, steel E ...	13
II-8 Continuous-cooling transformation diagram, steel F ...	13
II-9 Continuous-cooling transformation diagram, steel G ...	13
II-10 Continuous-cooling transformation diagram, steel H ...	13
II-11 Optical micrographs, steel A, cooling rates I-V nital etch, x200 .....	15
II-12 Optical micrographs, steel A, cooling rates I-V picral etch, x1000 .....	16
II-13 Optical micrographs, steel B, cooling rates I-V nital etch, x200 .....	17
II-14 Optical micrographs, steel B, cooling rates I-V picral etch, x1000 .....	18
II-15 Optical micrographs, steel C, cooling rates I-V nital etch, x200 .....	19
II-16 Optical micrographs, steel C, cooling rates I-V picral etch, x1000 .....	20
II-17 Optical micrographs, steel D, cooling rates I-V nital etch, x200 .....	21
II-18 Optical micrographs, steel D, cooling rates I-V picral etch, x1000 .....	22
II-19 Optical micrographs, steel E, cooling rates I-V nital etch, x200 .....	23
II-20 Optical micrographs, steel E, cooling rates I-V picral etch, x1000 .....	24
II-21 Optical micrographs, steel F, cooling rates I-V nital etch, x200 .....	25
II-22 Optical micrographs, steel F, cooling rates I-V picral etch, x1000 .....	26
II-23 Optical micrographs, steel G, cooling rates I-V nital etch, x200 .....	27
II-24 Optical micrographs, steel G, cooling rates I-V picral etch, x1000 .....	28
II-25 Optical micrographs, steel H, cooling rates I-V nital etch, x200 .....	29
II-26 Optical micrographs, steel H, cooling rates I-V picral etch, x1000 .....	30
II-27 Effect of chemical composition (niobium, vanadium, molybdenum) on transformation temperatures .....	32
II-28 Variation of hardness with cooling time (800-500°C), steels A-D .....	33
II-29 Variation of hardness with cooling time (800-500°C), steels E-H .....	33



## CONTENTS (cont'd.)

	<u>Page</u>
II-30 Variation of hardness with 50% transformation temperature .....	34
III-1 Optical micrographs, steel A heat-affected-zone, cooling rates I-V, nital etch, x500 .....	40
III-2 Optical micrographs, steel A heat-affected-zone, cooling rates I-V, picral etch, x2000 .....	41
III-3 Optical micrographs, steel B heat-affected-zone, cooling rates I-V, nital etch, x500 .....	42
III-4 Optical micrographs, steel B heat-affected-zone, cooling rates I-V, picral etch, x2000 .....	43
III-5 Optical micrographs, steel C heat-affected-zone, cooling rates I-V, nital etch, x500 .....	44
III-6 Optical micrographs, steel C heat-affected-zone, cooling rates I-V, picral etch, x2000 .....	45
III-7 Optical micrographs, steel D heat-affected zone, cooling rates I-V, nital etch, x500 .....	46
III-8 Optical micrographs, steel D heat-affected-zone, cooling rates I-V, picral etch, x2000 .....	47
III-9a High dislocation density in the heat-affected-zone of steel D, TEM, x21 500 .....	49
III-9b Bainitic structure in the heat-affected-zone of steel A, TEM, x21 500 .....	49
III-10 Cleavage cracks on fracture surface of heat-affected-zone .....	50
III-11 Cleavage cracks cutting across a bainite colony on a fracture surface of a simulated HAZ structure .....	51
III-12 Optical micrographs, steel E heat-affected-zone, cooling rates I-V, nital etch, x500 .....	52
III-13 Optical micrographs, steel E heat-affected-zone, cooling rates I-V, picral etch, x2000 .....	54
III-14 Optical micrographs, steel F heat-affected-zone, cooling rates I-V, nital etch, x500 .....	55
III-15 Optical micrographs, steel F heat-affected-zone, cooling rates I-V, picral etch, x2000 .....	56
III-16 Optical micrographs, steel G heat-affected-zone, cooling rates I-V, nital etch, x500 .....	57
III-17 Optical micrographs, steel G heat-affected-zone, cooling rates I-V, picral etch, x2000 .....	58
III-18 Optical micrographs, steel H heat-affected-zone, cooling rates I-V, nital etch, x500 .....	59
III-19 Optical micrographs, steel H heat-affected-zone, cooling rates I-V, picral etch, x2000 .....	60
III-20 Twinned martensite within elongated martensite-austenite particles, steel H heat-affected-zone, cooling rate V, TEM, x34 000 .....	61
III-21 Carbide precipitates in heat-affected-zone structure, stress-relieved at 620°C, optical micrographs, picral etch, x2000 .....	62
III-22 Carbide precipitates in heat-affected-zone structure, stress-relieved at 620°C, optical micrographs, picral etch, x2000 .....	63

## CONTENTS (cont'd.)

	<u>Page</u>
III-23 Results of microhardness (200-g load) traverses on welds in steels A to H. Weld energy input was 2.4 kJ/mm, all welds stress-relieved at 620°C for one hour ....	64
III-24 Illustrating the effect of increasing etching time on the extraction of fine NbC particles - base plate D (x55 500) .....	69
III-25 Comparing the size and distribution of NbC particles in: (a) the base plate, dark field micrograph g = (111); and (b) the coarse grained HAZ. (NbC sample D 112), (x55 500) .....	70
III 26 Fine distribution of NbC particles in samples B150, C150 and D150 .....	71
III-27 Very fine distribution of V (C,N) particles in sample E150; particles size $\sqrt{40A}$ , (x111 000) .....	73
III-28 Comparison of low magnification and high magnification shots of same area of sample C112, (x55 500) .....	74
III-29 Distribution of coarse and fine NbC particles in samples C60 and D60 (x21 500) .....	75
III-30 Fine distribution of NbC in sample N-D III .....	76
III-31 Distribution of NbC in stress-relieved samples, (x55 500) .....	77
IV-1 Microstructures of dilatometer samples and weld HAZ's, steel B, x200 .....	80,81
IV-2a Hardness of dilatometer samples as a function of 50% transformation temperature, steels A-D .....	82
IV-2b Hardness of dilatometer samples as a function of 50% transformation temperature, steels E-H .....	82
IV-3 Hardness increment due to microalloying additions as a function of 50% transformation temperature .....	83
IV-4a Hardness of weld HAZ as a function of 50% transformation temperature, steels A-D .....	84
IV-4b Hardness of weld HAZ as a function of 50% transformation temperature, steels E-H .....	84
IV-5 Microhardness results (200 g) for four steels after stress relief at 510°C and 675°C .....	84
IV-6 Microhardness (200 g) results for all steels in the as-welded condition for the 2.4 kJ/mm heat input at cooling time (800-500°C) of 39 s .....	85
IV-7 Effect of stress-relief temperature on hardness .....	86
IV-8 Plot of transition temperature shift against hardness increase relative to steel "A" .....	87
IV-9 Plot of transition temperature shift against hardness increase relative to steel "A" .....	88
IV-10 Plot of transition temperature shift against hardness increase in stress-relieved welds relative to as-welded values; 2.4 kJ/mm welds and microhardness (200 g) values .....	89
IV-11 As welded HAZ macrohardness relative to steel "A" as a function of cooling time between 800-500°C .....	89
IV-12 Schematic illustration of effects of microstructural parameters on HAZ toughness .....	91

## PART I: RESULTS OF INSTRUMENTED IMPACT TESTS

by

A.B. Rothwell\*

Introduction

The principal objective of this three-year program has been to determine the notch toughness of the heat-affected-zone (HAZ) of weldments in micro-alloy steels, and to relate these data to microstructure. Notch toughness was determined by instrumented Charpy tests carried out on pre-cracked specimens over a range of temperatures so as to identify the ductile-brittle transition temperature. The data are given in the appendix, Part V, and are discussed in Part I. Microstructures have been examined by optical and electron microscope with results that are given in Part III.

This experimental program was carried out on a five by eight matrix of specimens - five heat inputs to simulate cooling rates characteristic of welding applied to steel plate of eight different compositions.

To illumine analysis of the results, continuous cooling transformation diagrams for all eight steels were determined by high speed dilatometry. This work is presented in Part II.

This is the core body of data, but it has been reinforced by selected work on the effect of stress relief heat treatments and by some COD tests. The effect of heat treatment on HAZ notch toughness is presented in Part I and the effect of strain rate as revealed by the COD test, is discussed in Part III.

The whole is "pulled together" in a comprehensive synthesis given in Part IV.

In this, Part I, experimental procedures on weld preparation, heat treatment and instrumented impact testing are presented, and results of the impact tests discussed.

Experimental detailsMaterials

Composition of the eight experimental steels that were melted and rolled by CANMET are shown in Table I-1. As may be seen, these are a plain carbon-manganese steel (A), three steels with increasing levels of niobium (B-D), two vanadium steels with and without niobium (E,F), and two molybdenum steels with different niobium levels (G,H); the base composition was essentially constant throughout. Three 12.7-mm plates and one 25.4-mm plate were received from each heat. Tensile tests were carried out on one plate of each thickness for each steel. According to thickness and chemical composition, the mechanical properties were typical for such steels, i.e., 350-500 MPa yield strength for the micro-alloyed steels.

Welding, heat treatment and testpiece preparation

Welds were deposited transversely to the rolling direction using the submerged-arc process. Welding parameters, energy inputs and measured cooling times from 800 to 500°C are shown in Table I-2. It is apparent that the cooling conditions studied ( $t_{500}^{800}$  from 6.5 to 160 s) cover a large portion of the range associated with practical welding operations. For the highest heat input, butt welds were made between an experimental plate and a mild steel plate using a backing bar. Lower heat-input welds were deposited in grooves on the experimental plates. Thermal cycles were measured by plunging platinum-platinum/rhodium thermocouples into the fusion zone. It is generally accepted that a single measurement of this sort is sufficient to establish the thermal characteristics of a weld,

---

\*Noranda Research Centre, Pointe Claire, Quebec.



Table I-1 - Composition of experimental steels, wt %

Code	C	Mn	Si	Al	S	P	Nb	V	Mo
A	0.095	1.27	0.175	0.038	<0.005	0.008	-	-	-
B	0.095	1.27	0.175	0.038	<0.005	0.008	0.034	-	-
C	0.085	1.31	0.25	0.044	<0.005	0.009	0.09	-	-
D	0.085	1.31	0.25	0.44	<0.005	0.009	0.14	-	-
E	0.08	1.26	0.235	0.017	0.005	0.007	-	0.09	-
F	0.08	1.26	0.235	0.017	0.005	0.007	0.042	0.09	-
G	0.075	1.34	0.23	0.054	<0.005	0.008	0.05	-	0.31
H	0.075	1.34	0.23	0.054	<0.005	0.008	0.095	-	0.31

Table I-2 - Welding parameters

Code	Current (A)	Voltage (V)	Speed (mm/min)	Energy input (kJ/mm)	Cooling time (800-500°C, s)
150	750	34	203	7.5 (12-mm plate)	160
112	500	30	203	4.4 (12-mm plate)	80
60	600	30	456	2.4 (12-mm plate)	39
36	460	26	510	1.4 (12-mm plate)	16
30	460	26	610	1.2 (25-mm plate)	6.5

due allowance being made for the variation in peak temperature with distance from the fusion boundary. Samples for metallography and hardness determinations were cut from each weld.

Additional welds prepared from all eight steels with a heat input of 2.4 kJ/mm, were subjected to stress-relief heat treatment at a nominal soaking temperature of 620°C. The furnace temperature was controlled by a cam to simulate a thermal cycle typically experienced in practice by a full-scale weldment. Heating time was approximately four hours, soaking time one hour and cooling time eight hours to  $\sqrt{250^\circ\text{C}}$ . Samples from steels A, C, F and G welded with the same heat input, were also stress-relieved at nominal temperatures of 510°C and 675°C, following the same procedure. As a result of some irregularities in furnace operation, the three soaking temperatures were found in practice to be 600°C, 500°C and 680°C.

Charpy blanks, longer than normal, were machined from all weldments transversely to the weld line. To facilitate location of the notch, blanks were chemically polished by swabbing with an HF-H<sub>2</sub>O<sub>2</sub> solution, followed by etching in 2% nital to reveal the weld and HAZ structure. A line 2 mm below the testpiece surface was scribed using a height gauge. Location of the notch itself was scribed by hand, under a binocular microscope, in such a way that the tip of a 2 mm notch would lie in the heat-affected-zone, adjacent to the fusion boundary. Notches 0.15 mm wide were cut using high-speed grinding wheels in a machine built for the purpose. Notch depth was originally 1.5 mm but was later reduced to 1.25 mm to allow more distance for the establishment of a straight, uniform fatigue-crack front. Several testpieces could be notched simultaneously after individual alignment of the scribe marks; testpieces were finally cut to length

after notching.

Notch position was progressively improved over the course of the program, as evidenced by the increasing proportion of testpiece blanks from each batch judged to be acceptable for testing, and by the generally reduced degree of scatter in the final results.

The notches were extended to 2 mm by fatigue cracking. The testpieces produced during the year ending March 31, 1977 were pre-cracked using a Dynatup fatigue machine, whereas those tested in the year ending March 31, 1978 were fatigued on a ManLabs FCM 300 machine. In each case, the stress intensity range was  $17-22 \text{ MPa m}^{1/2}$  and the progress of the crack was examined at a magnification of 200-500x on a surface polished on 600 grit abrasive paper. Despite the fact that the Dynatup machine cracks eight testpieces simultaneously, the ManLabs machine was preferred for the present work from the points of view of both speed and precision of crack depth. This was the result of the simpler specimen insertion and loading system which allowed testpieces to be removed, examined, and returned to the machine very rapidly and without the need to reset the load. As a result, in general, crack-front position and linearity were found to be highly satisfactory in specimens produced during FY 1977/78.

The overall scheme of testpiece extraction and notch detail are shown in Fig. I-1.

#### Instrumented impact testing

The fatigue-cracked testpieces were tested on an instrumented Charpy machine by the Dynatup system over a range of temperatures covering the ductile to brittle transition. Load-time and energy-time traces were photographed directly from the oscilloscope. The time scale chosen was generally such as to give the maximum detail in the early stages of deformation and fracture, as later events, given the specimen geometry and orientation, are less characteristic. The choice of system response characteristics in instrumented impact testing clearly represents a

compromise between achieving an acceptably "clean" trace and maintaining a sufficiently rapid rise-time to prevent unacceptable signal attenuation. Given the period of natural oscillation of a steel Charpy bar, estimated at  $33 \mu\text{s}$ , and a system rise-time of  $\sqrt{120} \mu\text{s}$  for 10% attenuation, all loads corresponding to times in excess of  $\sqrt{135} \mu\text{s}$  should be measurable with acceptable accuracy according to the criteria of Ireland (1) which are generally regarded as conservative. A value of  $135 \mu\text{s}$  is similar in magnitude to the time to yield for the impact velocity and material under consideration. In any event, the minor error in load associated with more brittle (short time) fractures will have little influence on transition temperature which

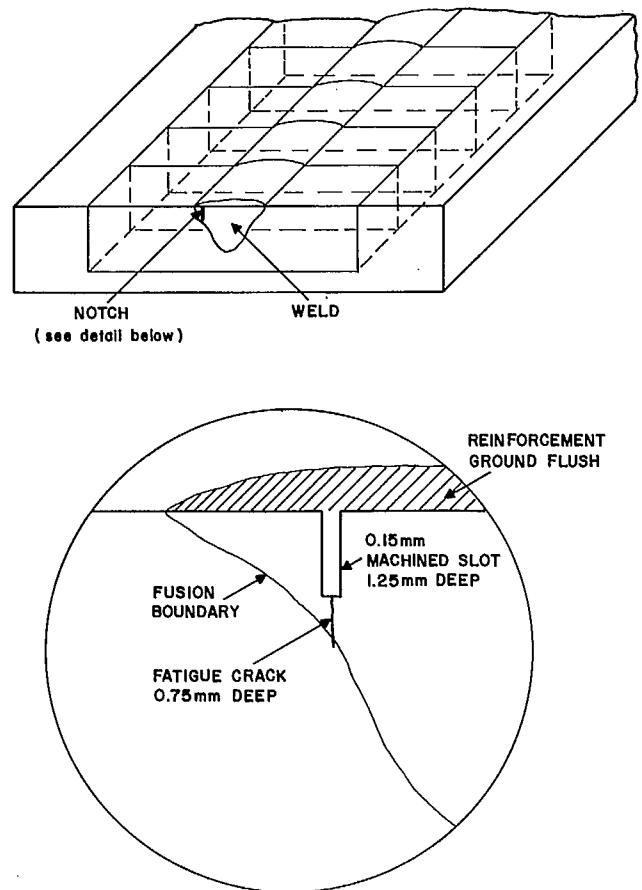


Fig. I-1 - Details of testpiece preparation - schematic

was used as a comparative measure of material toughness in the present work.

Characteristic values of load and time were measured from each oscilloscope trace. For the higher heat-inputs, the load-time curves could easily be divided into those in which fracture preceded yield, those in which brittle fracture occurred after yield, and those in which fully ductile fracture with no load instability occurred at all (Fig. I-2). At the lowest heat-inputs, the distinction was not so clear, as the small dimensions of the HAZ meant that brittle fracture could initiate in the interior of the testpiece, propagate a very short distance, and be arrested in the fine-grained HAZ or base metal with no instability, the load being transferred to the shear lips at the testpiece surface. To clarify this, the following criterion was adopted: if a deviation from linearity occurred in the load-time trace significantly below the extrapolated yield load, the fracture surface showed signs of brittle initiation at some point in the notch root, it was assumed the deviation was due to an increase in compliance resulting from crack extension, and not to yielding. The very regular variation of yield load with temperature gave considerable confidence in this procedure, and it was possible in this way to account rationally for the load-time behaviour of virtually all testpieces. A further complication in the load-time records of some of the low heat input samples tested, was a tendency to rapid shear failure along a contour following the fusion boundary. This generally led to instability and to low values of the maximum load. The low resistance to ductile fracture of hard heat-affected zones has been pointed out previously (2), and is not unexpected in the present case given the relative orientation of the fusion boundary and the anticipated trajectories of maximum shear. In any event, this is a post-yield phenomenon, and will have little effect on the ductile-brittle transition as defined for the purposes of the present work.

Considerable numbers of fractured testpieces were nickel-plated and sectioned in the

earlier stages of this work, with a view to determining the consistency of notch position. However, this approach was not continued as it is extremely time-consuming and was at variance with the economy oriented philosophy of the program. In effect, the toughness of the transformed HAZ is expected to deteriorate monotonically as the

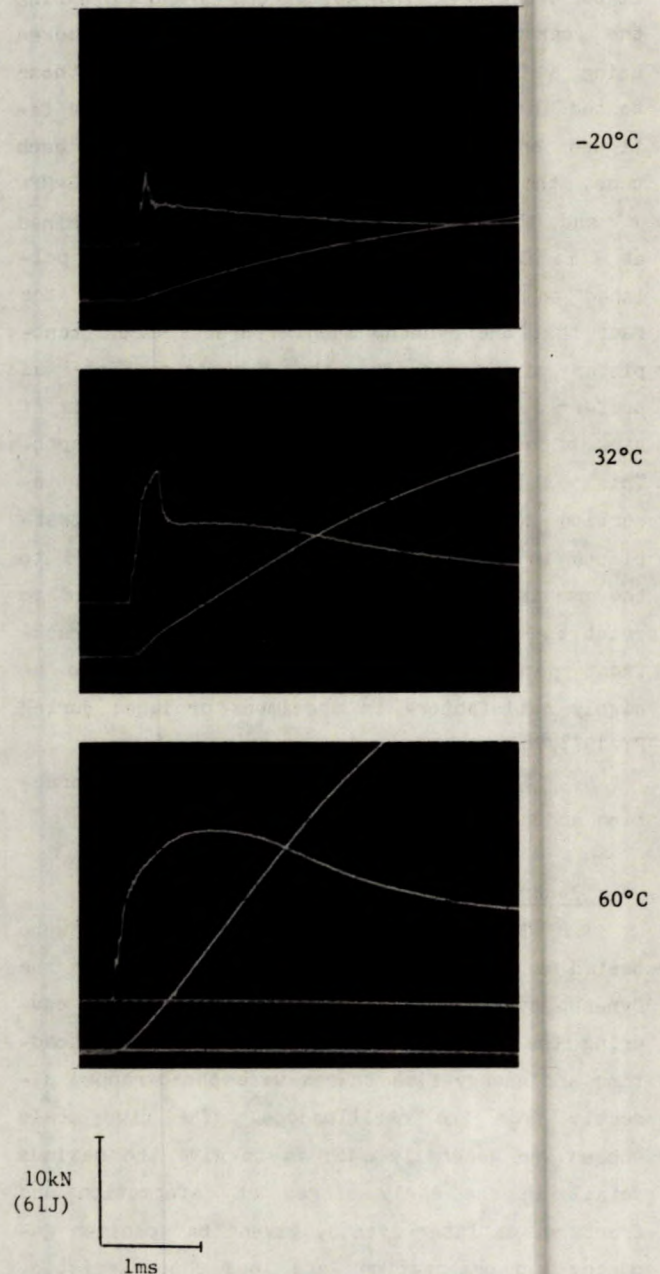


Fig. I-2 - Typical oscillograms: steel A, 2.4 kJ/mm



fusion boundary is approached. The assumption made in this study that a line of minimum toughness follows a path through the coarse grains of the HAZ adjacent to the fusion boundary appears to be justified. In most cases, sufficient duplicate testpieces were available to ensure that this "worst case" line could be located with confidence.

Yield and fracture loads were plotted against temperature e.g., Fig. I-3, and the anticipated transition from pre-yield fracture to stable, ductile tearing was observed with increasing temperature. To compare different materials, it was necessary to define a transition temperature. The temperature at which the fracture load intersects the extrapolated yield load-line provides a convenient and appropriate value. At low values of fracture load, the plastic zone size will be limited, and fracture behaviour is thus less likely to be influenced by regions outside the coarse-grained HAZ. In addition, the slope of the fracture load-temperature line is usually steep in the transition region between preand post-yield failure, and a transition temperature defined as above is thus not subject to

great error. Some consideration was also given to the adoption of a transition temperature based on time to fracture which is analogous to a deformation-based criterion e.g. COD. However, various factors such as local load-point indentation and deceleration can complicate the interpretation of such measurements. For similar reasons the adoption of a criterion based on energy was also considered likely to introduce unnecessary difficulties.

### Results and discussion

In the interests of brevity, the 56 load-temperature transition curves determined in the present program are not included in the body of this report, but are collected in the appendix, Part V. Yield load fracture transition temperatures were determined from these curves as discussed above. Values for the as-welded samples are shown in Table I-3, whereas those corresponding to the stress-relieved condition appear in Table I-4.

#### As-welded condition

Figures I-4 and I-5 summarize the transition temperatures determined in the as-welded condition for the 40 combinations of chemical composition and heat input. Results are plotted as a function of cooling time between 800 and 500°C, which is widely used as a characteristic

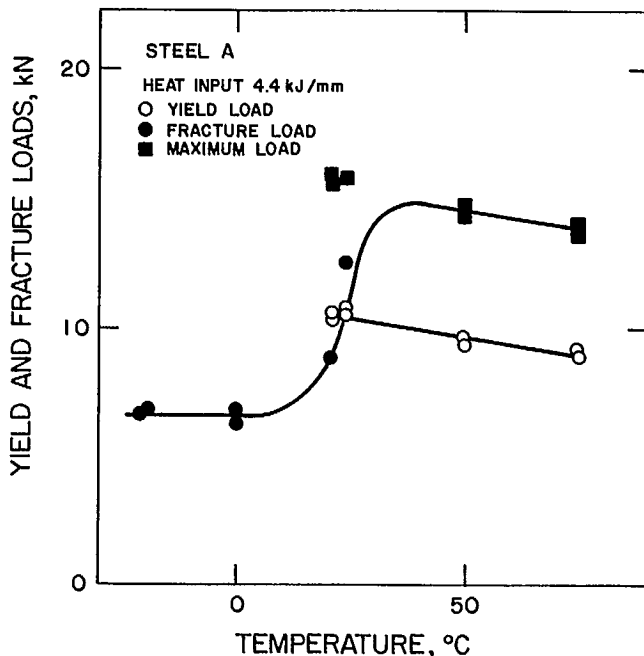


Fig. I-3 - Typical fracture transition curve

Table I-3 - Yield-load transition temperature, as-welded condition, °C

Steel	Heat input, kJ/mm (plate thickness, mm)				
	7.5(12)	4.4(12)	2.4(12)	1.4(12)	1.2(25)
A	+27	+23	+25	+ 9	- 6
B	+45	+32	+20	- 2	- 8
C	+53	+53	+18	-34	- 6
D	+42	+75	+17	-11	+ 2
E	+20	+35	+15	+ 5	-18
F	+30	+38	+29	- 7	-35
G	+47	+28	+22	- 3	- 4
H	+68	+75	+19	- 6	-17

parameter of weld thermal cycles. In Fig. I-5, which concerns the vanadium and molybdenum containing steels, results for corresponding vanadium and molybdenum free steels are also shown, for purposes of comparison.

From these figures the following observations may be made.

1. There is a general trend of decreasing toughness with decreasing cooling rate. However, while the plain carbon-manganese steel A shows no further deterioration, once a cooling

ing time of 39 s is reached, the transition temperatures of the micro-alloyed steels continue to rise, at least up to cooling times of 80 s. This parallels the behaviour observed in earlier work on simulated heat-affected zones in microalloyed steels (2,3). The two higher niobium steels C and D showed a slight deterioration in toughness on passing from the second fastest to the fastest cooling rate.

2. At a cooling time of 39 s, toughness is relatively insensitive to chemical composition, all transition temperatures lying between +15

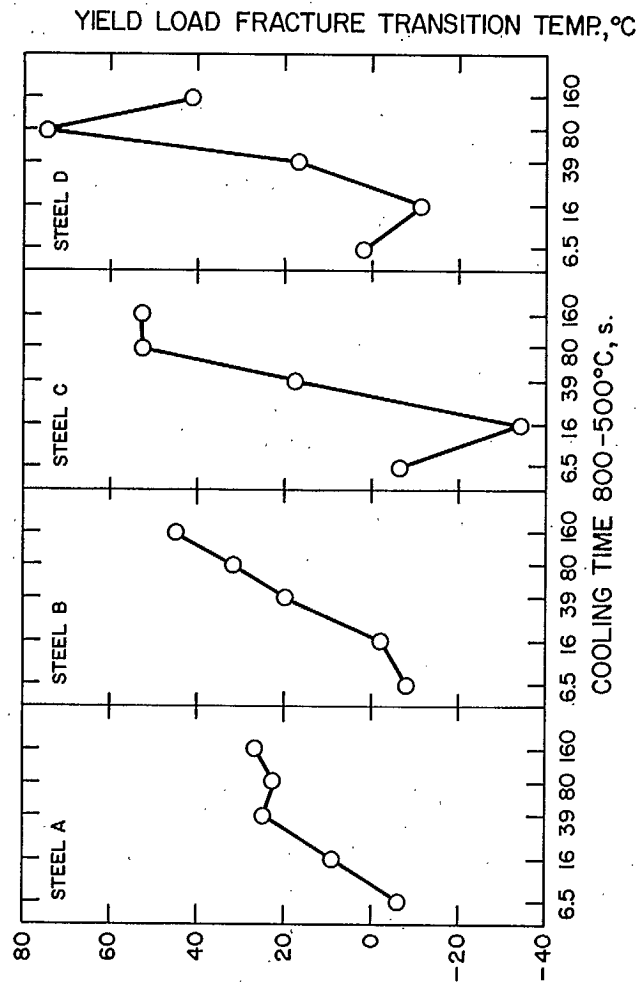


Fig. I-4 - Variation of yield load fracture transition temperature with cooling time (800-500°C), steels A-D

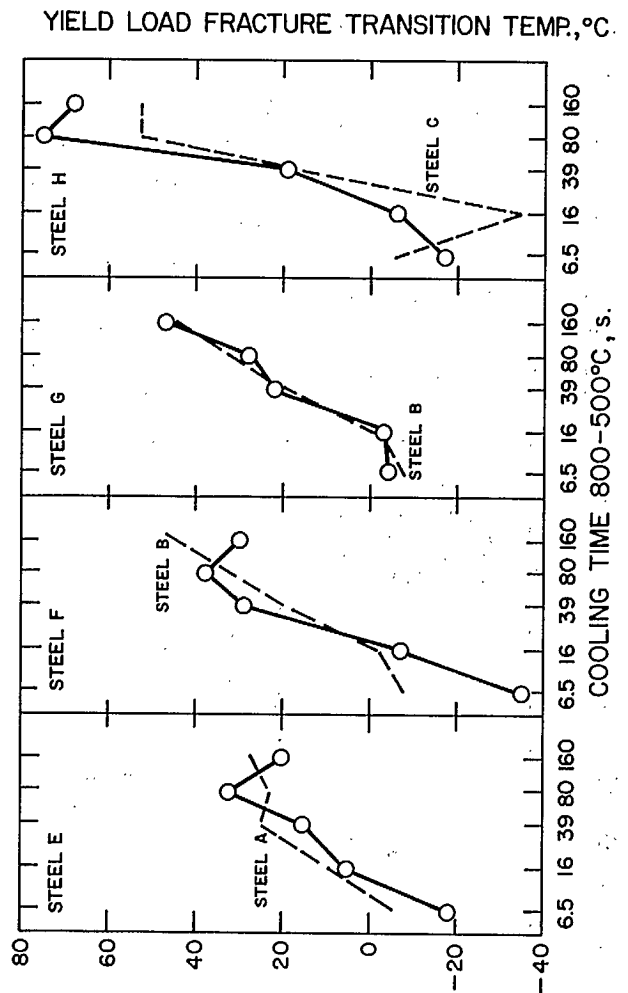


Fig. I-5 - Variation of yield load fracture transition temperature with cooling time (800-500°C), steels E-H

and +30°C.

3. At the shortest cooling times, the microalloyed steels are generally as tough as or tougher than the plain-carbon steel.
4. Vanadium appears to have very little effect on HAZ toughness, with or without niobium; the only exception appears to be the extremely low transition temperature achieved in steel F at the fastest cooling rate (Fig. I-5).
5. Molybdenum had no significant effect at the lower niobium content of steel G in Fig. I-5 whereas at the higher niobium content of steel H, the deterioration in toughness at high heat inputs is accentuated.

Figure I-6 summarizes the effect of niobium content. At the two highest heat inputs, some deterioration in toughness with increasing niobium level is apparent. The result for steel D (0.14% Nb) welded with the highest heat input may appear anomalous, and indeed, the transition curve was based on a relatively limited number of testpieces. However, variations in toughness reflect a complex system of metallurgical effects and interactions, and detailed consideration of such results will be taken up in Part IV in the light of findings on transformation behaviour and metallography.

At heat inputs of 2.4 kJ/mm and lower, niobium has no significant detrimental effect on toughness and may in some instances be beneficial.

#### Stress-relieved condition

Figure I-7 summarizes the results for welds stress-relieved at a nominal soaking temperature of 620°C. In strong contrast to the results obtained in the as-welded condition at the same heat-input, there is a marked deterioration in toughness with increasing niobium content. Vanadium appears to have no effect in the absence of niobium, but both vanadium and molybdenum appear to accentuate the detrimental effect of niobium. Table I-4 shows that the toughness of the stress-relieved micro-alloyed steels was somewhat improved at a lower temperature, whereas a higher

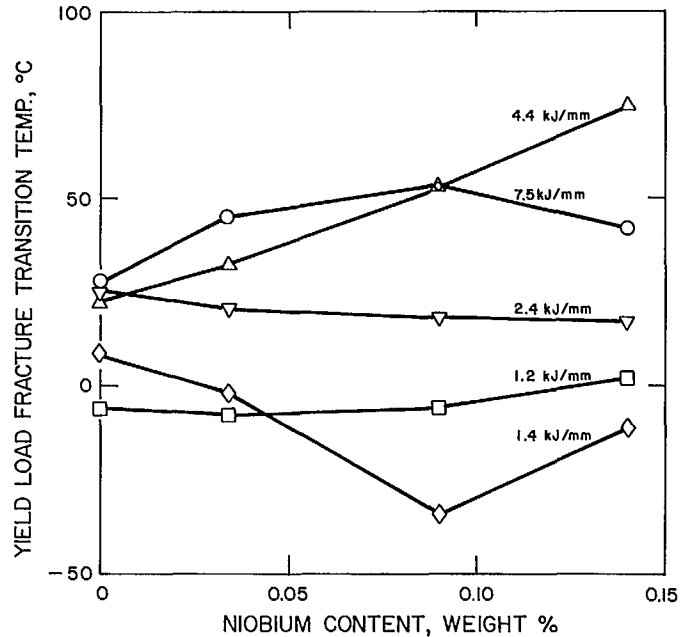


Fig. I-6 - Effect of niobium on yield load fracture transition temperature, as-welded condition

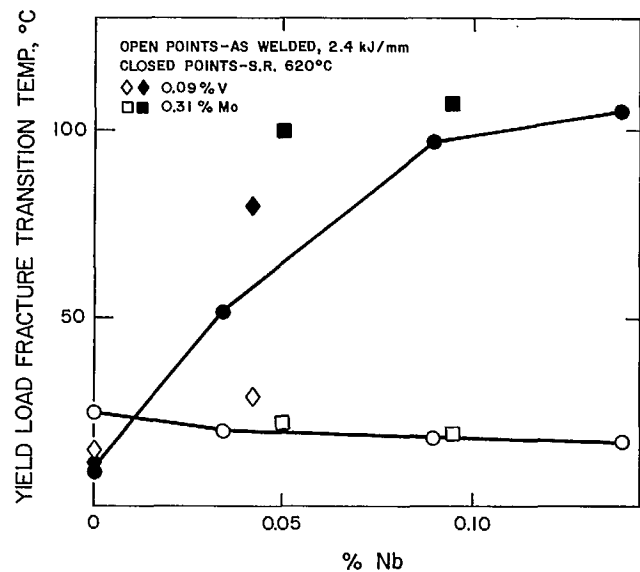


Fig. I-7 - Effect of niobium and stress-relief on yield load fracture transition temperature

Table I-4 - Yield-load transition  
temperature, stress-  
relieved condition, °C

Steel	Nominal stress-relief temperature, °C		
	620	510	675
A	+ 10	+30	+ 30
B	+ 52	-	-
C	+ 97	+60	+100
D	+105	-	-
E	+ 12	-	-
F	+ 80	+40	+ 75
G	+100	+80	+100
H	+107	-	-

temperature gave no improvement.

#### Conclusions

It has been established that the instrumented Charpy technique represents a powerful and economic approach to the study of the effects of chemical composition and heat input on HAZ toughness. Although the method is only comparative it is not certain that other small-scale laboratory techniques yield results which are more directly applicable to practice. Because of the rapid variation of microstructure with distance from the fusion line, some degree of scatter is inevitable, but the experimental technique has been refined so that this effect is minimized. The economical nature of the technique allows many samples to be tested so that the probability limit is good that a true lower limit to toughness can be identified.

Niobium has been found to be detrimental only at the highest heat inputs in the as-welded condition. Vanadium has very little effect on notch toughness but molybdenum appears to accen-

tuate the detrimental effect of niobium at high niobium contents.

In the stress-relieved condition, niobium causes a progressive and serious deterioration in toughness at a heat input of 2.4 kJ/mm. Vanadium and molybdenum appeared to accentuate this effect to some extent. A reduction in stress-relief temperature from 620 to 510°C led to some improvement in toughness in micro-alloyed steels although an increase to 675°C had no apparent effect.

In subsequent sections, the transformation behaviour, Part II, and the metallographic features, Part III, of the experimental steels will be considered. An attempt to relate the toughness results discussed above to the metallurgical features of the 8 steels will be made in Part IV.

#### Acknowledgements:

All welding, heat-treatment, machining and mechanical notching was carried out at Dominion Bridge Co. Ltd., Lachine, Quebec under the general supervision of B.A. Graville and L. Malik. W. Fearis was responsible for details of specimen preparation. Fatigue pre-cracking and instrumented Charpy testing were performed by R. Dufresne and J.-P. Fachinetti. Without the willing cooperation of the above, it would not have been possible to complete this portion of the program in the limited time available.

#### References:

1. Ireland, D.R. "Dynamic fracture toughness"; The Welding Institute, Cambridge, U.K., p. 47; 1977.
2. Rothwell, A.B. and Bonomo, F. "Welding of pipeline steels", Welding Research Council; p. 118; New York; 1977.
3. Bonomo, F. and Rothwell, A.B.; Zvaranie; 20: 9-11: 300; 1971.

## PART II: CONTINUOUS-COOLING TRANSFORMATION CHARACTERISTICS

by

A.B. Rothwell\*

### Introduction

One of the principal aims in the final year of the program was to develop a thorough understanding of the fundamental metallurgy underlying the variation in toughness described in Part I. A number of microstructural factors are known to influence toughness. Among the most important of these are the dimensions of the characteristic structural features, e.g., the morphology of prior austenite grains, "co-variant packets" for structures consisting of parallel laths, cementite particles etc., the presence of a strengthening precipitate dispersion and, above all, the basic microstructure e.g., ferrite-pearlite, bainite, martensite etc. It is often difficult in real welds to develop a full appreciation of the effects of process and composition on transformation behaviour, and thus on microstructure, as it is usually not possible to determine the transformation temperatures with any degree of precision. Independent transformation studies have thus been incorporated in weldability investigations for many years, and have provided information which is vital to an understanding of welding metallurgy (1-5). A number of techniques are available for such studies, but one of the most widely used has been that of high-speed dilatometry, and this was adopted in the present investigation.

### Experimental details

The experimental materials were those already detailed in Table I-1 of Part I.

Ideally, it is clearly desirable that the equipment be capable of simulating in their entirety the thermal cycles occurring in real weld

heat-affected-zones (4). However, no apparatus currently exists which can achieve this ideal for a full range of welding processes, though the "Gleeble", and other instruments with sophisticated programming capabilities, can reproduce the cooling regime of any cycle to a high degree of precision. The instrument used for the present investigation, the Fuji "Formaster-F", has some limitations in both heating and cooling capabilities. However, it does allow the full range of cooling rates in the transformation range to be reproduced, and being designed primarily as a dilatometer yields high quality dilatation-temperature traces.

Testpieces 10 mm long by 3 mm in diameter, with a 2-mm deep thermocouple cavity 2 mm in diameter in one end, were machined from the 12.7-mm plates. This configuration had given good control and temperature distribution, particularly for rapid thermal cycles (6). Platinum/platinum-13% rhodium thermocouples were welded by capacitor discharge from 0.2-mm diameter wire; the extremely small hot-junction thus formed was discharge welded to the bottom of the cavity in the testpiece. The testpiece was then mounted in the dilatometer head inside a vacuum chamber. Heating was by a 3-kW, 1.7-MHz induction coil surrounding the testpiece; provision was also made for gas cooling. Dilatation was detected through a quartz rod by an LVDT system operating within a thermostatically controlled oven, to eliminate thermal fluctuations. The displacement signal and thermocouple output were recorded simultaneously on a two pen recorder, and also cross plotted on a Honeywell X-Y recorder. The furnace chamber was evacuated to a pressure of <13 mPa before each run, and high-purity helium was used where necessary for cooling.

---

\*Noranda Research Centre, Pointe Claire, Quebec.

Duplicate, or triplicate testpieces were treated for each steel and cooling rate.

Five thermal cycles, designated I-V were investigated, giving cooling times between 800 and 500°C of nominally 3, 10, 30, 100 and 300 s respectively, and thus covering the full range associated with normal welding processes. In all cases the peak temperature of 1320°C was reached in 10 s. This was the maximum rate of heat input achievable consistent with avoiding melting the specimen, although it is somewhat slower than would be observed close to the fusion boundary in a typical arc weld.

The five thermal cycles adopted are shown in Fig. II-1. Cooling curves I and II, for gas cooling only, are the most closely representative of the conditions typically experienced by the HAZ of a real weld, but are complicated by the effect of the heat generated within the test-piece on transformation. As in many cases the resulting thermal arrest occurred between 800 and 500°C, some variation from nominal cooling rates within this range was inevitable. Cooling curves III-V were linear from the peak temperature. Some gas flow was necessary for cycles III and IV to maintain linearity through the transformation range and below. Clearly, the cooling rates at high temperature for these three cycles will be slower than for a real weld at corresponding cooling times in the 800-500°C range. Despite these limitations, however, it is considered that the transformation data generated in the current study are valuable and will cover the same range of transformation temperatures and products as would be observed in real welds, though some slight displacement along the cooling time axis is likely.

The dilatation thermocouple output traces during cooling were replotted as a dilatation vs. temperature curve to eliminate errors arising from the non-linearity of the thermocouple signal. Transformation start and finish temperatures could be determined as the first detectable deviation of this curve from the linear, austenite and ferrite + carbide dilatation traces respectively. Temperatures for a given degree of

transformation were determined as the intersection between the experimental curve and lines dividing the distance between the austenite and ferrite + carbide lines and their extrapolations into the desired proportions (7). Figure II-2 shows a typical curve, together with the construction for determining percentage transformation. In practice, a 2% deviation from linearity is the minimum which can be determined with any degree of accuracy, and this level was accordingly used to define the transformation start and finish temperatures shown in the CCT diagrams. In the interests of clarity, the 2% and 98% lines are not shown in Fig. II-2.

CCT diagrams were constructed for all eight steels. For ease of comparison with existing welding data, the presentation adopted was to plot transformation temperature as a function of cooling time from 800 to 500°C. It should be noted, however, that diagrams plotted in these coordinates cannot be directly compared with those presented in the conventional manner.

In addition to the above measurements,  $Ac_1$  and  $Ac_3$  temperatures were determined at a heating rate of 0.033°C/s.

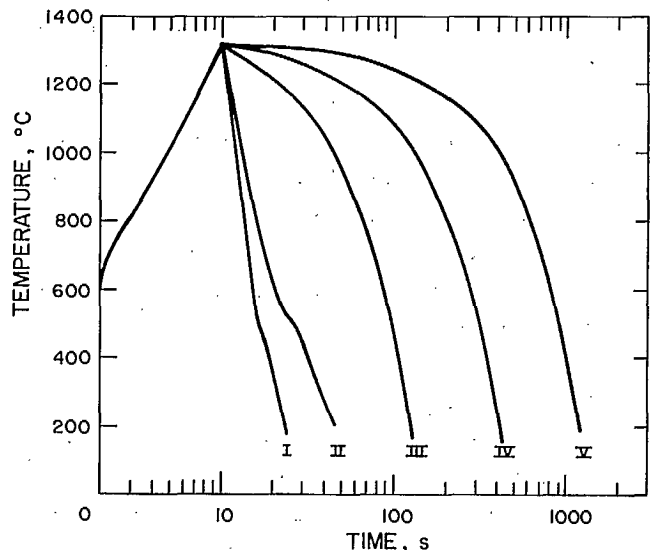


Fig. II-1 - Thermal cycles used in dilatometric investigation

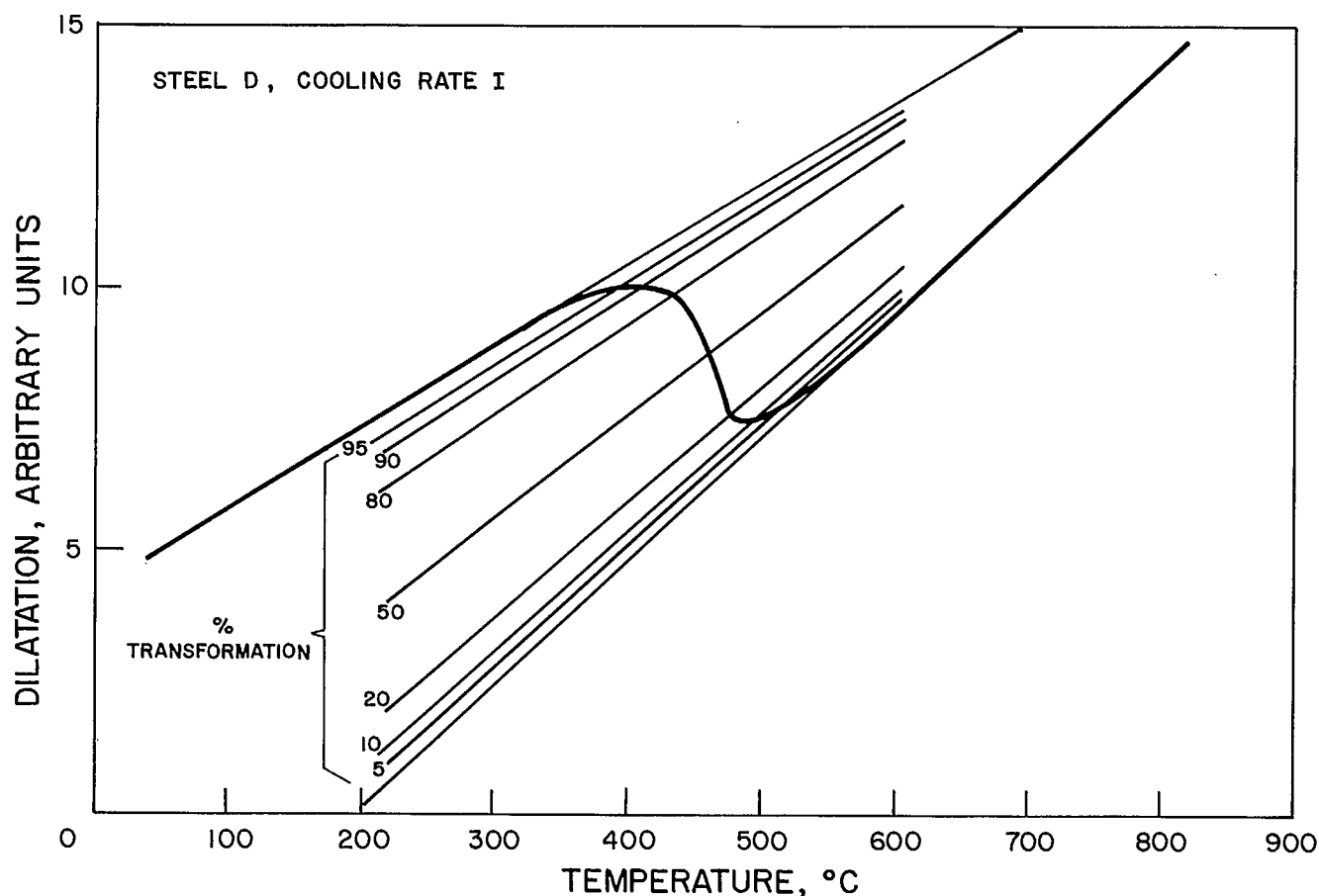


Fig. II-2 - Typical dilatometric curve and construction for obtaining percentage transformation

Each testpiece was sectioned transversely at midheight and examined metallographically. The general microstructure was observed after etching in 2% nital. It was also confirmed that the degree of vacuum and the purity of the cooling gas had been sufficient to prevent significant decarburization, which can give rise to spurious transformation start results.

The microstructure of the carbon-rich regions (carbides or martensite/retained austenite) was examined at high magnification after etching in saturated picral. Finally, the diamond pyramid hardness was determined on each section as the mean of at least three indentations with a 5-kg load.

#### Results and discussion

Table II-1 shows  $Ac_1$  and  $Ac_3$  temperatures for the eight experimental steels.  $Ac_1$  appeared to be relatively insensitive to microalloy additions, though there may have been a minimum at around 0.1% Nb.  $Ac_3$  was not significantly affected by niobium or molybdenum additions, but did appear to be somewhat higher in the vanadium containing steels E and F. However, the end of transformation on heating is not as well defined as the beginning. Steels E and F would contain substantial quantities of vanadium carbide in the as-rolled condition; these precipitates become readily soluble immediately above the ferrite-austenite transformation temperature



Table II-1 -  $Ac_1$  and  $Ac_3$  temperatures  
for experimental steels

Steel	Transformation temperature, °C	
	$Ac_1$	$Ac_3$
A	700	865
B	690	855
C	680	865
D	690	880
E	700	905
F	695	900
G	690	875
H	685	880

and the influence of their progressive dissolution could be sufficient to distort the austenite dilatation line in its initial stages and yield a spuriously high  $Ac_3$  temperature. Niobium carbide would not have this effect as its solubility is very limited in the low austenite range. Because these pseudo-equilibrium transformation data are of limited interest, given the high austenizing temperatures adopted in the CCT studies reported below, no attempt was made to resolve this question.

Continuous-cooling transformation diagrams for the eight steels are shown in Fig. II-3 to II-10: the corresponding micrographs appear in Fig. II-11 to II-26. The CCT diagrams will be discussed individually in the first instance; the effects of varying chemical composition will then be examined. In steel A in Fig. II-3, the temperatures corresponding to 2% transformation rise progressively from 560°C for the fastest cooling rate to over 700°C for cooling rates III and IV. The 2% transformation temperature falls to 680°C for cooling rate V; this may appear anomalous, but it should be noted that in this range, transformation is grain-boundary nucleated. The extremely large grain size of 0.5-1 mm generated by the long time at high temperature, thus causes a marked reduction in the initial transformation rate.

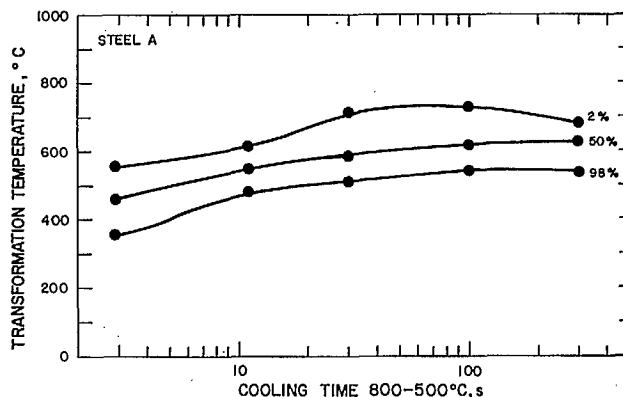


Fig. II-3 - Continuous-cooling transformation diagram, steel A

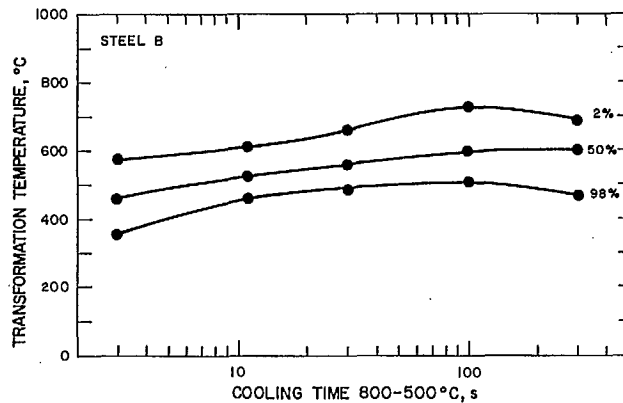


Fig. II-4 - Continuous-cooling transformation diagram, steel B

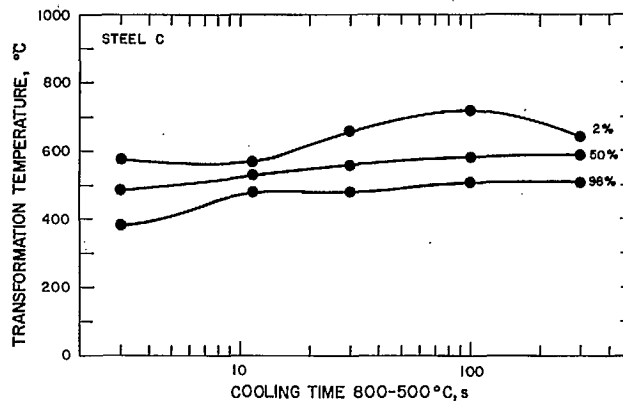


Fig. II-5 - Continuous-cooling transformation diagram, steel C

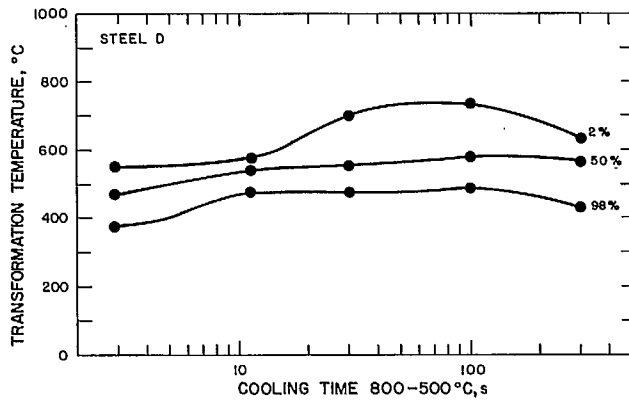


Fig. II-6 - Continuous-cooling transformation diagram, steel D

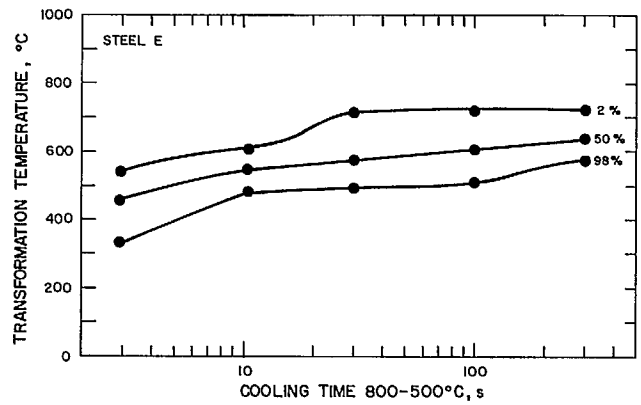


Fig. II-7 - Continuous-cooling transformation diagram, steel E

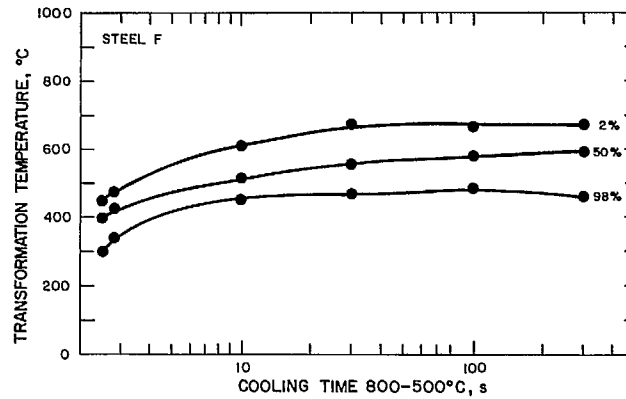


Fig. II-8 - Continuous-cooling transformation diagram, steel F

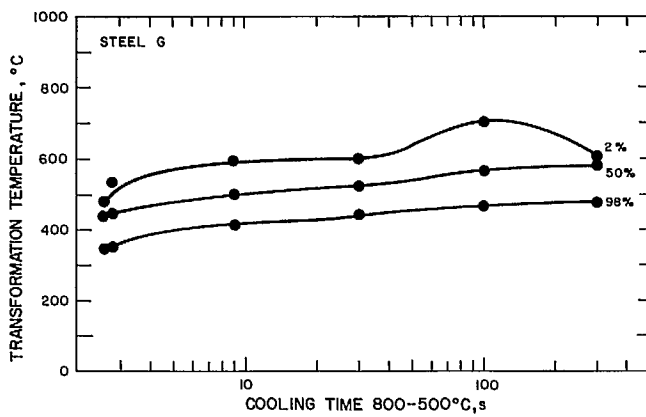


Fig. II-9 - Continuous-cooling transformation diagram, steel G

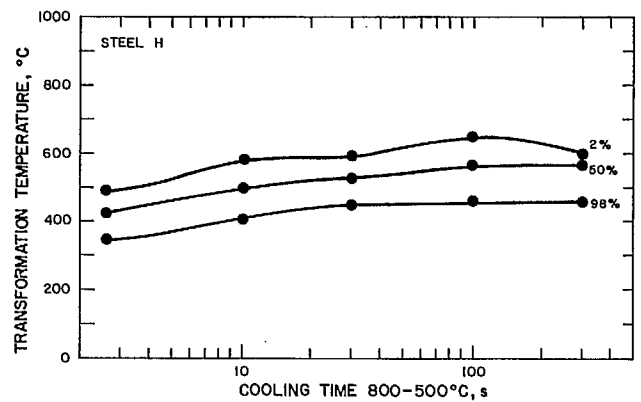


Fig. II-10 - Continuous-cooling transformation diagram, steel H

The 50% transformation temperature for this steel shows a progressive rise from 460°C at the fastest cooling rate to 625°C at the slowest, whereas the 98% transformation temperature rises rapidly from 355°C for cooling rate I to 475°C for rate II, and then more slowly to 540°C for the slowest cooling rates.

The sequence of microstructures shown in Figs. II-11 and 12 agrees well with these transformation temperatures; the  $M_s$  temperatures for the experimental steels should lie in the range 470-480°C (8), while grain boundary nucleated polygonal ferrite generally begins to form only at temperatures above 680°C. In the intermediate temperature range, structures broadly referred to as bainitic are formed.

At the fastest cooling rate, the microstructure of steel A is approximately half martensitic and half bainitic, in agreement with the 50% transformation temperature of 460°C. The martensite progressively disappears as the cooling rate decreases, and some grain-boundary polygonal ferrite appears at cooling rate III, as would be expected from the high transformation start temperature. The bainitic ferrite consists primarily of parallel laths at the three fastest cooling rates, but appears to be more randomly oriented for cooling rates IV and V. The carbon-rich regions in the bainitic structure are predominantly light-etching martensite/retained austenite (M-A) at the fastest cooling rates I and II; some dark-etching carbide aggregates appear at cooling rate III, whereas for slower cooling rates, only carbide aggregates are visible, (Fig. II-17).

Steel B shows similar transformation behaviour to that of steel A, although the rise in transformation start temperature to over 700°C occurs at a somewhat longer cooling time, (Fig. II-4). In addition, there may be a slight fall in transformation finish temperature at the longest cooling time. The optical microstructures are thus broadly similar to those of steel A (Fig. II-13 and 14), except that little or no grain boundary ferrite is visible at cooling

rate III, and some M-A persists even at the longest cooling time.

The transformation behaviour shown in Fig. II-5 and microstructures in Fig. II-15 and 16 as observed in steel C, are similar to those in steel B. However, the transformation start temperature at cooling rate II remains somewhat lower, and the fall in start temperature at the slowest cooling rate appears more pronounced.

Steel D in Fig. II-6, 17 and 18 behaves in a similar manner to the other niobium steels, although the fall in transformation temperature at the slowest cooling rate may be even more marked. In addition, the start temperature is somewhat higher for cooling rate III at 700°C, and no grain-boundary ferrite is observed.

Steel E shows rather lower transformation temperatures at the fastest cooling rate than do steels A-D (Fig. II-7), and there appears to be a higher percentage of martensite in the microstructure (Fig. II-19). Furthermore the bainitic ferrite is predominantly randomly orientated from cooling rate III onwards. Little M-A appears beyond cooling rate III (Fig. II-20). At the slowest cooling rate, the transformation is virtually complete by 570°C, and the resulting microstructure is a coarse, almost equiaxed ferrite.

Steel F in Fig. II-8, 21 and 22 shows particularly low transformation temperatures at the fastest cooling rate and the structure is predominantly martensitic. At slower cooling rates, transformation temperatures remain somewhat lower than in the corresponding steels B and E, but grain-boundary ferrite is visible at the two slowest cooling rates.

Steels G and H also show low transformation temperatures and predominantly martensitic microstructures at the fastest cooling rate (Fig. II-9, 10, 23-26). In addition, as expected, molybdenum holds the transformation start temperature to 600°C or below for longer cooling times than in other steels. No significant amount of grain-boundary ferrite was observed at



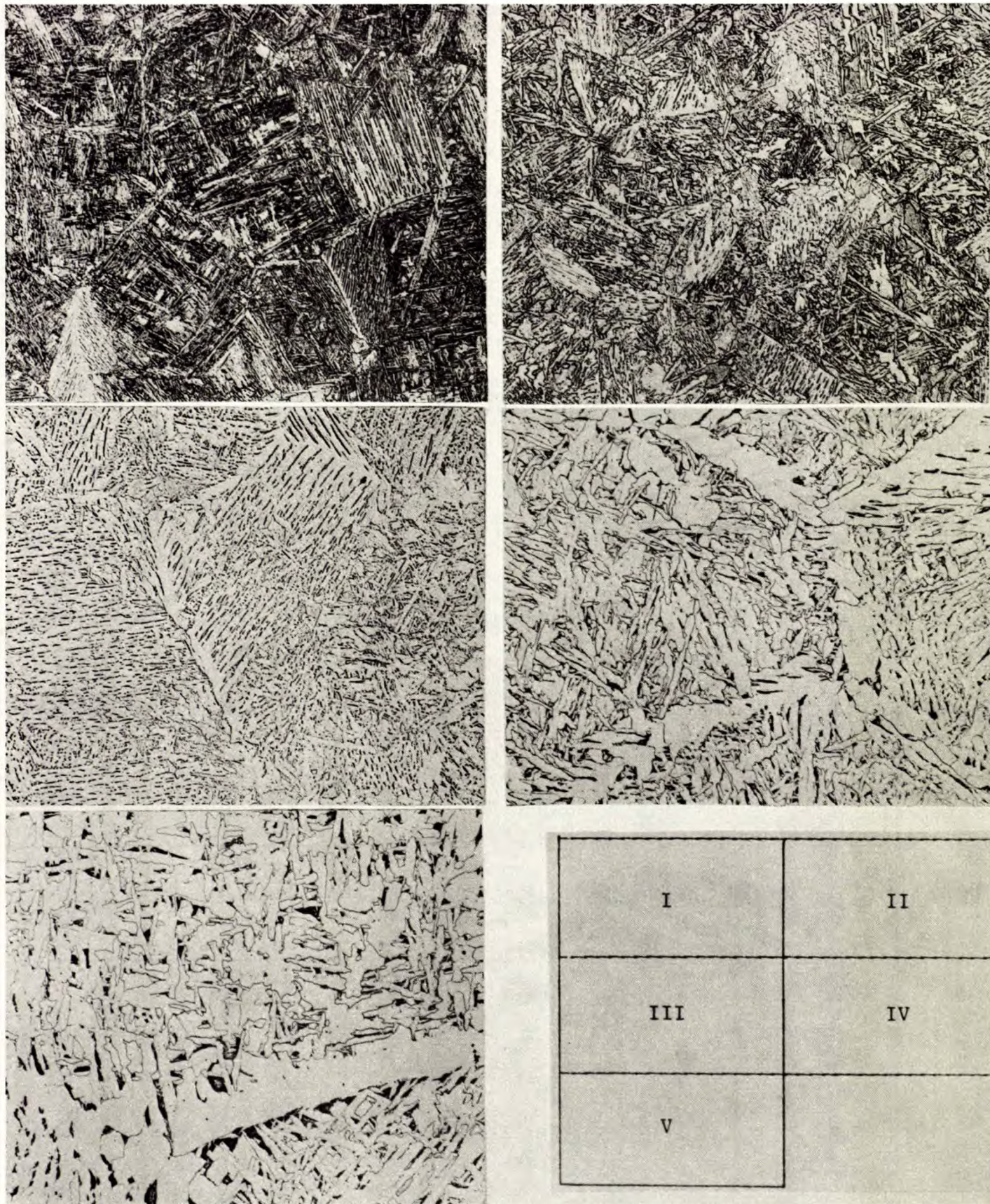


Fig. II-11 - Optical micrographs, steel A, cooling rates I-V nital etch, x200



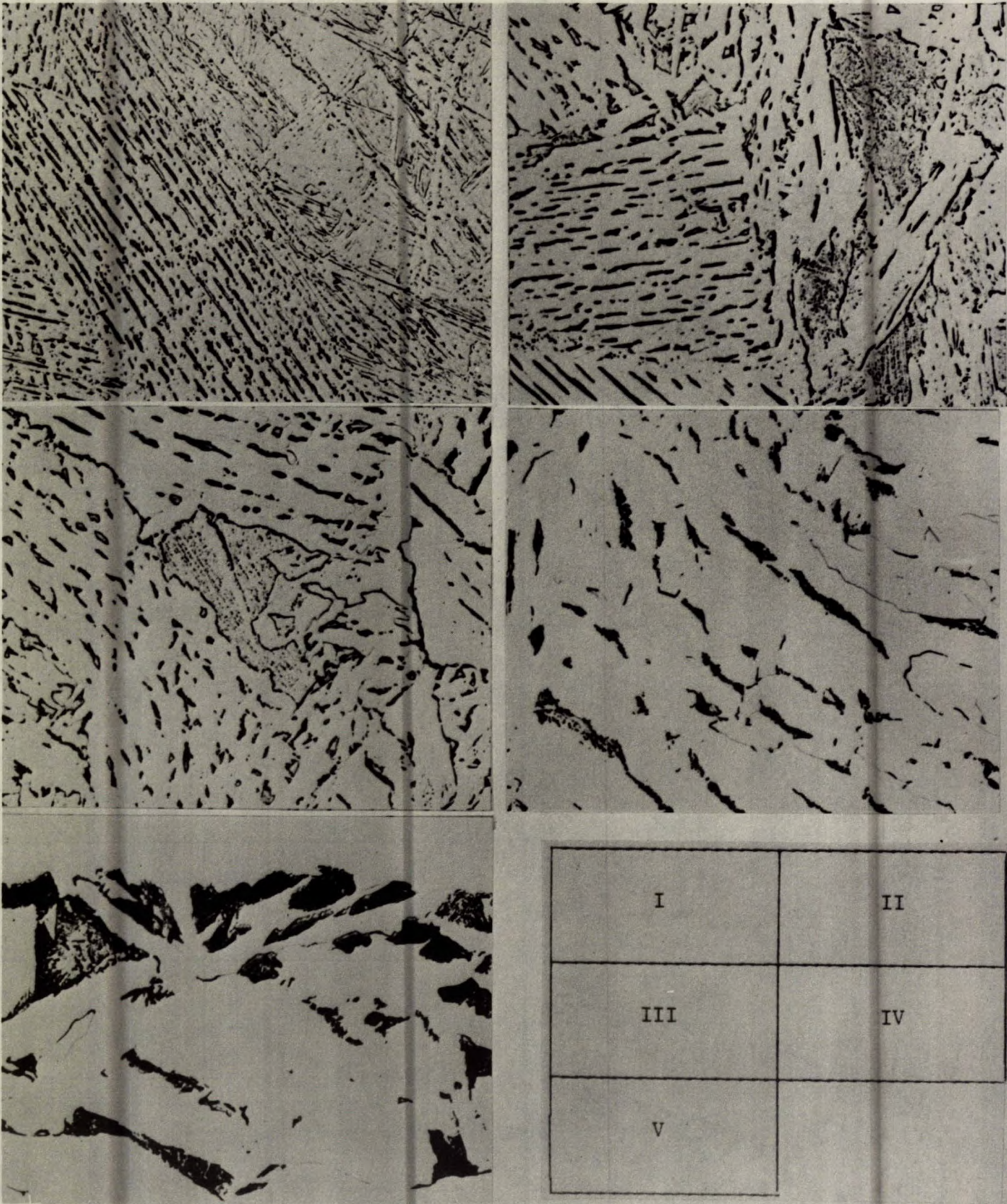


Fig. II-12 - Optical micrographs, steel A, cooling rates I-V picral  
etch, x1000



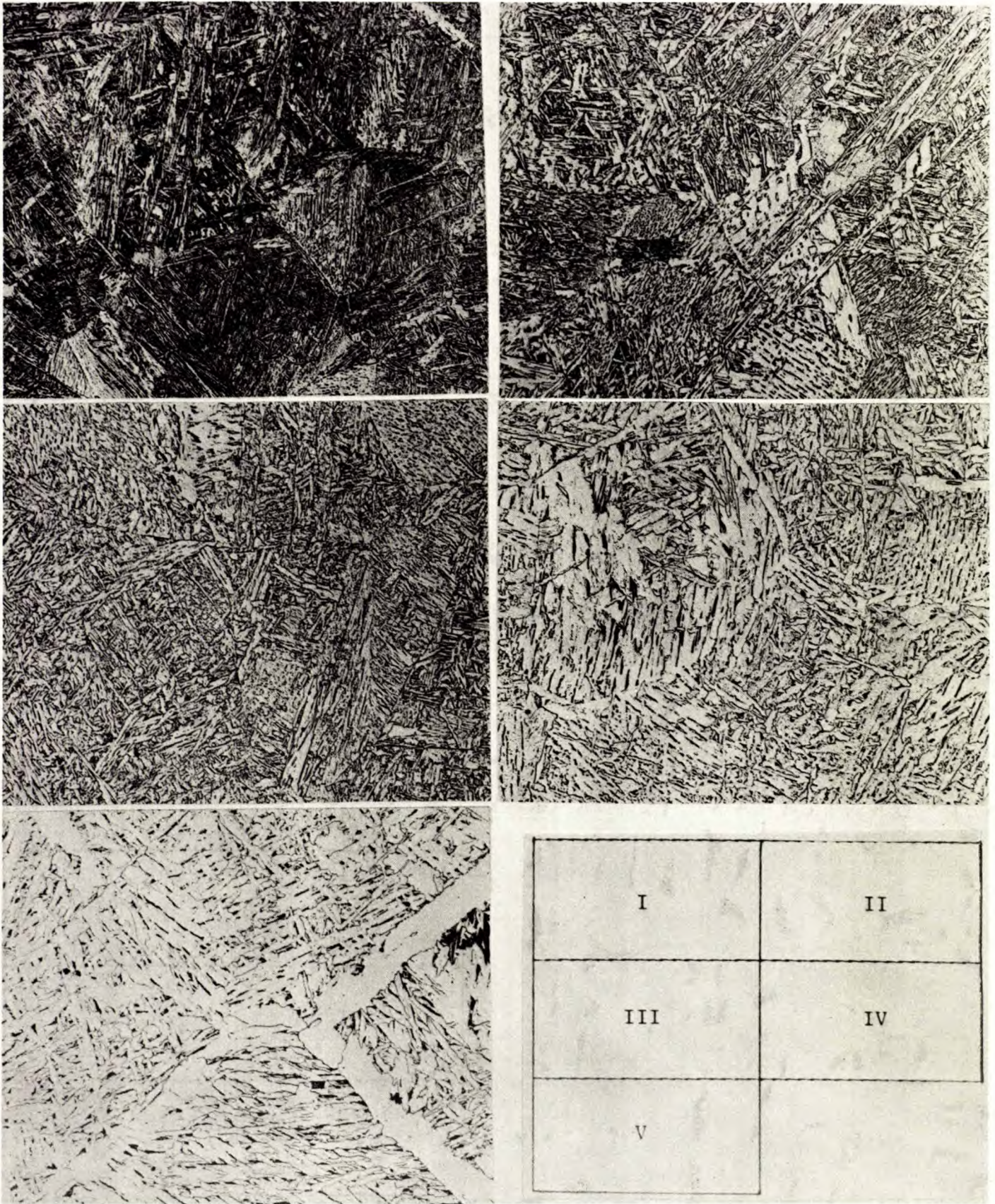


Fig. II-13 - Optical micrographs, steel B, cooling rates I-V nital etch, x200



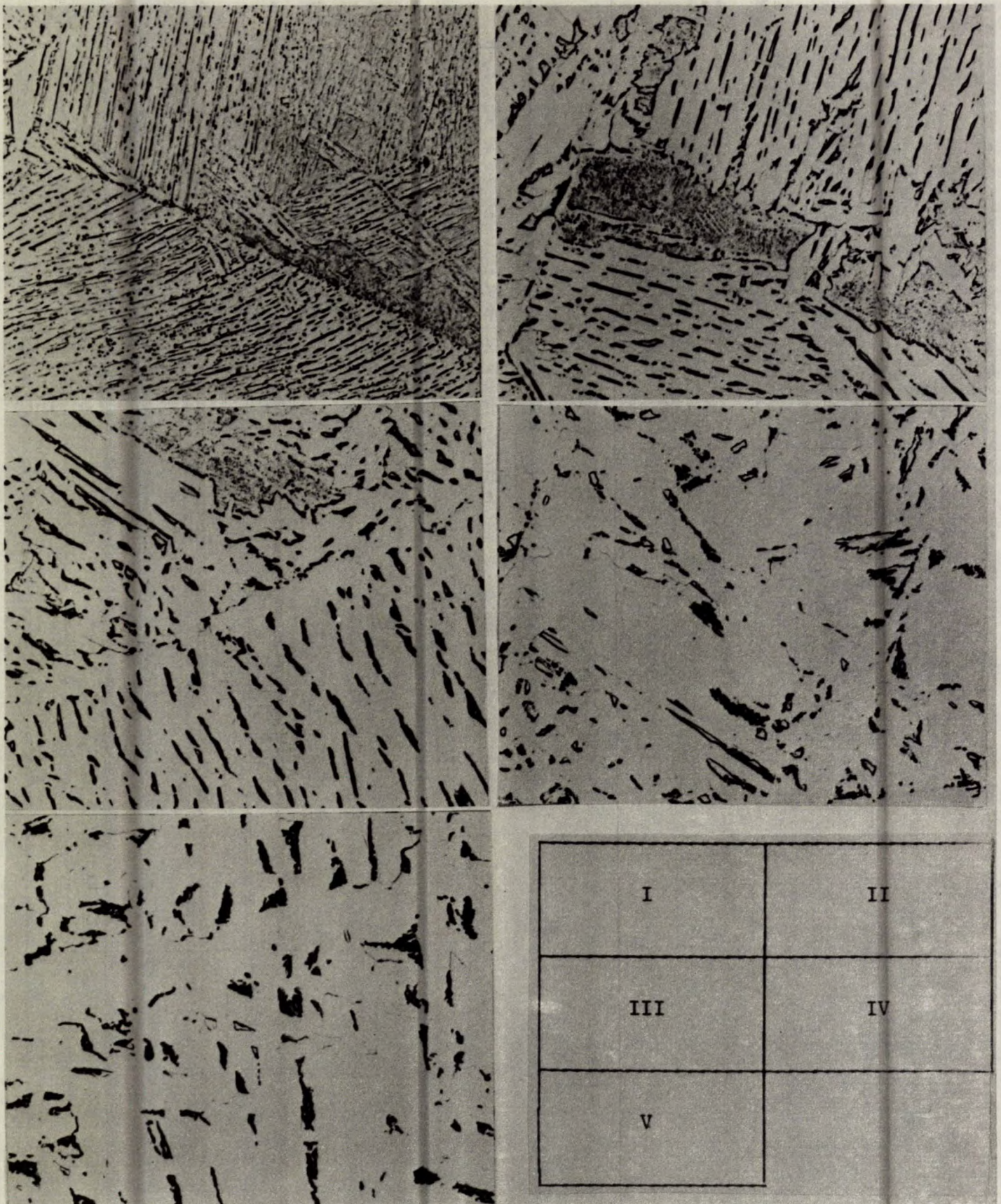


Fig. II-14 - Optical micrographs, steel B, cooling rates I-V picral  
etch, x1000



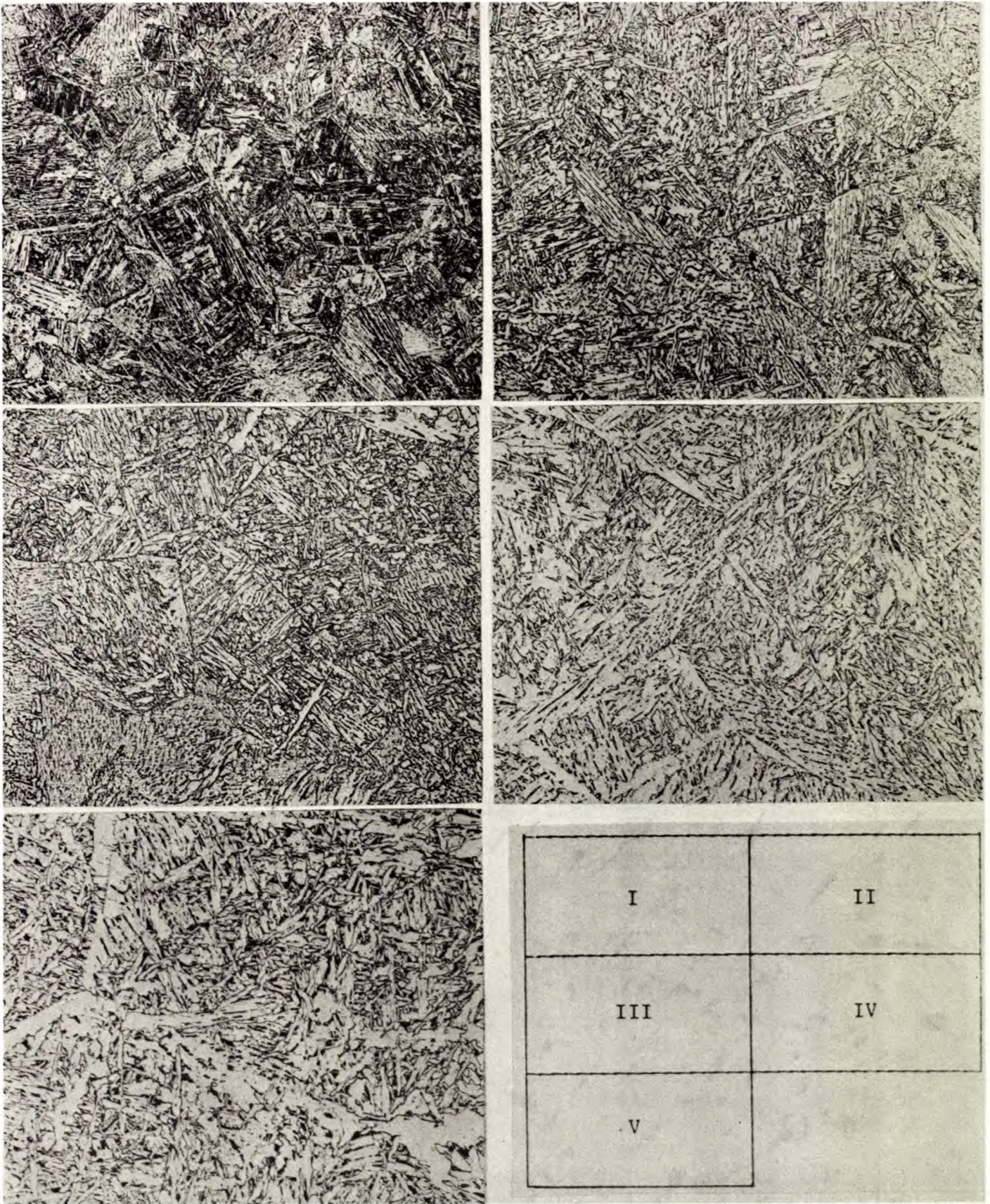


Fig. II-15 - Optical micrographs, steel C, cooling rates I-V nital etch, x200



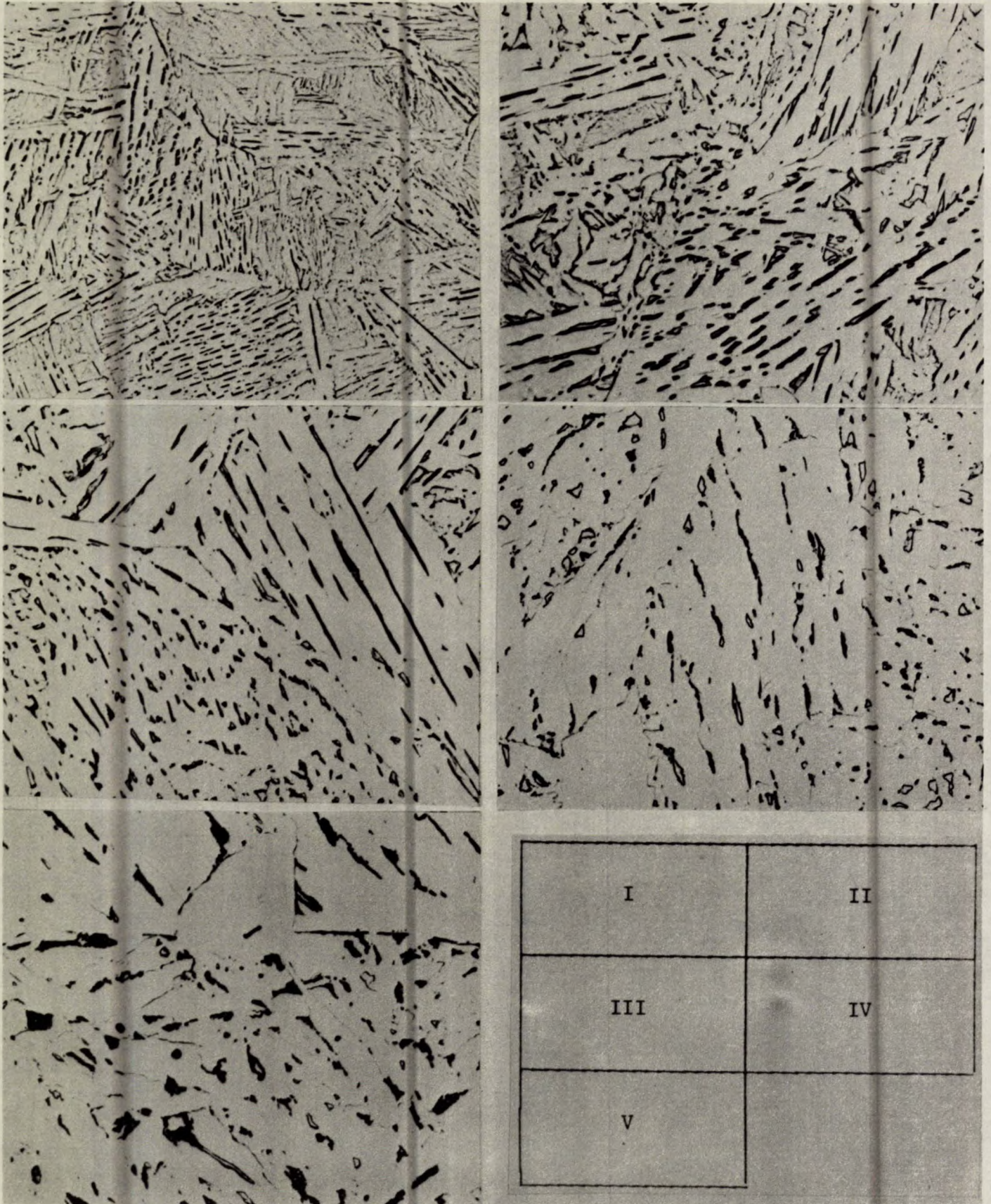


Fig. II-16 - Optical micrographs, steel C, cooling rates I-V picral  
etch, x1000



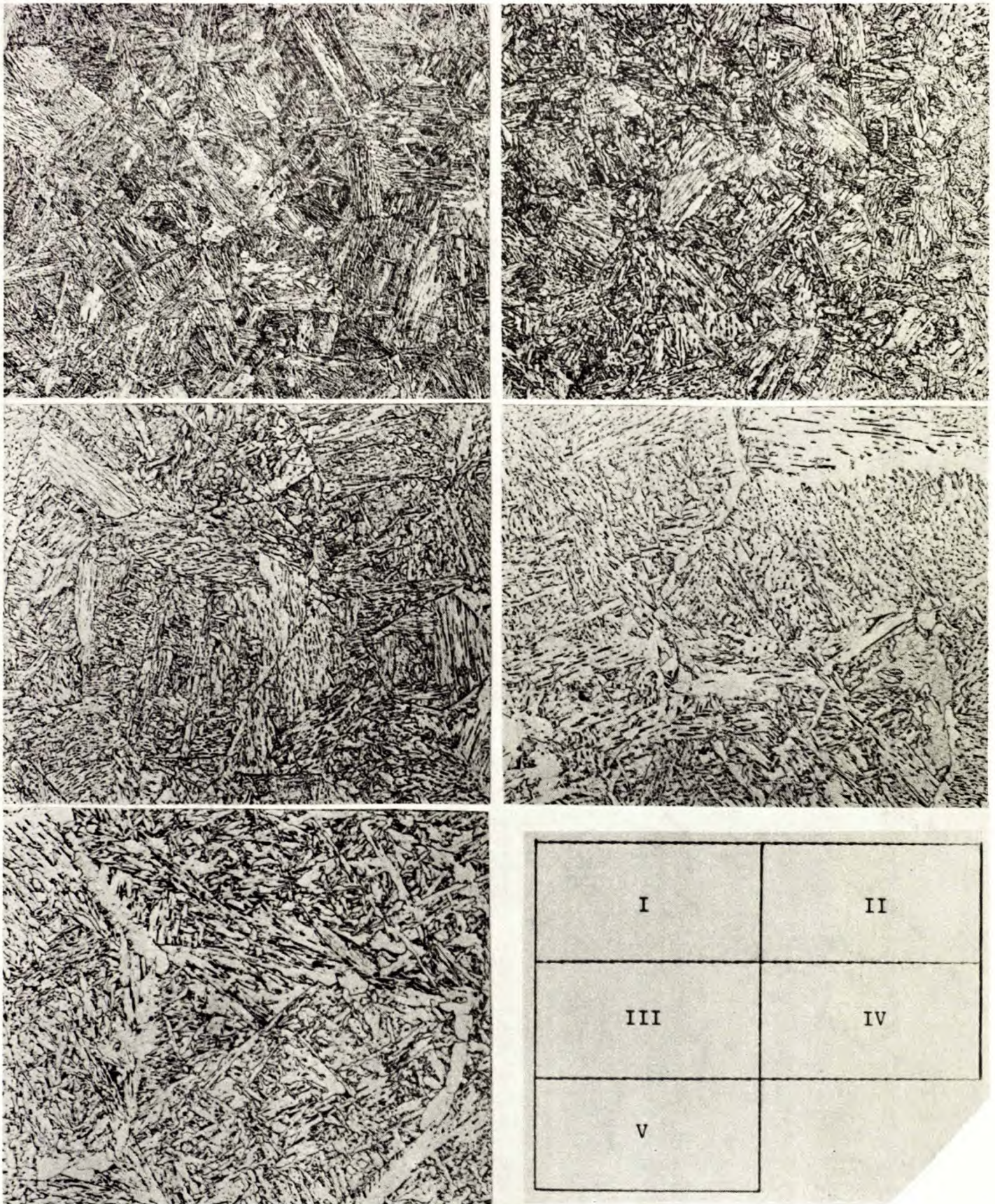


Fig. II-17 - Optical micrographs, steel D, cooling rates I-V nital etch, x200



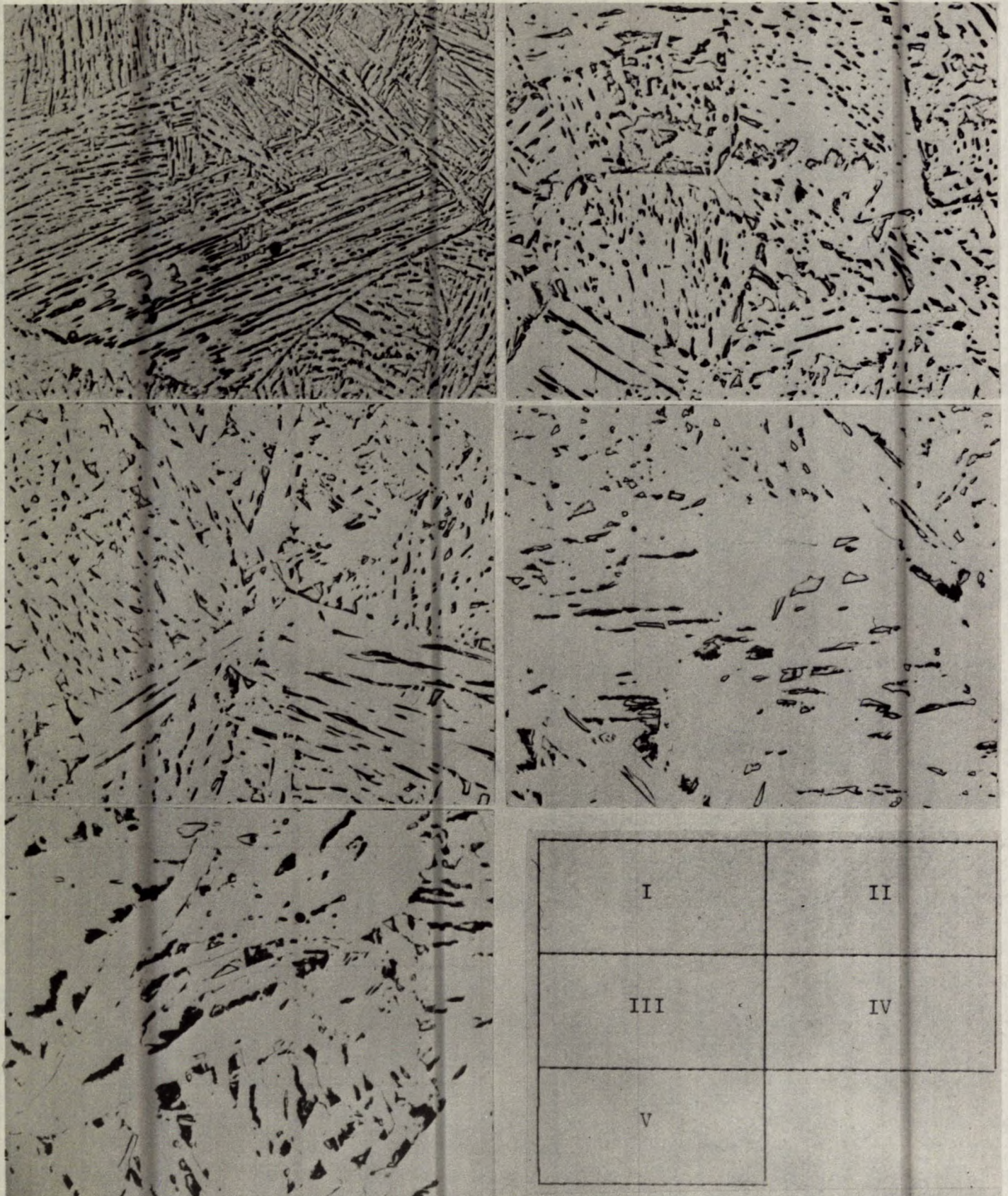


Fig. II-18 - Optical micrographs, steel D, cooling rates I-V picral  
etch, x1000



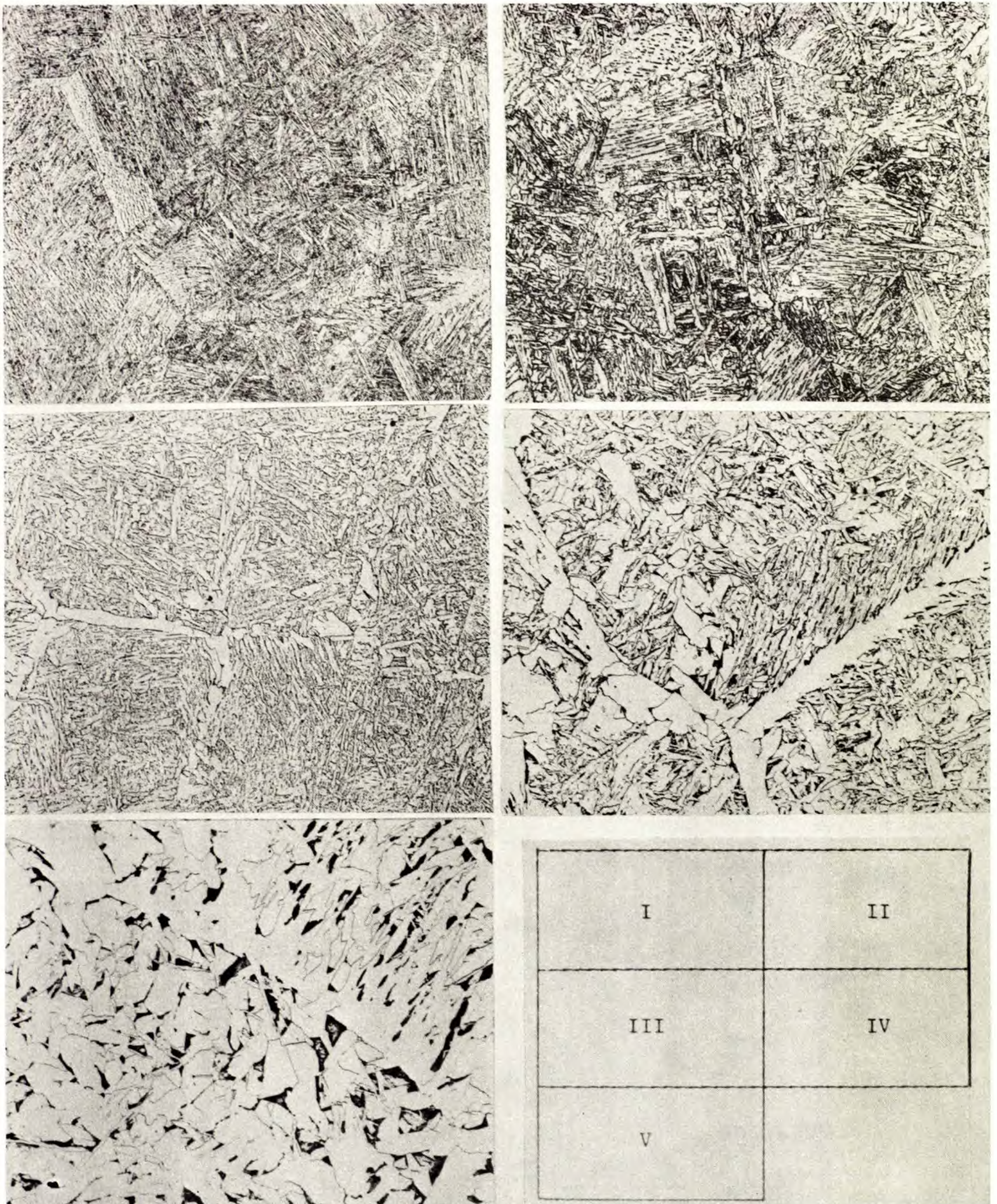


Fig. II-19 - Optical micrographs, steel E, cooling rates I-V nital etch, x200



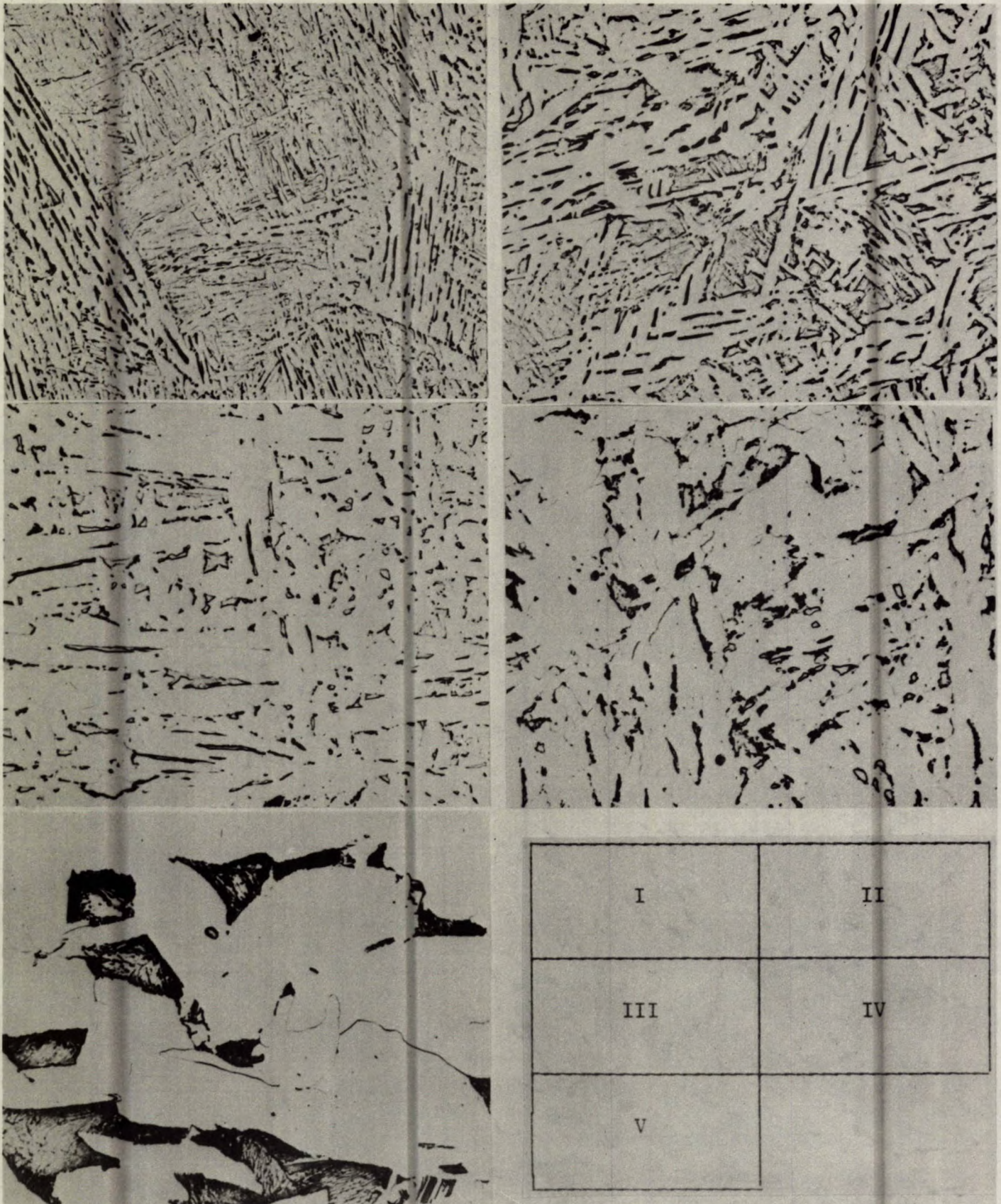


Fig. II-20 - Optical micrographs, steel E, cooling rates I-V picral etch, x1000



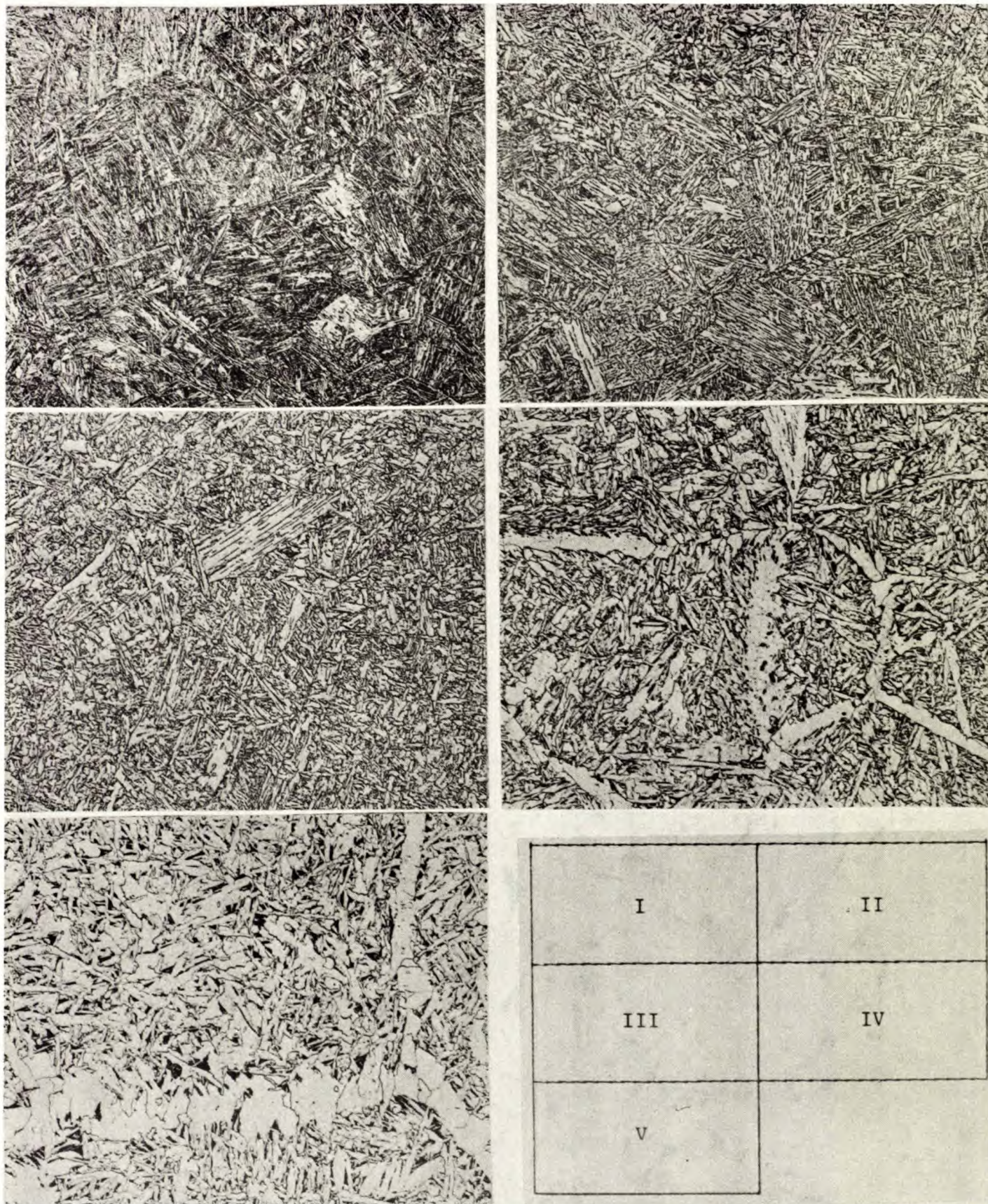


Fig. II-21 - Optical micrographs, steel F, cooling rates I-V nital etch, x200



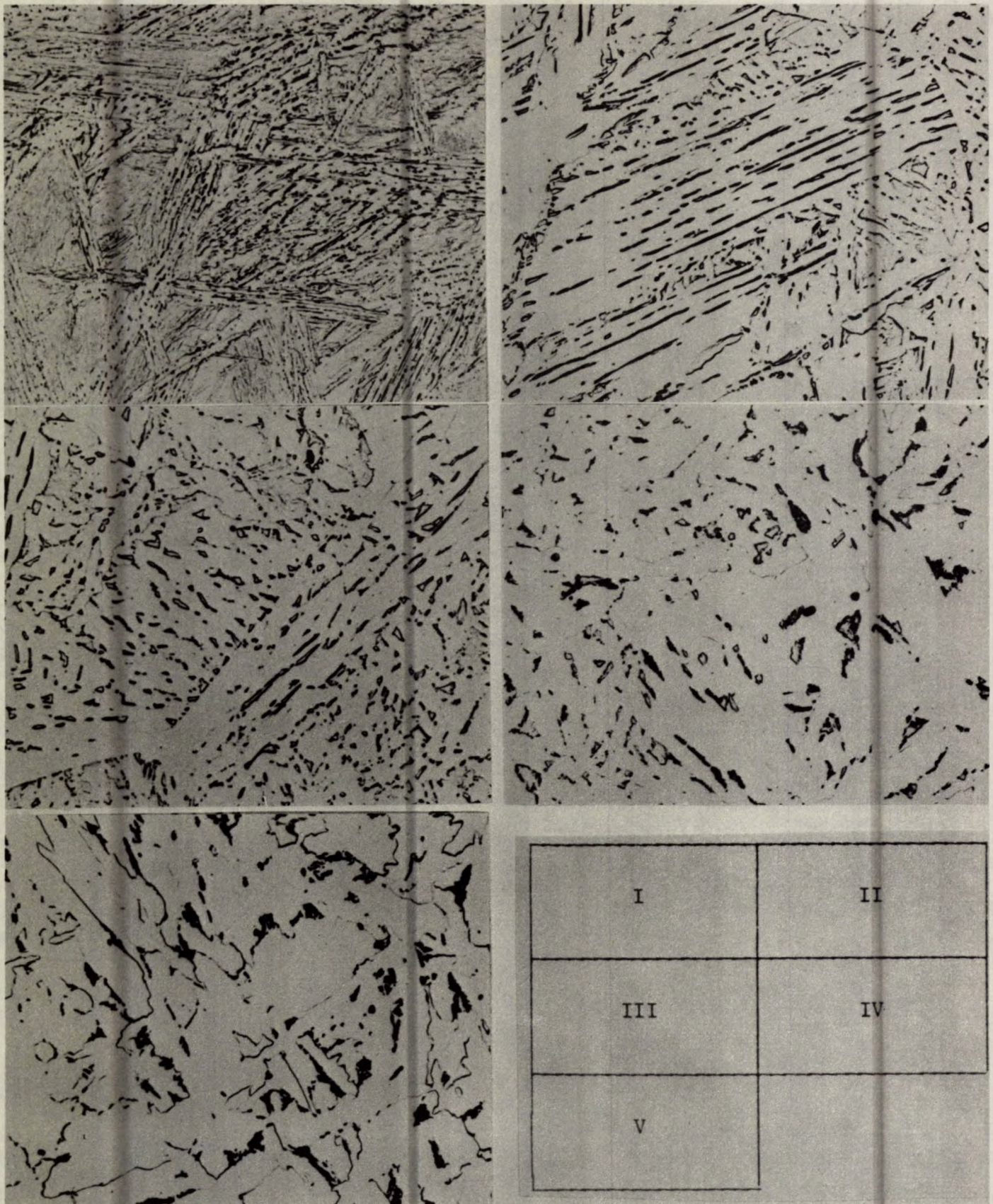


Fig. II-22 - Optical micrographs, steel F, cooling rates I-V picral etch, x1000



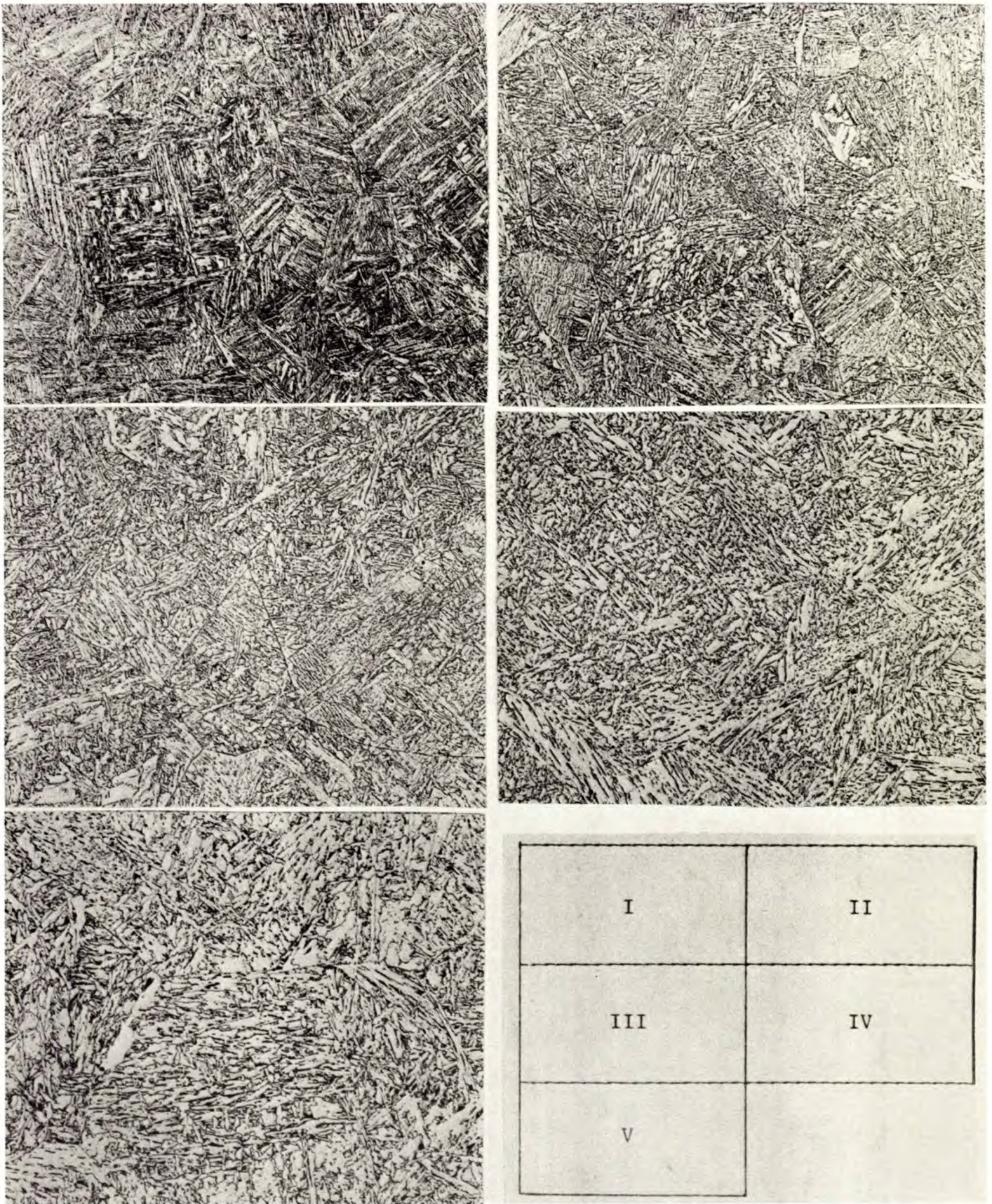


Fig. II-23 - Optical micrographs, steel G, cooling rates I-V nital etch, x200



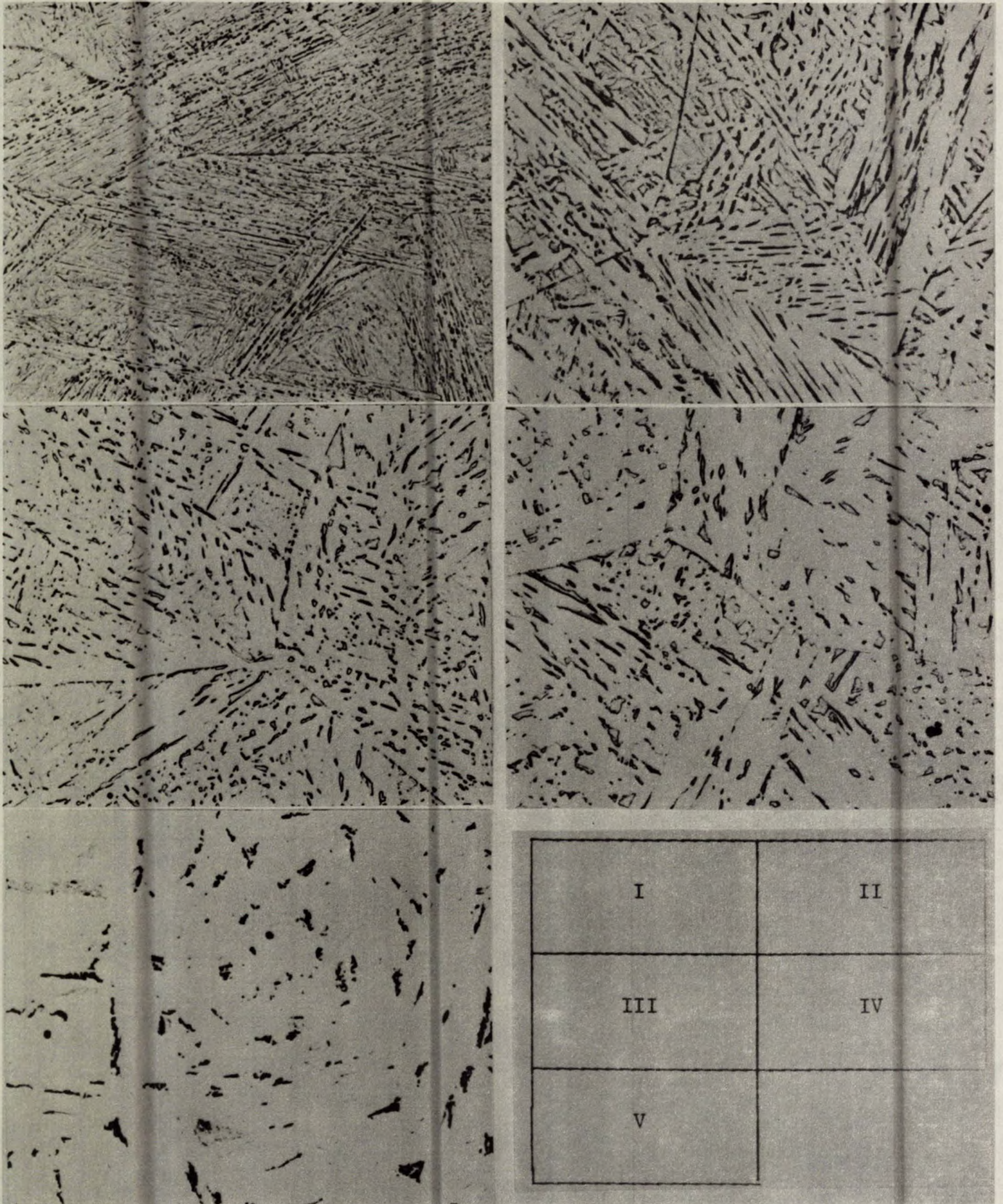


Fig. II-24 - Optical micrographs, steel G, cooling rates I-V picral  
etch, x1000



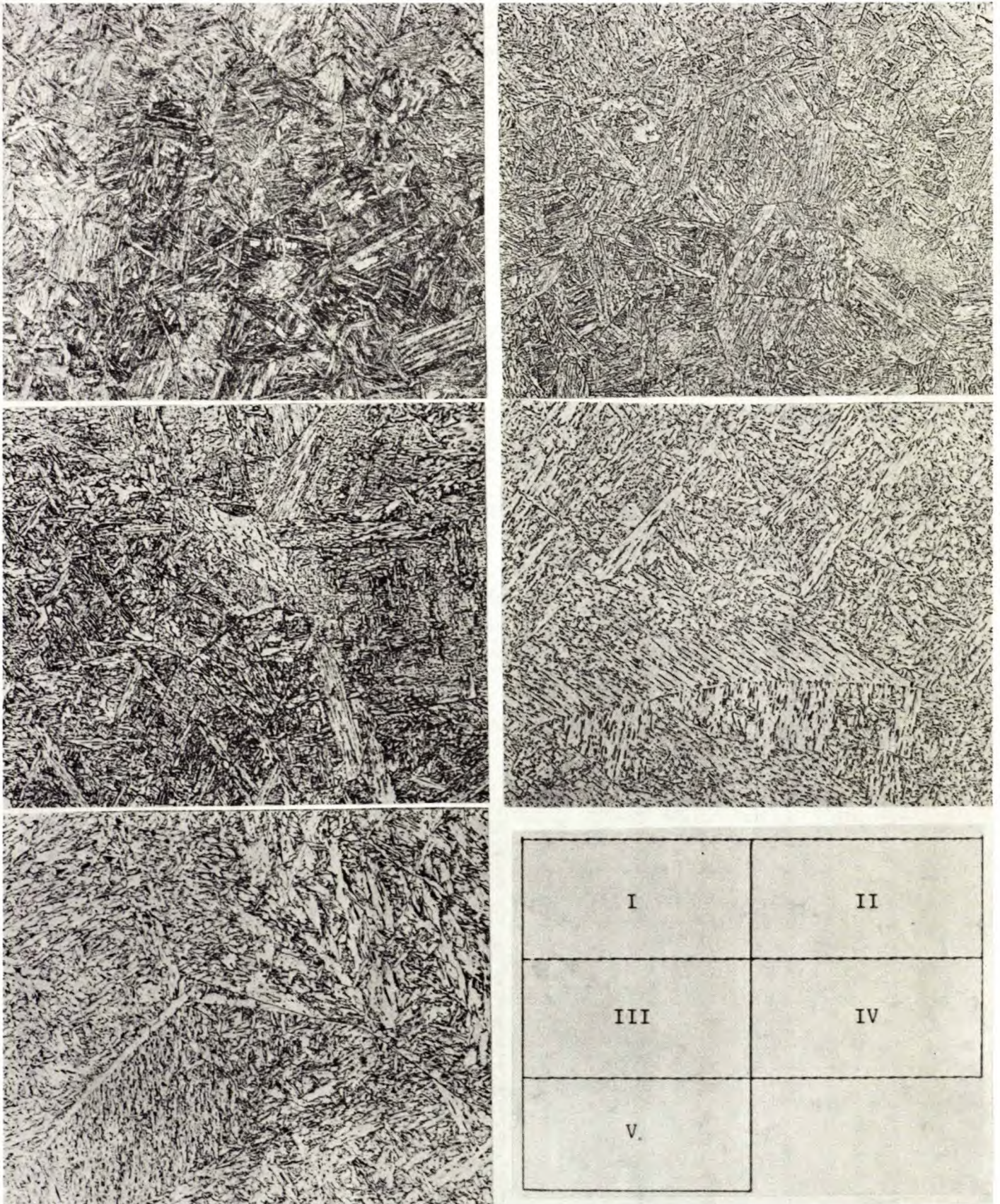


Fig. II-25 - Optical micrographs, steel H, cooling rates I-V nital etch, x200



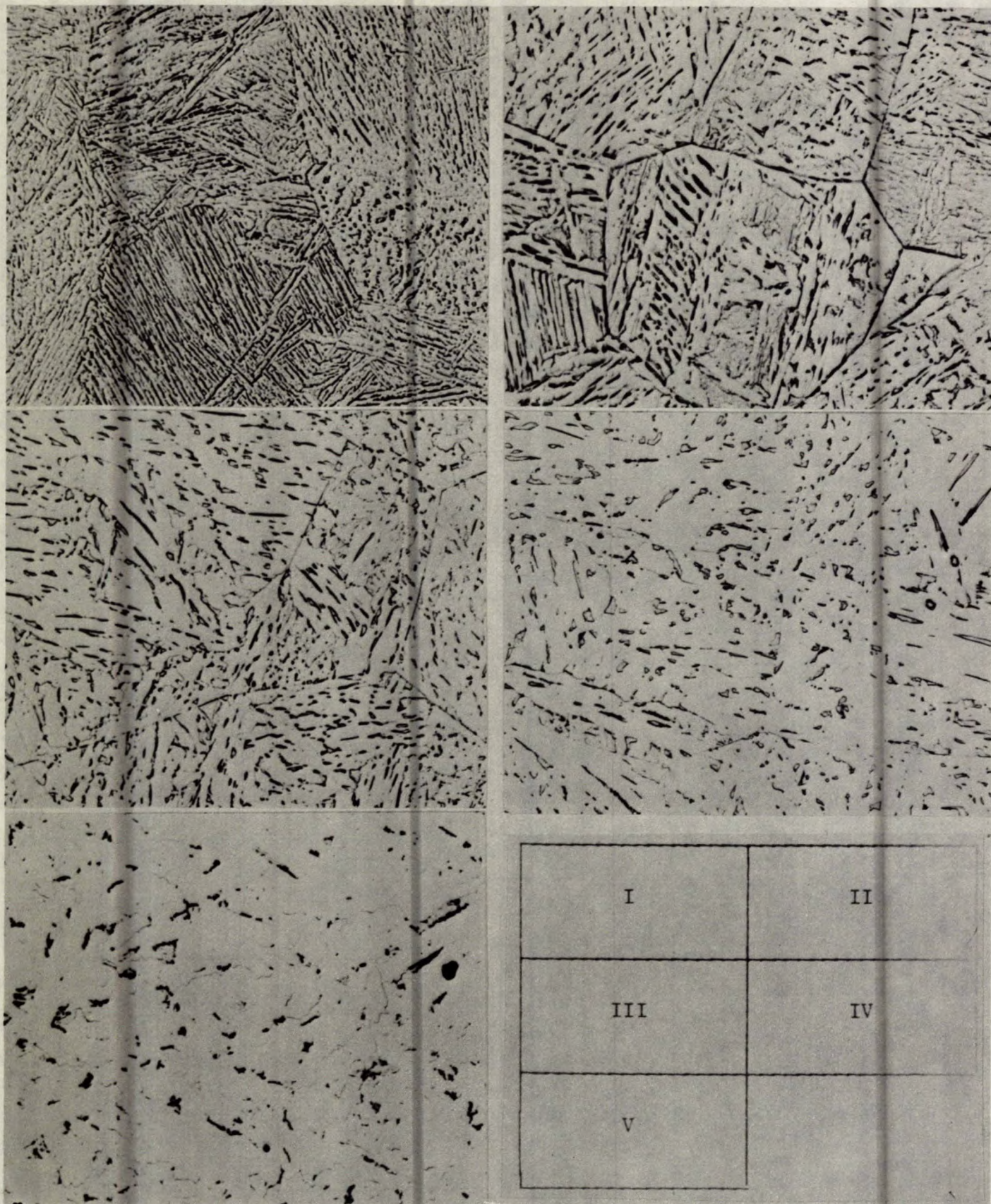


Fig. II-26 - Optical micrographs, steel H, cooling rates I-V picral  
etch, x1000



any cooling rate in these steels, and some M-A persisted even at the longest cooling times.

Table II-2, which obviously involves some simplifications and subjectivity, attempts to summarize all the microstructural observations. It is possible to isolate the following qualitative trends:

Niobium has little effect on the major transformation product but tends to encourage the retention of M-A. Vanadium promotes the formation of a more randomly-orientated bainitic ferrite at slow cooling rates. Molybdenum eliminates

the formation of grain-boundary ferrite and promotes the retention of M-A.

The effects of chemical composition on transformation temperatures are summarized in Fig. II-27. In this figure, 5% and 95% transformation temperatures are used as they are more indicative of the overall transformation conditions and less influenced by minor microconstituents formed at the beginning and end of the transformation range. The effect of niobium appears particularly clearly in these diagrams. For the two shortest cooling times, niobium has little or no

Table II-2 - Microstructure of dilatometer samples

Steel		Cooling rate				
		I	II	III	IV	V
A	Structure	M + B(P)	B(P)+m	gbf+B(P)+m	GBF+B(R)	GBF+B(R)
	Carbon-rich zones	M-A	M-A	M-A + c	C	C
B	Structure	M + B(P)	B(P)+m	B(P)+m	gbf+B(R)	GBF+B(R)
	Carbon-rich zones	(unresolved)	M-A	M-A + c	M-A+C	C+ma
C	Structure	M + B(P)	B(P)+m	B(P)	gbf+B(R)	gbf+B(R)
	Carbon-rich zones	(unresolved)	M-A	M-A	M-A+C	C+ma
D	Structure	M + B(P)	B(P)	B(P)	gbf+B(P)	GBF+B(R)
	Carbon-rich zones	M-A	M-A	M-A	M-A+c	C+ma
E	Structure	M + B(P)	B(P)+m	gbf+B(R)	GBF+B(R)	GBF+EF
	Carbon-rich zones	M-A	M-A	M-A	C+ma	C
F	Structure	M + b(p)	B(P)+m	B(P)	GBF+B(R)	GBF+B(R)
	Carbon-rich zones	(unresolved)	M-A	M-A	C+M-A	C
G	Structure	M + b(p)	B(P)+M	B(P)+m	B(P)	B(R)
	Carbon-rich zones	(unresolved)	M-A	M-A	M-A	M-A+C
H	Structure	M + b(p)	B(P)+M	B(P)+m	B(P)	B(R)
	Carbon-rich zones	(unresolved)	M-A	M-A	M-A	M-A+C

Key: M: martensite

B(P): bainite consisting primarily of packets of parallel ferrite laths

B(R): coarse bainite consisting of apparently randomly-orientated ferrite

GBF: grain-boundary nucleated, equi-axed ferrite

EF: grain-interior, roughly equi-axed ferrite

M-A: martensite/retained austenite

C: carbide or ferrite-carbide aggregates

Lower case letters denote minor constituents

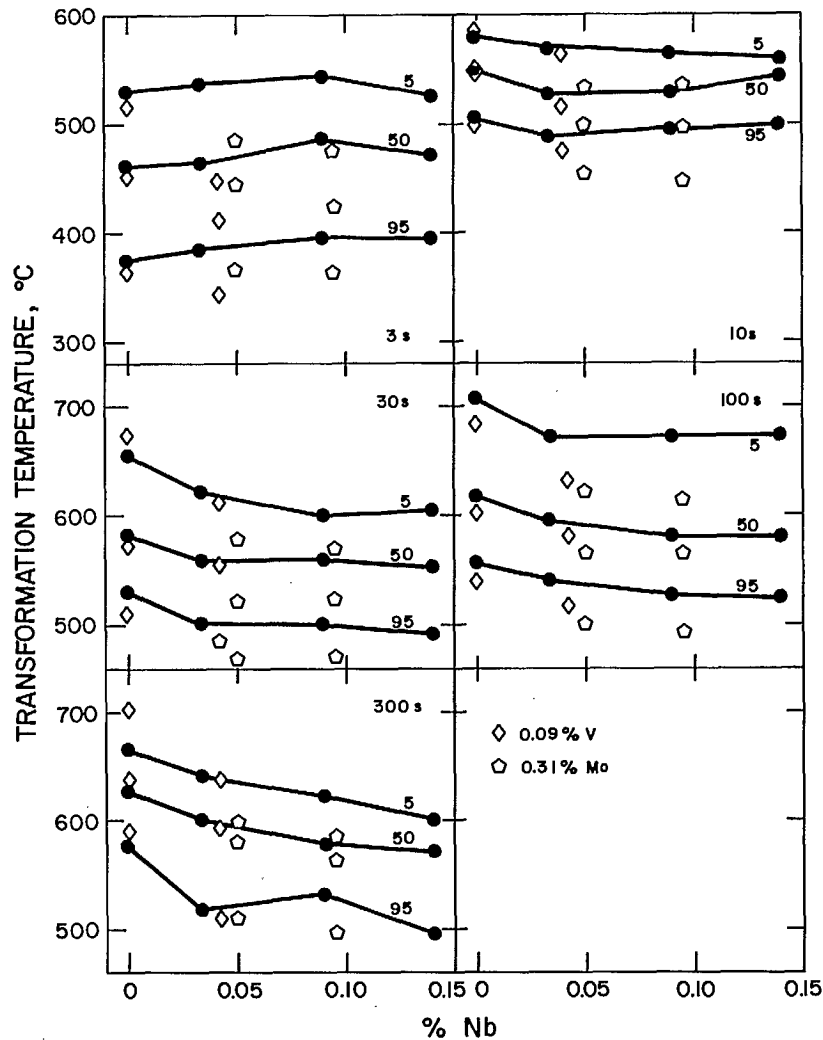


Fig. II-27 - Effect of chemical composition (niobium, vanadium, molybdenum) on transformation temperatures

significant influence on transformation temperatures, whereas at longer cooling times, transformation temperatures decrease progressively with increasing niobium content. This decrease appears to be particularly pronounced at a cooling time of 300 s.

These observations can be logically accounted for in terms of the time available for dissolution of niobium carbide at the peak temperature. For example, the times spent above 1000°C for the five cycles were 7, 8, 41, 130, and 390 s, respectively. It is quite plausible that little or no niobium is taken into solution for cycles I and II, whereas cycles III and IV allowed a progressively greater degree of dissolution.

Vanadium alone appears to have very little effect on transformation behaviour except, as noted above, to raise transformation temperatures at very slow cooling rates. The latter observation is unexpected, but the tendency of vanadium to promote the formation of polygonal ferrite in the heat-affected zone of high heat input welds has been noted before (10). In the presence of niobium, vanadium markedly increases the "martensitic hardenability", and thus results in a considerable drop in transformation temperatures at the fastest cooling rate. There is also a considerable reduction in transformation temperature at a cooling time of 100 s, which is not readily explained.

Molybdenum, as might be expected, causes

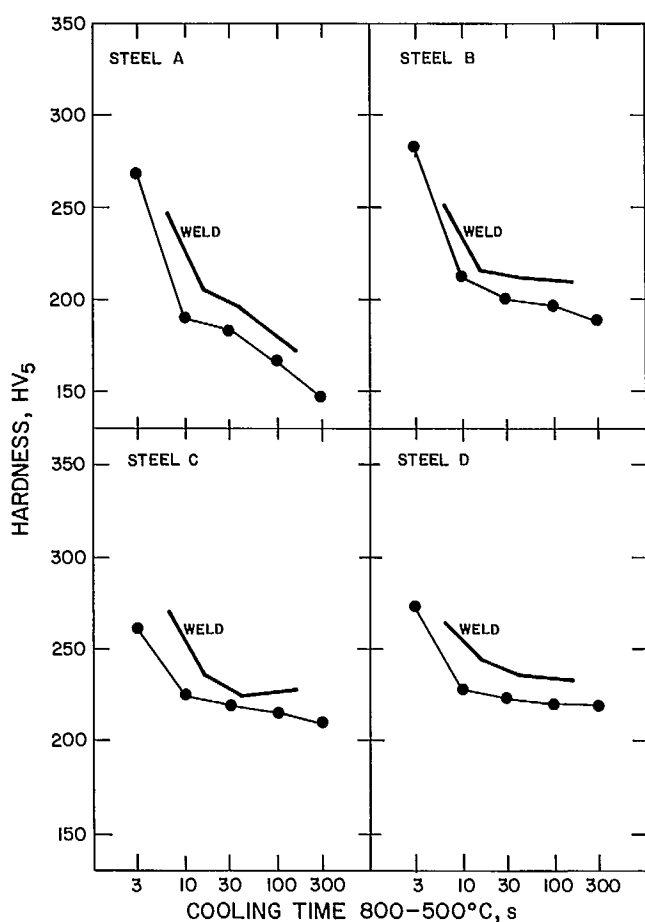


Fig. II-28 - Variation of hardness with cooling time (800-500°C), steels A-D

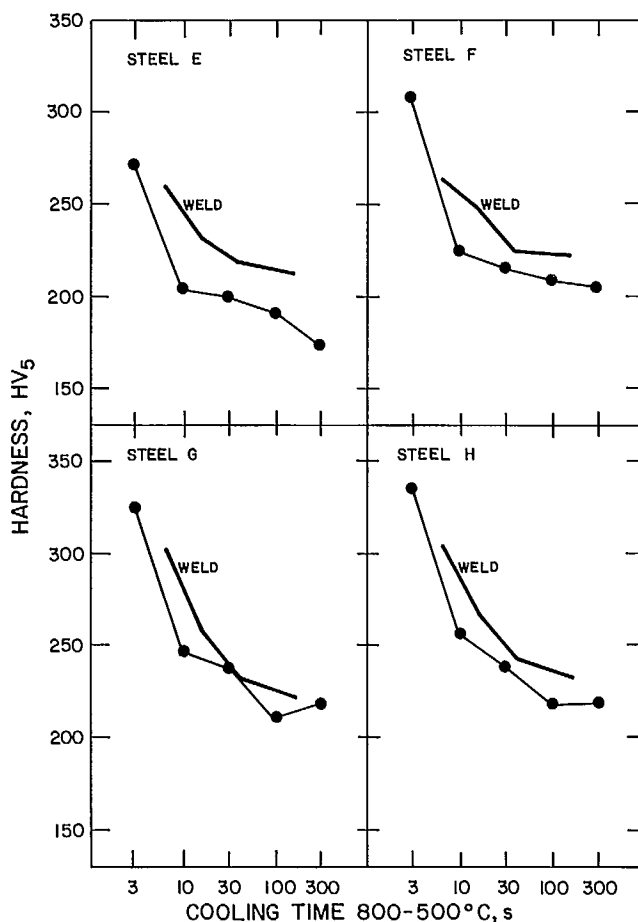


Fig. II-29 - Variation of hardness with cooling time (800-500°C), steels E-H

a substantial decrease in transformation temperatures under all cooling conditions; this effect appears to be practically independent of niobium content.

Figures II-28 and 29 show the variation in hardness with cooling time for the eight experimental steels; also shown are the experimental maximum values measured in the heat-affected-zones of real welds. The dilatometer results show broadly the same trends as those from the welds but generally at slightly lower hardness values. It is difficult to account in detail for this discrepancy, but there are two factors which may be significant apart from the differences in details of the thermal cycles mentioned above. First, there is an instantaneous temperature gradient across the real weld HAZ so that

the transformation characteristics of any given point may be influenced by adjacent regions at a lower temperature, or in the case of the coarse grained HAZ, by the weld metal. More importantly, the hardness values shown for the real welds are "maximum" values and, thus, refer to points very close to the fusion boundary; "maximum" hardness values can be typically 20-30 points higher than average. It is interesting to note that the expected hardness for virgin martensite, estimated at around 370HV in these steels, was not approached even in steels F, G and H, despite their prevalently martensitic microstructure at the fastest cooling rate. However, with an  $M_s$  temperature around 470°C, very rapid cooling to room temperature would be needed to avoid substantial autotempering, and the values reached in

steels G and H ( $\sim 330\text{HV}$ ) are close to the maximum usually observed for practical cooling conditions in 0.1% C steels.

Figure II-30 shows the hardness of the dilatometer samples as a function of 50% transformation temperature. This has been shown in previous work to be a reasonable expression of overall transformation behaviour, though, clearly, no single parameter can be fully adequate for this purpose (5). With the exception of steel B (0.034% Nb) and one anomalous point for steel F, the results for all niobium-containing steels fall approximately within the band determined in an earlier dilatometric study on steels containing 0.06% Nb or 0.03% Nb, 0.07% V (11). In general, the present results fall at the bottom end of, or a little below, a band obtained in a wider ranging study using Gleeble simulation (5). As observed in that study, however, consistently higher hardnesses were obtained in the microalloyed steels than in the reference plain-carbon material. There may be some tendency for this difference to peak at around 580–600°C, and it

could readily be explained for the higher transformation temperature by reprecipitation of microalloy carbides dissolved during the high-temperature portion of the thermal cycle. However, the difference appears to persist at least down to transformation temperatures around 450°C, where precipitation of microalloy carbides during cooling would be very unlikely; given the very short time at high temperature associated with the faster thermal cycles, it may be that a sufficient precipitate dispersion to give rise to some hardness increment is preserved throughout the thermal cycle. Alternatively, solid solution effects may be involved, although small concentrations of substitutional solutes are unlikely to give rise to significant hardening.

#### Conclusions

At the fastest cooling rates studied, microstructures are predominantly martensitic or mixtures of martensite and bainite consisting of packets of parallel ferrite laths. These structures are consistent with the observed transfor-

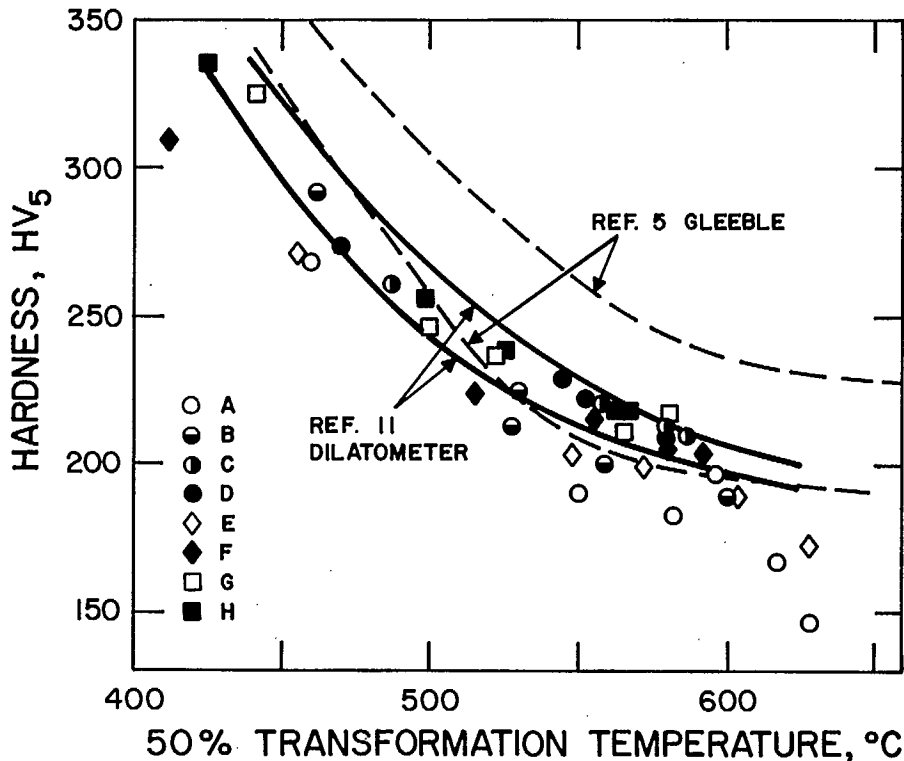


Fig. II-30 - Variation of hardness with 50% transformation temperature

mation temperatures and the calculated  $M_s$  temperature of 470-480°C. As the cooling rate decreases and the transformation temperatures rise, martensite is progressively replaced by bainite. At the higher transformation temperatures, the parallel-lath bainitic structure tends to give place to an apparently random structure. In addition, carbide aggregates begin to appear instead of the martensite/retained austenite (M-A) seen at the lower temperatures. Grain-boundary ferrite is generally present when transformation start temperatures rise above 680-700°C. Niobium appears to have limited effects on gross microstructure but tends to promote the retention of some M-A to slower cooling rates. Vanadium appears to increase the tendency towards the formation of more randomly oriented ferrite at slow cooling rates, whereas molybdenum completely eliminates grain boundary ferrite and leads to the retention of significant amounts of M-A even at the slowest cooling rates.

Niobium has little influence on transformation temperatures at fast cooling rates, but leads to a progressive decrease in transformation temperature at slower cooling rates. This may be explained by the differences in the high-temperature portion of the thermal cycles and by the solubility characteristics of niobium carbide. Vanadium has little effect in the absence of niobium, but in the presence of niobium causes a significant decrease in transformation temperature at the fastest cooling rate. Molybdenum reduces transformation temperatures for all thermal cycles.

Hardness varies with cooling rate in broadly the same way as in the HAZ of real welds, but hardness values are uniformly lower in the dilatometer samples. The hardness expected in a 0.1% carbon virgin martensite is not approached even in those steels which showed predominantly martensitic microstructures at the fastest cooling rate. This could be explained by the presence of some bainitic regions, and by the probable occurrence of a substantial degree of auto-tempering during the relatively slow cooling between  $M_s$  and room temperature.

Hardness varies inversely with 50% transformation temperature, the microalloyed steels show higher hardness than the plain carbon-manganese steel at virtually all transformation temperatures. Whereas this could be explained by dissolution and reprecipitation of niobium carbide for the higher transformation temperatures, the explanation is not plausible at lower temperatures. In these instances, the retention of precipitate particles throughout the thermal cycle may account for the hardness increment, times within the dissolution range being very short, particularly for the two fastest thermal cycles.

#### Acknowledgements

The dilatometric and metallographic investigation described above was undertaken in collaboration with U. Huggins, whose invaluable cooperation is gratefully acknowledged.

#### References

1. Watkinson, F. and Baker R.G.; Br Weld J; 14:603; 1967.
2. Murry, G., Prudhomme, M. and Constant, A.; Rev Met; 64:559; 1967.
3. Lafrance, M., Prudhomme, M., Murry, G. and Constant, A.; Rev Met; 65:417; 1968.
4. "Note sur la détermination des diagrammes de transformation au refroidissement continu pour l'étude de la soudabilité des aciers": IIS/IIW Document 375-71.
5. Rothwell, A.B. and Bonomo, F. "Welding of line pipe steels"; New York, Welding Research Council; p 118; 1977.
6. Fuji Electronic Industrial Co. Ltd.; Private communication; 1976.
7. Fisher, G.L. and Geils, R.H.; Metallography, 3: p 229; 1970.
8. Steven, W. and Haynes, A.G.; JISI, 183:349; 1956.
9. Rothwell, A.B., Glover, A.G., McGrath, J.T. and Weatherly, G.C.: to be published.
10. Rothwell, A.B.; Internal Report, 1968R; Centro Sperimentale Metallurgico; 1974.
11. Rothwell, A.B.; Noranda unpublished work; 1977.



PART III - SECTION 'A'  
METALLOGRAPHIC ANALYSIS OF  
HAZ MICROSTRUCTURES

by

J.T. McGrath\* and A.G. Glover\*

### Introduction

In the study of HAZ toughness of welds prepared in microalloy steels, the link between toughness properties and microstructure must be established. The objective of Part III of this report is to provide a complete characterization of the features of the HAZ microstructure contained in the following weldments:

- (a) eight steel compositions welded with five heat inputs;
- (b) eight steel compositions welded at a given heat input and stress-relieved at 620°C.

The summary of the metallographic data contained in this part is intended as a companion document to Part I which is a compilation of results of the instrumented impact test program. HAZ toughness properties are linked with microstructure in Part IV.

In addition to the metallographic analysis, the report contains the results of some slow bend crack opening displacement (COD) fracture toughness tests performed on four steel weldments prepared at a similar heat input. The purpose of these tests is to provide a comparison between the results of fracture toughness tests carried out at low and high strain rates.

### Experimental

#### Metallographic analysis

##### Materials

Submerged-arc welds prepared in eight steels at five heat inputs were provided for metallographic analysis of HAZ structure. The

composition of the steels and the heat input/-cooling rate data are listed in Table III-1 and III-2.

The HAZ structure of welds prepared in the eight steels with a heat input of 2.4 kJ/mm and stress-relieved at 620°C were examined.

#### Metallographic techniques:

(a) *Optical microscopy* -- Sections were taken through the thickness of the weldment and were mounted and polished using standard techniques. The gross microstructure was revealed by etching in 2 1/2% nital solution. Details of the carbon-containing regions were revealed by preferential etching in saturated picral solution.

When a quantitative assessment of the amount of various transformation products was required, a point-counting technique was used in which 500 counts were taken over 20 areas. In examining the HAZ, the emphasis was placed on characterizing the structure of the coarse grain region immediately adjacent to the fusion boundary. This region is the most significant with respect to HAZ fracture toughness properties, in that the tip of the notch in the impact test specimen is positioned within the coarse grain region.

The objectives of the examination by optical microscopy were to;

- i) identify the gross HAZ microstructure in terms of type and amount of transformation products;
- ii) identify carbon-containing microconstituents;

---

\*Canadian Welding Development Institute, Toronto



Table III-1 - Compositions of experimental steels, wt %

Code	C	Mn	Si	Al	S	P	Nb	V	Mo
A	0.095	1.27	0.175	0.038	<0.005	0.008	-	-	-
B	0.095	1.27	0.175	0.038	<0.005	0.008	0.034	-	-
C	0.085	1.31	0.25	0.044	<0.005	0.009	0.09	-	-
D	0.085	1.31	0.25	0.044	<0.005	0.009	0.14	-	-
E	0.08	1.26	0.235	0.017	0.005	0.007	-	0.09	-
F	0.08	1.26	0.235	0.017	0.005	0.007	0.042	0.09	-
G	0.075	1.34	0.23	0.054	<0.005	0.008	0.05	-	0.31
H	0.075	1.34	0.23	0.054	<0.005	0.008	0.095	-	0.32

Table III-2 - Welding parameters

Code	Energy input kJ/mm	Cooling time, $\Delta t_{800-500^\circ\text{C}}$ s	
30	1.2	6.5	I
36	1.4	16	II
60	2.4	39	III
112	4.4	80	IV
150	7.5	160	V

iii) provide a measure of the prior austenite grain size of the coarse grain HAZ.

(b) *Transmission electron microscopy* --

Specimens for examination in the TEM were prepared by two techniques: (i) thin foil, and (ii) extraction replica.

In the preparation of thin foils, wafers were cut through the thickness of the weld. The wafers, which were initially 0.038 mm (0.015 in.) thick, were reduced to 0.020 mm (0.008 in.) by the thinning action of a chemical polishing solution (80%  $\text{H}_2\text{O}_2$ , 5% HF, 15%  $\text{H}_2\text{O}$ ). Approximately 6-8 disks (3 mm in diameter) were cut out from the wafers by means of a mechanical punch. The disks contained the coarse grain region of

the HAZ. Final electropolishing of the disks was carried out in an automatic Disapol cell, using a solution of 80% methanol and 20% perchloric acid. Polishing conditions were  $-35^\circ\text{C}$ , 35 V, 0.5 A.

The extraction replica technique is covered in Section B.

(c) *Scanning electron microscopy* -- The fracture surfaces of selected specimens were examined by scanning electron microscopy. The fractured faces were electropolished, using the conditions in (b), for  $\sim 1$  min to remove a minimum of surface metal and then etched in 2% nital. This allowed the features of the brittle fracture within the HAZ to be related to the gross microstructure.

COD fracture toughness testing

Slow bend COD tests were carried out on the HAZ coarse grain region of welds in steels A, D, E, and H prepared at a heat input of 7.5 kJ/mm. Specimens, 10 mm x 10 mm x 60 mm, were machined and notched in the same manner as described in Part I. The tip of the fatigue pre-crack was positioned to lie within the coarse grain region of the HAZ.

The specimens were tested in bending with a load/displacement curve being recorded. The critical COD value was determined from the

maximum surface displacement measured from a clip gauge. The maximum surface displacement was recorded either at maximum load, when extensive plastic deformation took place, or at the load associated with abrupt fracture initiation.

The objective of the COD test program was to establish the temperature at which fracture initiation changed from a ductile tearing mode to a rapid, brittle mode. Thus, for each weldment, HAZ COD tests were conducted over a range of temperatures from 25°C to -100°C.

## Results

### Metallographic analysis

The metallographic data for HAZ structures in the as-welded condition will be presented with the steel compositions arranged in the following groupings:

- Group I : weldments from steels A, B, C, and D, allowing the effect of Nb content to be assessed;
- Group II : weldments from steels A and E will indicate the effect of vanadium;
- Group III: weldments from steels B and F will show the effect of vanadium in a Nb bearing steel;
- Group IV : comparing weldments from steels G and B and H and C will allow the effect of Mo in Nb bearing steels to be determined.

So that results of the optical microscopy examination can be related to the metallographic data in Part II on continuous cooling transformation characteristics, the HAZ structures will be presented for each steel weldment as a function of cooling rate.

Group I -- The HAZ microstructure of steels A, B, C and D can be compared in Fig. III-1 to III-8. If one examines the effect of cooling rate on HAZ microstructure for each steel, some general trends emerge. Using steel A

as an example, the HAZ exhibits a coarse bainitic structure with large polygonal ferrite grains along the prior austenite grain boundaries at the slow cooling rates IV and V, (Fig. III-1). As the cooling rate increases, the bainite structure remains the same, but the bainitic ferrite lath width and overall packet size decreases. The smaller packet size relates to the decrease in prior austenite grain size with lowering heat input (Table III-3). The amount of grain boundary ferrite becomes less with increasing cooling rate. At the fastest cooling rate, martensite forms in addition to bainite. The quantitative assessment of the amounts of bainite and martensite at the fastest cooling rate is shown in Table III-4.

The carbon-rich regions in the HAZ are also affected by change in cooling rate. In steel A for example, carbide aggregates form between the bainitic ferrite laths at the slower cooling rates (Fig. III-2). Some of the large carbide-containing regions have the appearance of classical lamellar pearlite. At the faster

Table III-3 - Prior austenite grain size

Cooling rate $\Delta t_{800^\circ - 500^\circ\text{C}}, ^\circ\text{s}$	Grain size $\mu\text{m}$
160	150-160
80	160-170
39	70
16	65
6.5	61

Cooling rate $\Delta t_{800^\circ\text{Z} - 500^\circ\text{ZC}}, ^\circ\text{s}$	Steel	Grain size $\mu\text{m}$
6.5	A	60-66
6.5	B	61-66
6.5	C	51-60
6.5	D	58-65
6.5	E	60-65



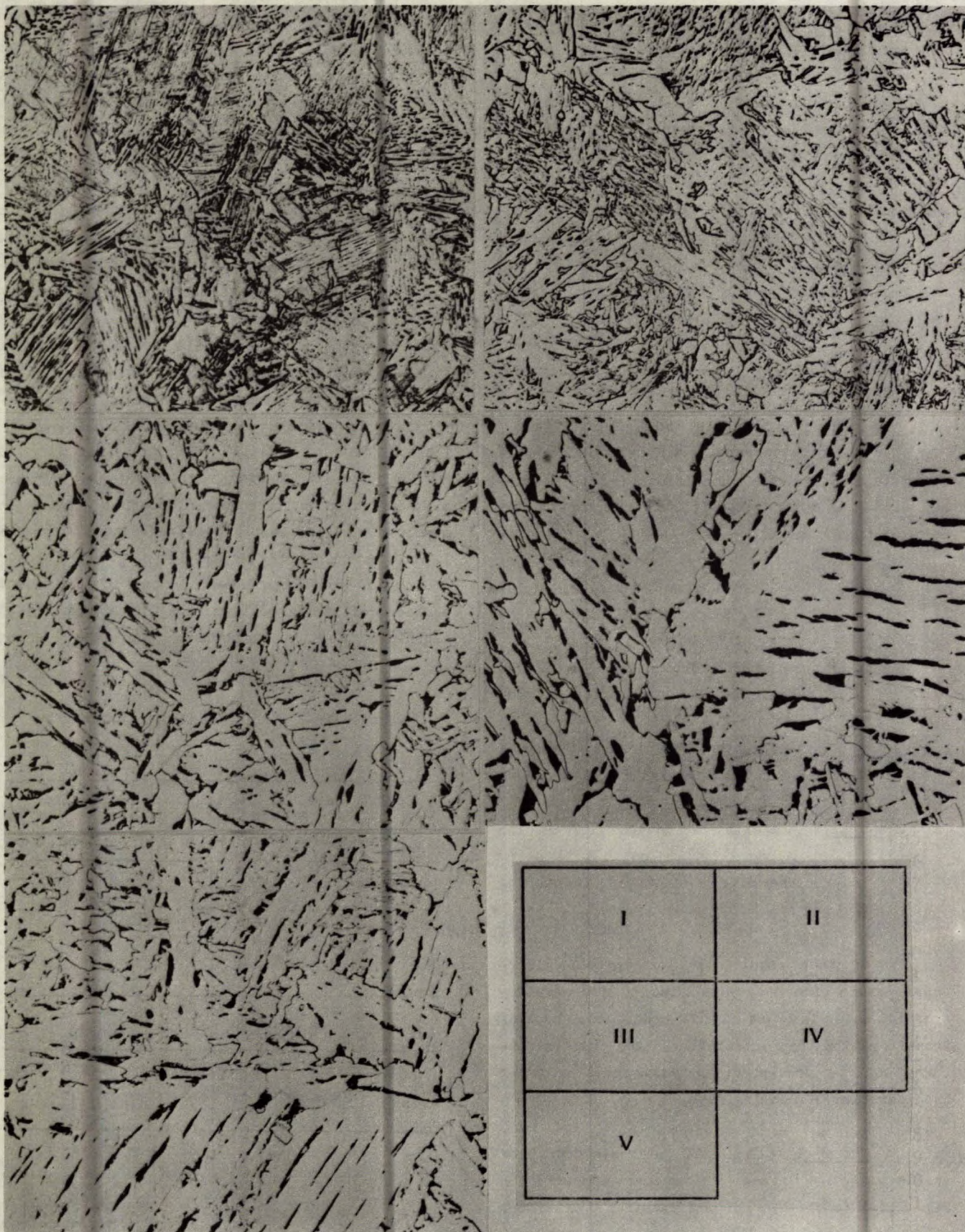


Fig. III-1 - Optical micrographs, steel A heat-affected-zone, cooling rates I-V, nital etch, x500



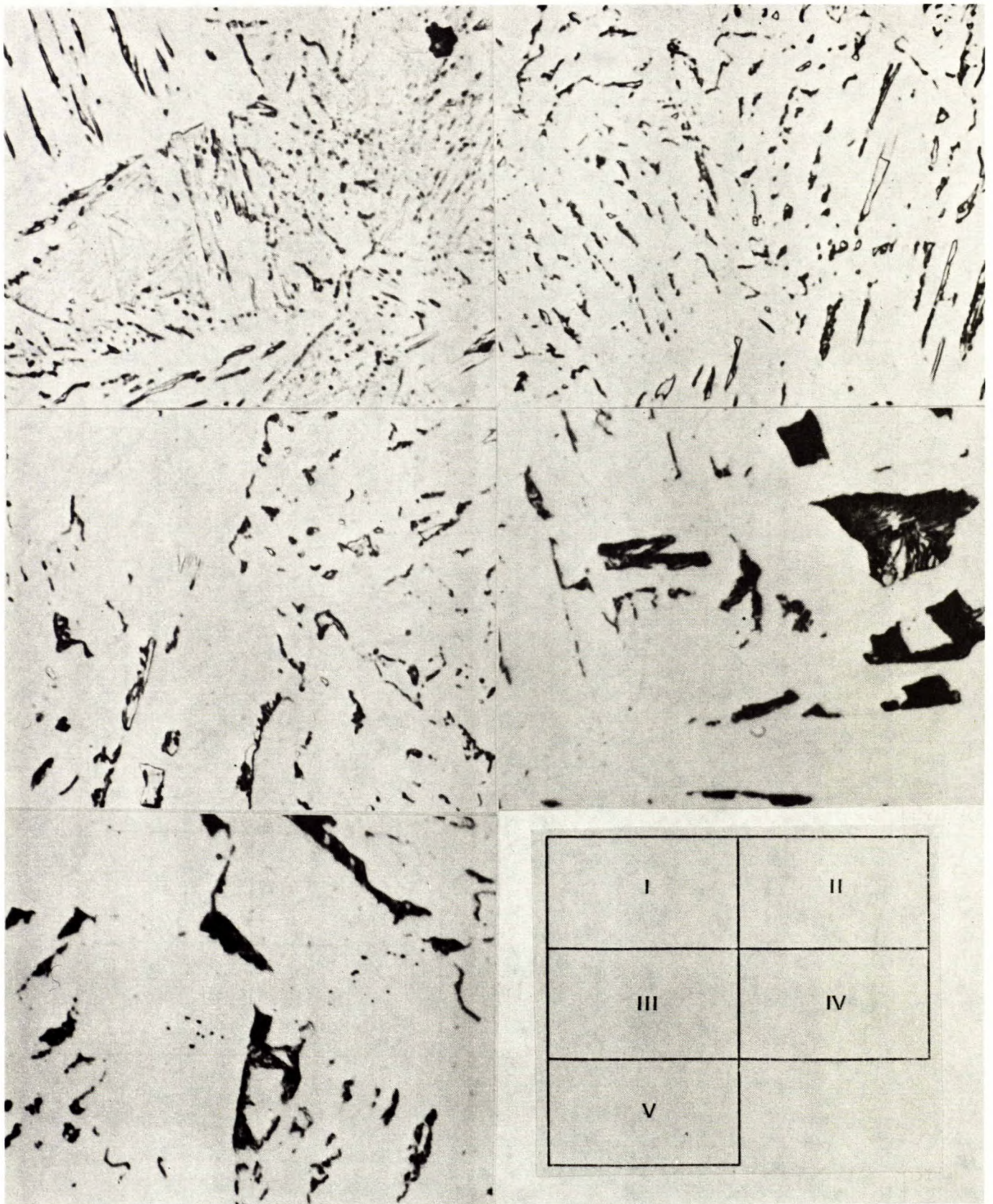


Fig. III-2 - Optical micrographs, steel A heat-affected-zone, cooling rates I-V, picral etch, x2000



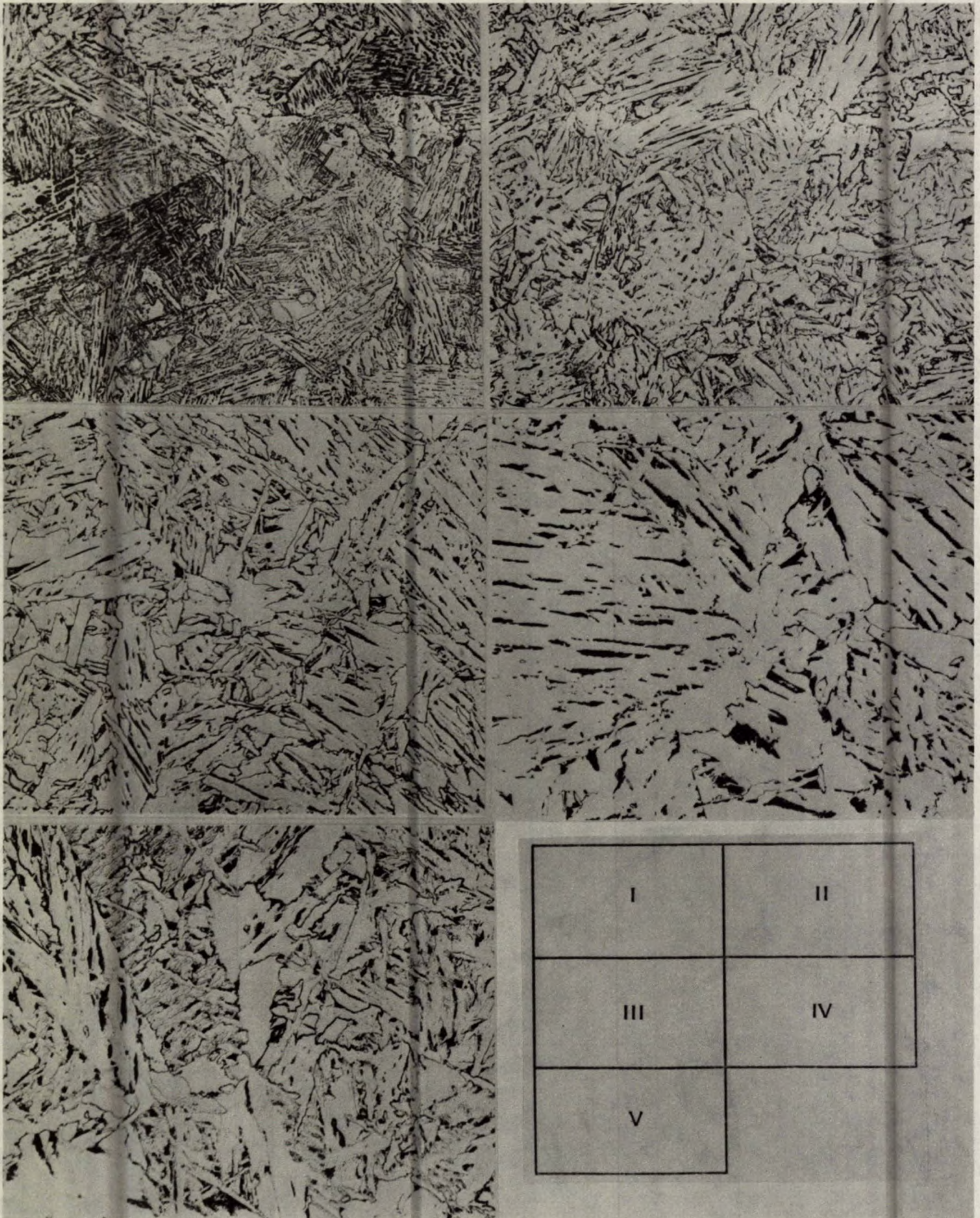


Fig. III-3 - Optical micrographs, steel B heat-affected-zone, cooling rates I-V, nital etch, x500



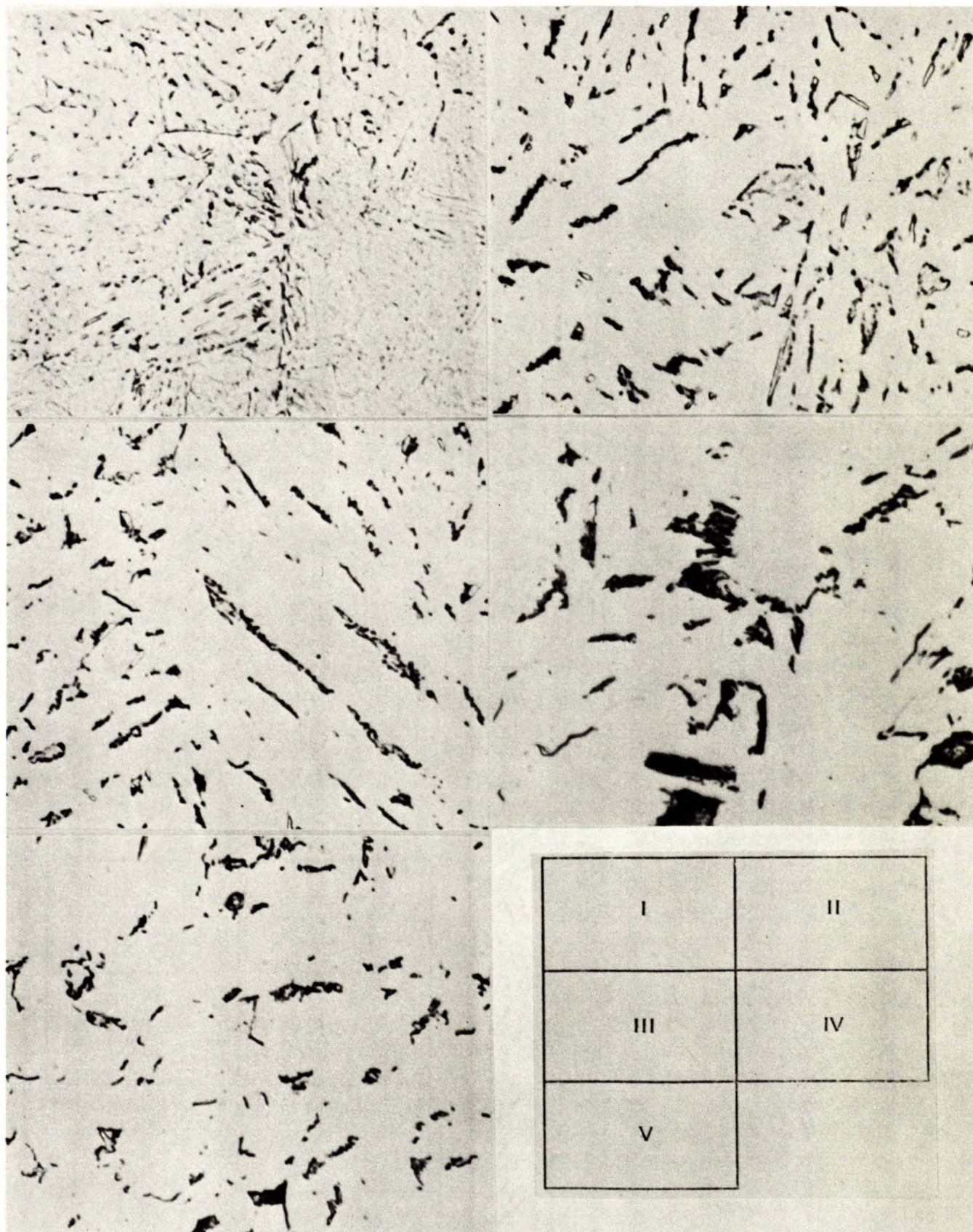


Fig. III-4 - Optical micrographs, steel B heat-affected-zone, cooling rates I-V, picral etch, x2000



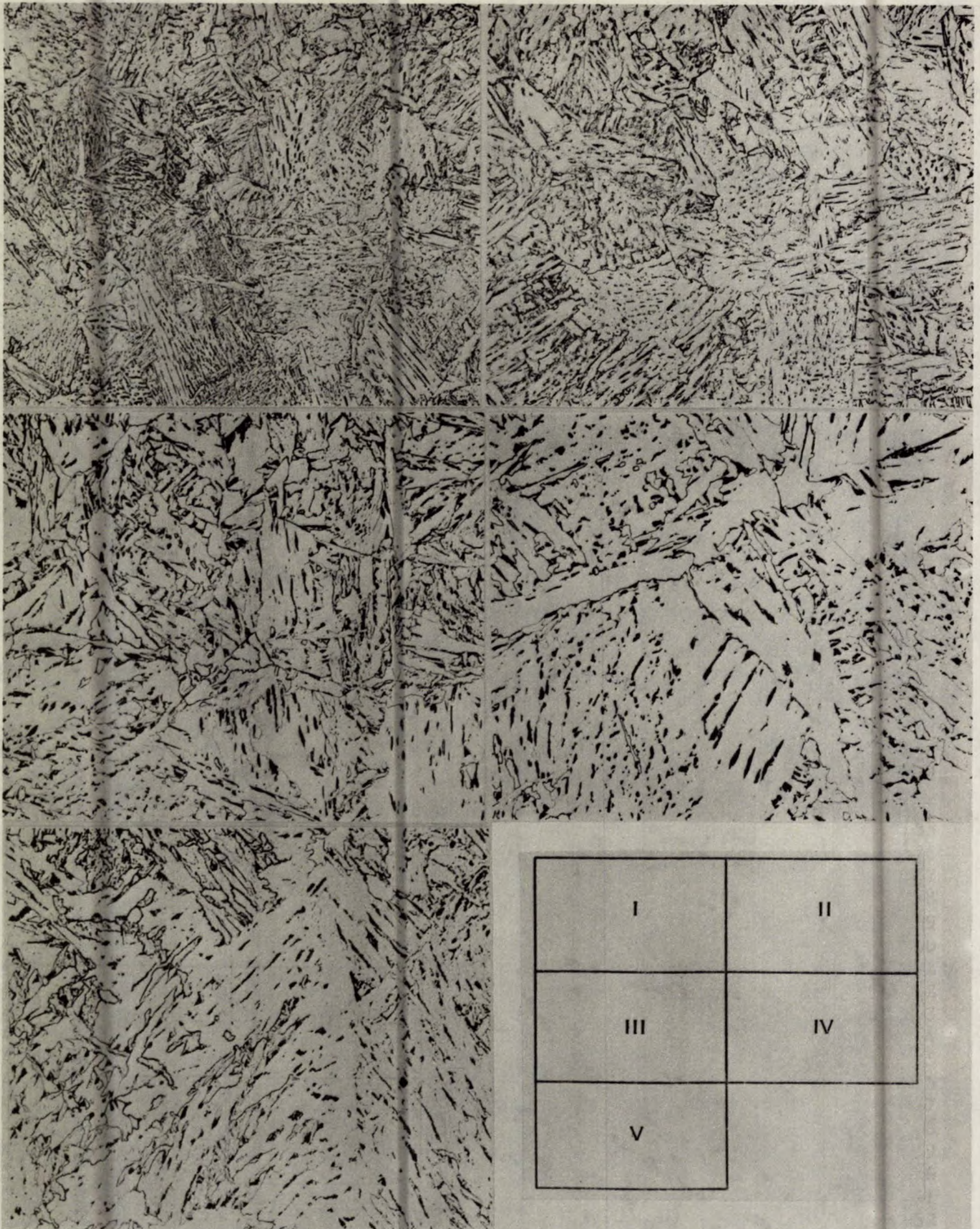


Fig. III-5 - Optical micrographs, steel C heat-affected-zone, cooling rates I-V, nital etch, x500



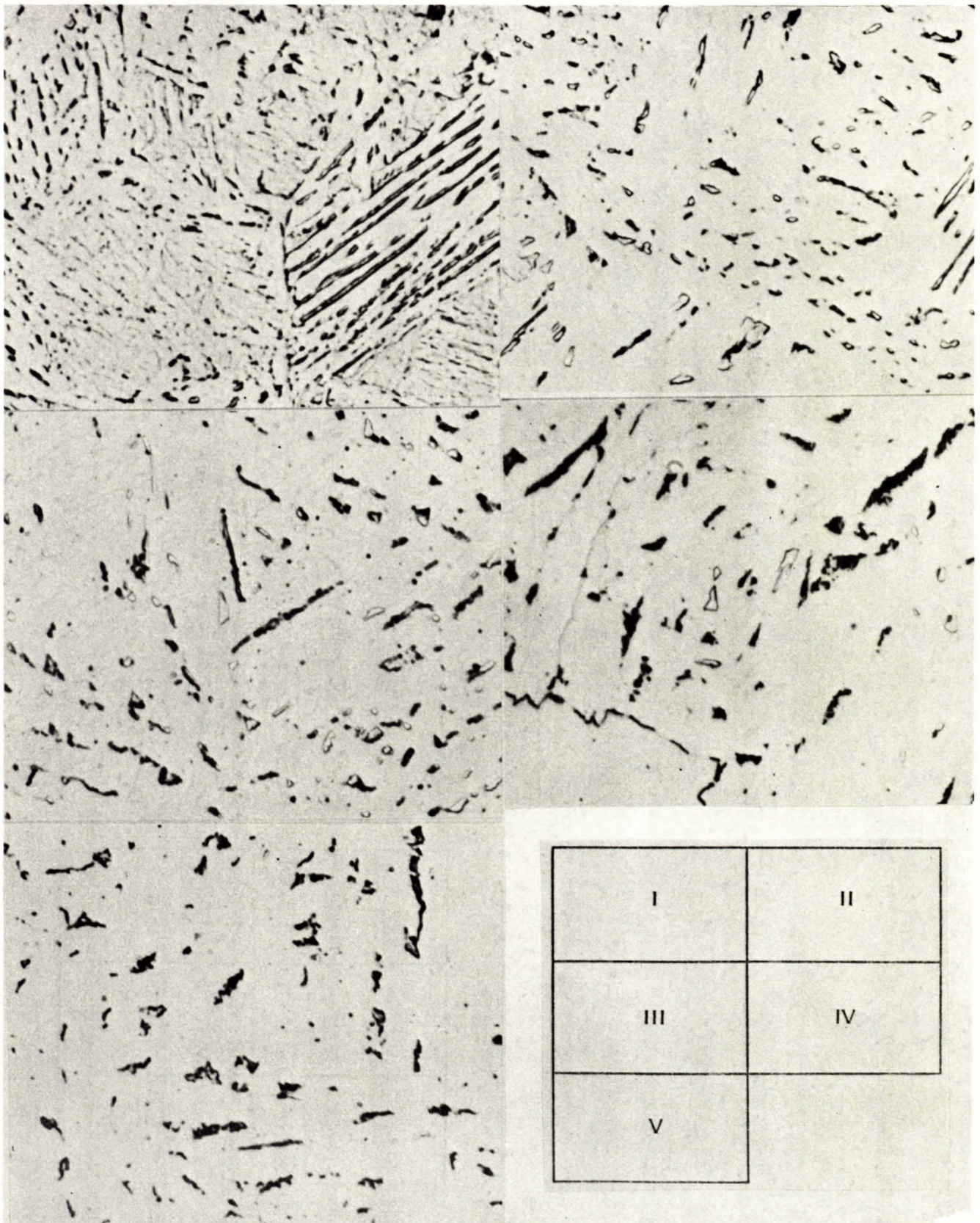


Fig. III-6 - Optical micrographs, steel C heat-affected-zone, cooling rates I-V, picral etch, x2000



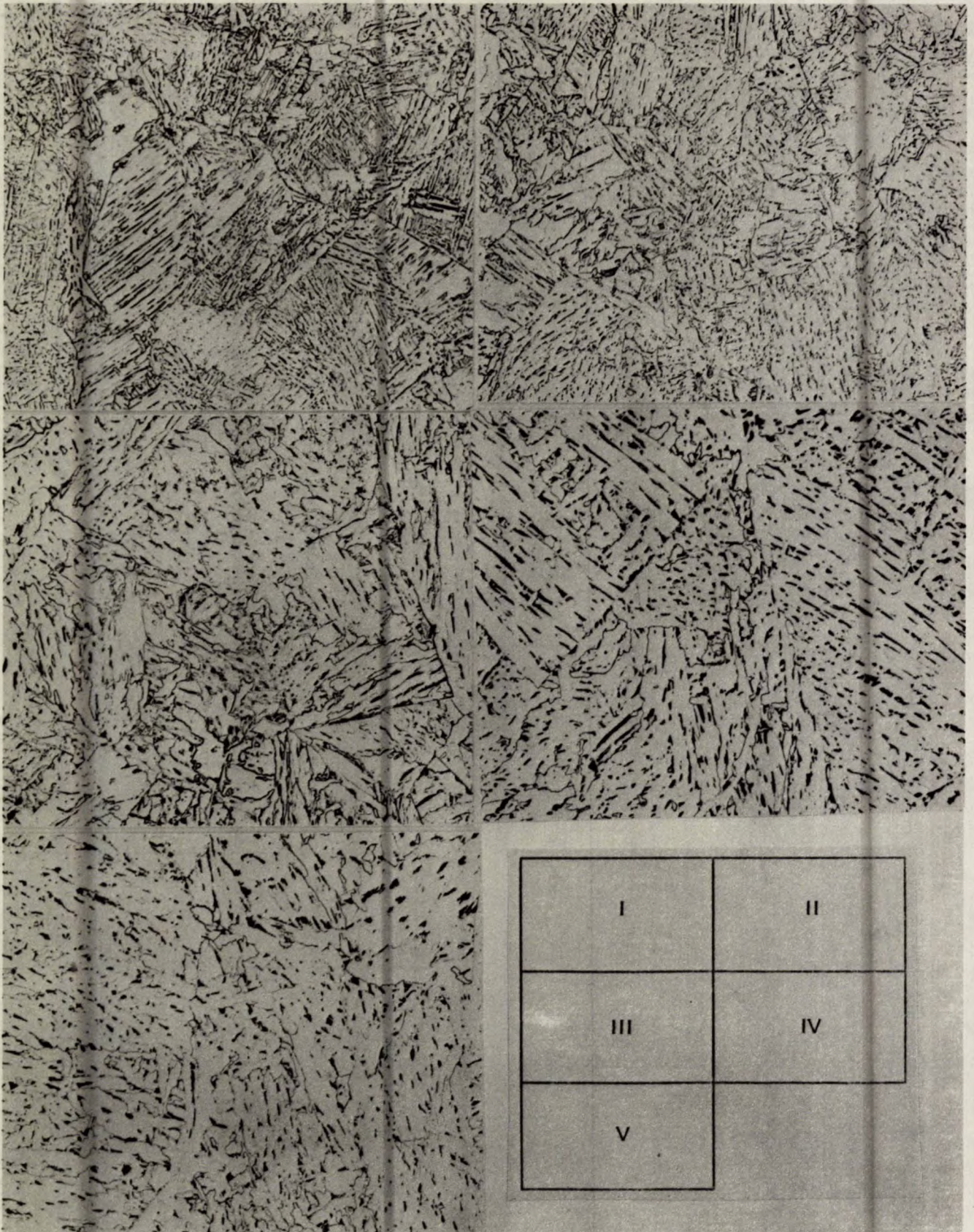


Fig. III-7 - Optical micrographs, steel D heat-affected-zone, cooling rates I-V, nital etch, x500



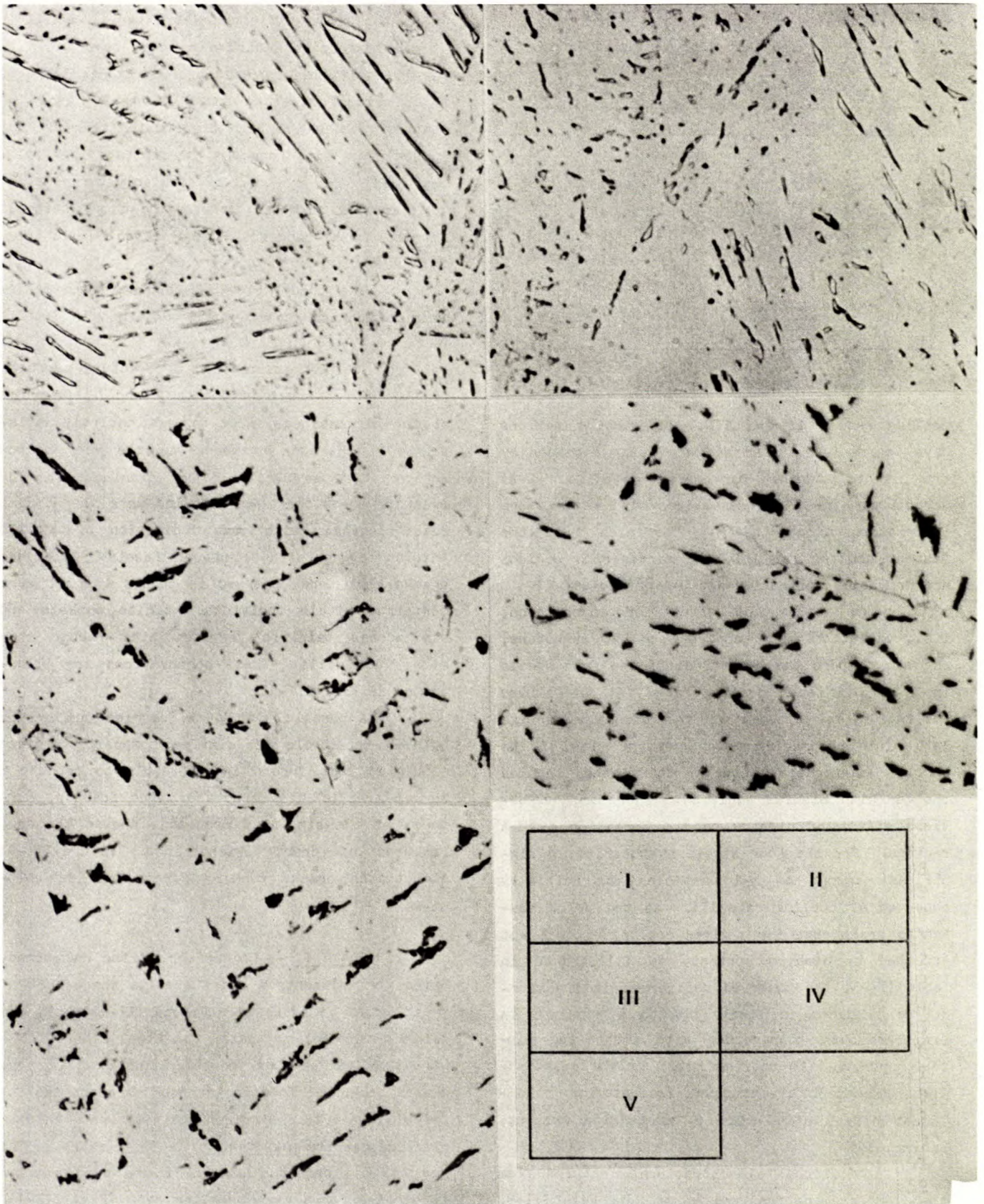


Fig. III-8 - Optical micrographs, steel D heat-affected-zone, cooling rates I-V, picral etch, x2000



Table III-4 - HAZ constituents in weldments  
subjected to cooling rate I

Steel	% Bainite	% Martensite	Other
A	78	20	2
B	78	16	6
C	91	6	5
D	74	18	8
E	52	40	8
F	41	51	8
G	25	74	1
H	29	69	2

cooling rates, II and III, the carbide regions have become much finer and are being replaced by the light etching martensite-austenite (M-A) structure. The TEM observations will reveal more information about the M-A particles. At the fastest cooling rate, I, the carbon-rich regions are primarily martensite and M-A particles.

To assess the effect of composition, i.e., variation in Nb content, on HAZ structure, one can compare the structures of the four steels in Group I at each cooling rate. At the slower cooling rates, IV and V, the bainitic ferrite lath width becomes narrower and the size of the carbide aggregates between the laths becomes smaller with niobium addition. There was no obvious effect of niobium on the formation of M-A regions. For the four steels in question, a significant amount of M-A particles was initially observed at cooling rate III. As the prior austenite grain size for a given cooling rate is not affected by niobium content, as illustrated in Table III-3, the observed refinement in transformation products is likely due to a decrease in transformation temperature with increasing niobium content. At cooling rate, I, the quantitative assessment of structure indicated no significant effect of niobium on martensite content, Table III-4.

Additional microstructural features from the TEM examination are shown in Fig. III-9.

There was only sufficient HAZ material available from weldments made at the highest heat input to permit thin foil preparation. Examination of thin foils of steels A and D in the TEM revealed that the HAZ had a high dislocation density that masked any fine carbide precipitate particles that might be present, particularly in steel D. The lamellar carbides that reside along bainitic ferrite lath boundaries are revealed in Fig. III-9(b).

The observation of carbide precipitates from extraction replicas are contained in Section B.

The SEM examination of fracture surfaces of the HAZ of steel weldments A and D, prepared at the highest heat input was not entirely satisfactory. The main drawback was the very narrow region of  $\sqrt{1}$  mm available for examination. The fracture areas that were studied were essentially quasi-cleavage, with some indication of ductile tearing along with cleavage facets. Cleavage cracks that were observed in steels A and D were contained within individual bainite packets and ran across bainitic ferrite laths rather than along lath walls. These observations are illustrated in Fig. III-10.

A parallel study was carried out by the authors on steels of similar composition given simulated heat inputs in a Gleeble to produce a larger area of HAZ structure. The fracture surfaces of the simulated specimens showed the same features of crack orientation. Figure III-11 illustrates cracks running across bainite colonies.

Group II -- Comparison of the HAZ structures for weldments A and E enables the effect of vanadium to be assessed. Figure III-12 shows the effect of cooling rate on steel E HAZ. The structure ranges from coarse bainite and coarse grain boundary ferrite at the slower cooling rates, IV and V, to finer bainite and bainite plus martensite at faster cooling rates. The gross HAZ microstructures of E are very similar to steel A for a given cooling rate (Fig. III-1).



Fig. III-9a - High dislocation density in the heat-affected-zone of steel D, TEM, x21 500

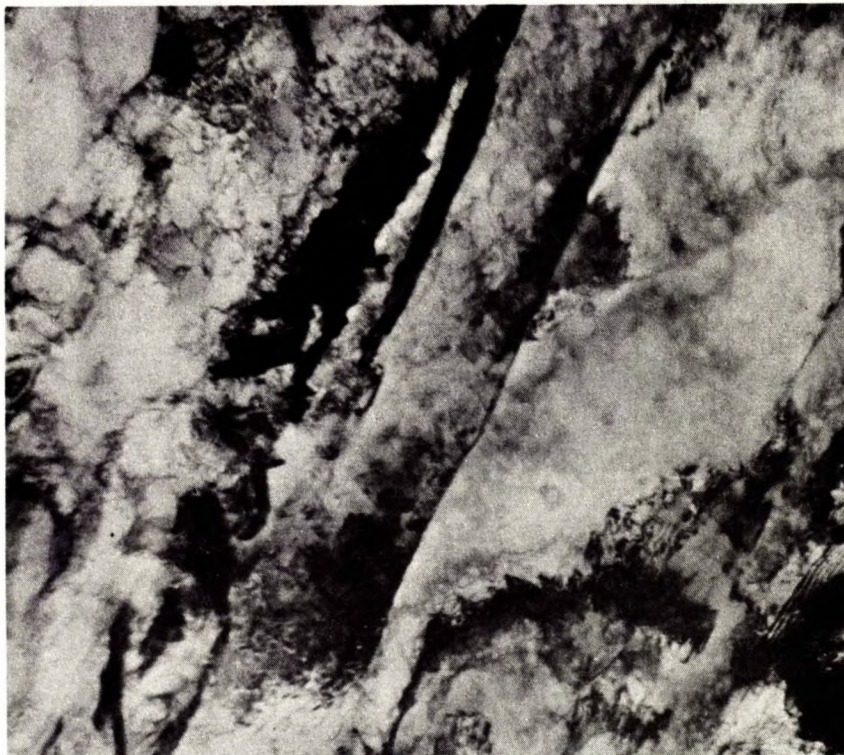


Fig. III-9b - Bainitic structure in the heat-affected-zone of steel A, TEM, x21 500





Fig. III-10 - Cleavage cracks on fracture surface of heat-affected-zone



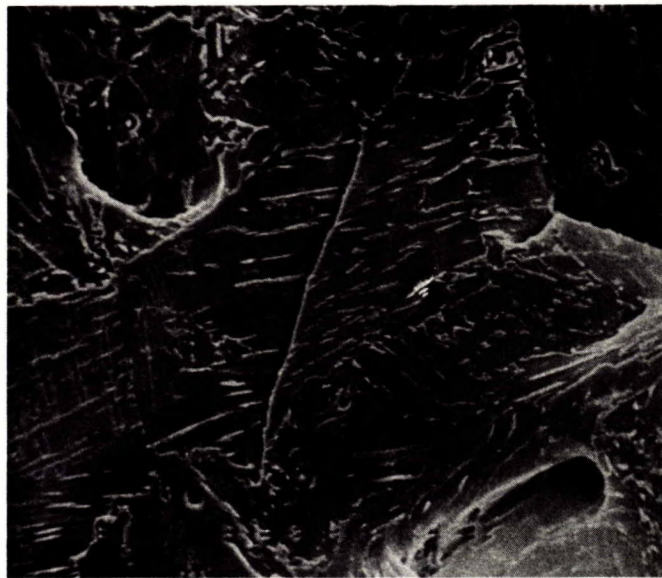
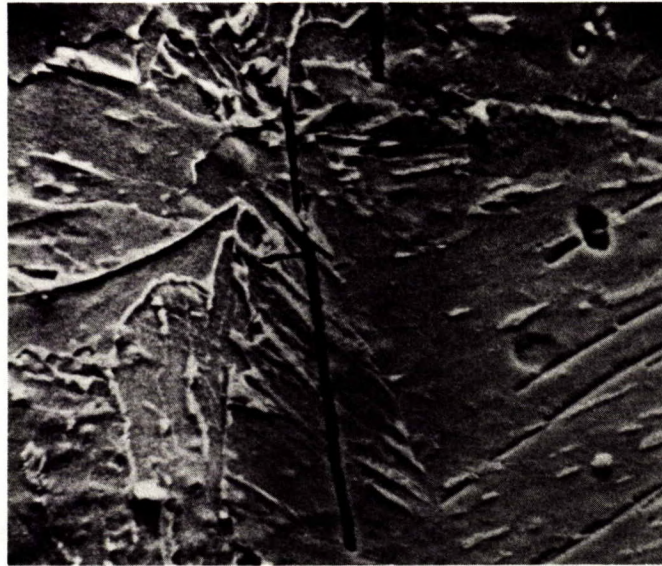


Fig. III-11 - Cleavage cracks cutting across a bainite colony on a fracture surface of a simulated HAZ structure



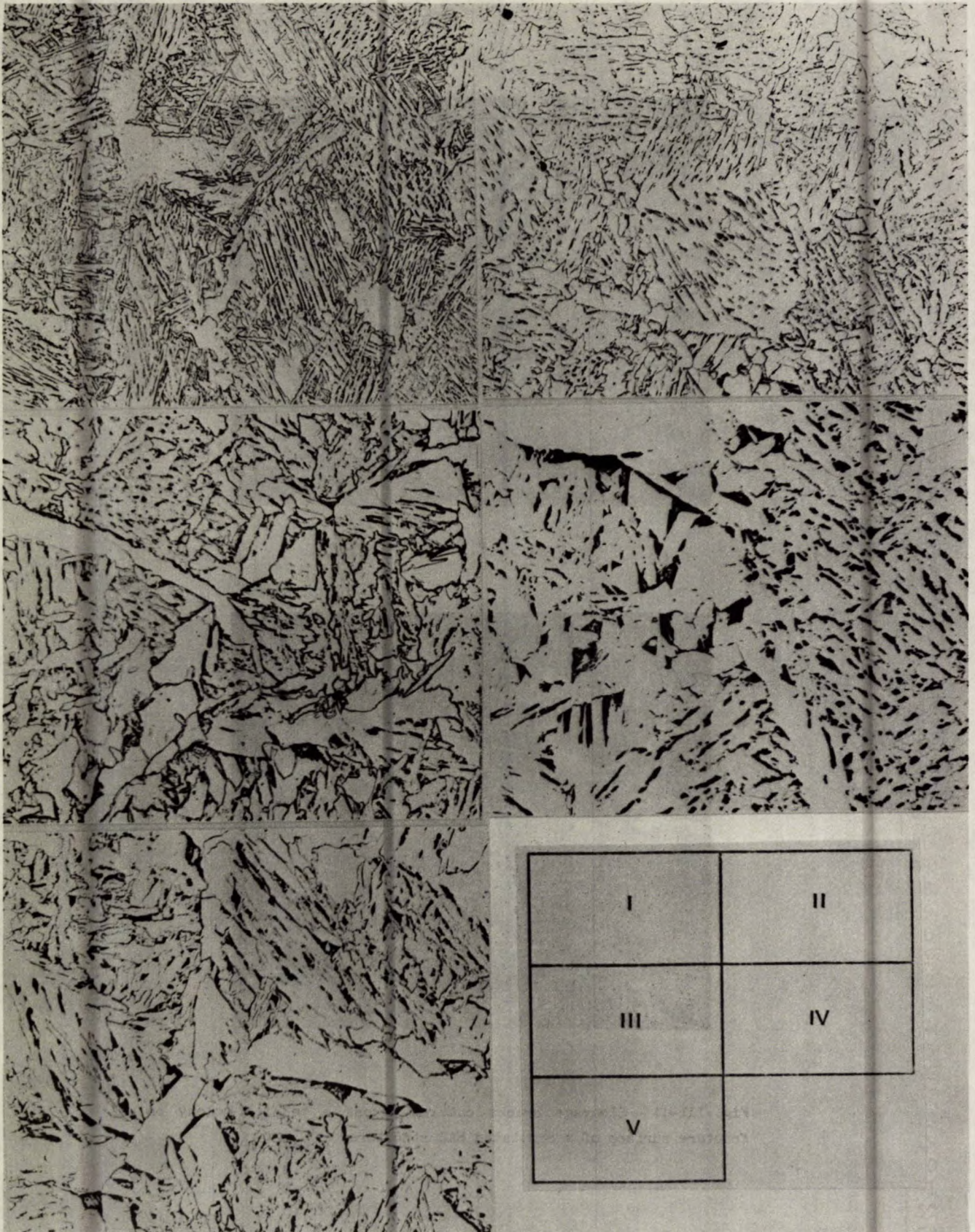


Fig. III-12 - Optical micrographs, steel E heat-affected-zone, cooling rates I-V, nital etch, x500



The quantitative assessment of structure at cooling rate I, Table III-4, indicates a higher martensitic content for steel E than steel A.

The examination of carbon-rich regions of the HAZ of steel E as a function of cooling rate, reveals coarse carbide aggregates at slow cooling rates, fine carbide/M-A regions at the intermediate cooling rates, II and III, and fine M-A particles and martensite laths at the fastest cooling rate, (Fig. III-13). Once again these structures are comparable to those of steel A, HAZ, Fig. III-2.

Group III -- The effect of vanadium on the HAZ structure of niobium-containing steels can be assessed in steels B and F. The gross HAZ microstructure and the structures of the carbon-rich regions as a function of cooling rate are shown in Fig. III-14 and III-15 for weldment F. The same general trend in terms of refinement of structure with increasing cooling rate observed for the other weldments was exhibited by steel F. However, comparing steel F with steel B, it is apparent that, in the carbon-rich regions, steel F has a slightly finer structure (bainitic ferrite lath width) for cooling rate III and slower. There is no significant difference between steel F and steel B in terms of size of carbide aggregates or nucleation of the M-A regions. Steel F has a higher martensite content than steel B at cooling rate I.

Group IV -- In this group the effect of Mo on HAZ structures in steels containing Nb at two levels can be determined, i.e., compare steel G with B and steel H with C. The gross HAZ structures of weldment G as a function of cooling rate are shown in Fig. III-16. In comparing structures directly with steel B (Fig. III-3) the following observations can be made:

- (a) the HAZ structure in steel G is predominantly bainitic with very small amounts of polygonal ferrite along grain boundaries;
- (b) the ferrite lath width is much narrower in steel G; and

(c) steel G HAZ has a higher martensite content than steel B at cooling rate I.

The main observation in examining the carbon-rich regions in Fig. III-17 is the presence of M-A particles, even at slow cooling rates IV and V, in steel G HAZ, whereas in steel B, it was necessary that cooling rate II be achieved before M-A particles became prominent.

The lack of grain boundary ferrite in steel G HAZ suggests that the ferrite nose of the CCT diagram of steel G has been displaced to longer times, thus allowing the austenite to transform entirely to bainite at slow cooling rates. A depression in the bainite start transformation temperature with molybdenum addition would account for the finer bainitic structure. This lower transformation temperature also suggests that carbon diffusion would be more sluggish in steel G, allowing the observed M-A regions to form in preference to carbides.

In examining the HAZ structures of steels H and C, similar observations apply as for steels G and B, the exception being that there is less difference in bainitic ferrite lath width in steels H and C.

Thin foil examination in the TEM reveals the structure of the M-A particles which occurred in steel H HAZ at cooling rate V. In Fig. III-20, twinned martensite within the M-A particles can be observed. The presence of twinned martensite was verified by the split spot selected area diffraction pattern.

#### Stress-relieved HAZ structures

The eight steel weldments prepared by an energy input of 2.4 kJ/mm were stress-relieved at 620°C. While the gross HAZ microstructure remained the same, i.e., predominantly bainitic, changes in the carbon-rich regions were revealed by picral etching. As shown in Fig. III-21 and III-22, spherical carbide precipitates have formed in all eight weldments. The sites of precipitation were between bainitic ferrite laths and along prior austenite grain boundaries. The M-A regions, which were observed in many of the



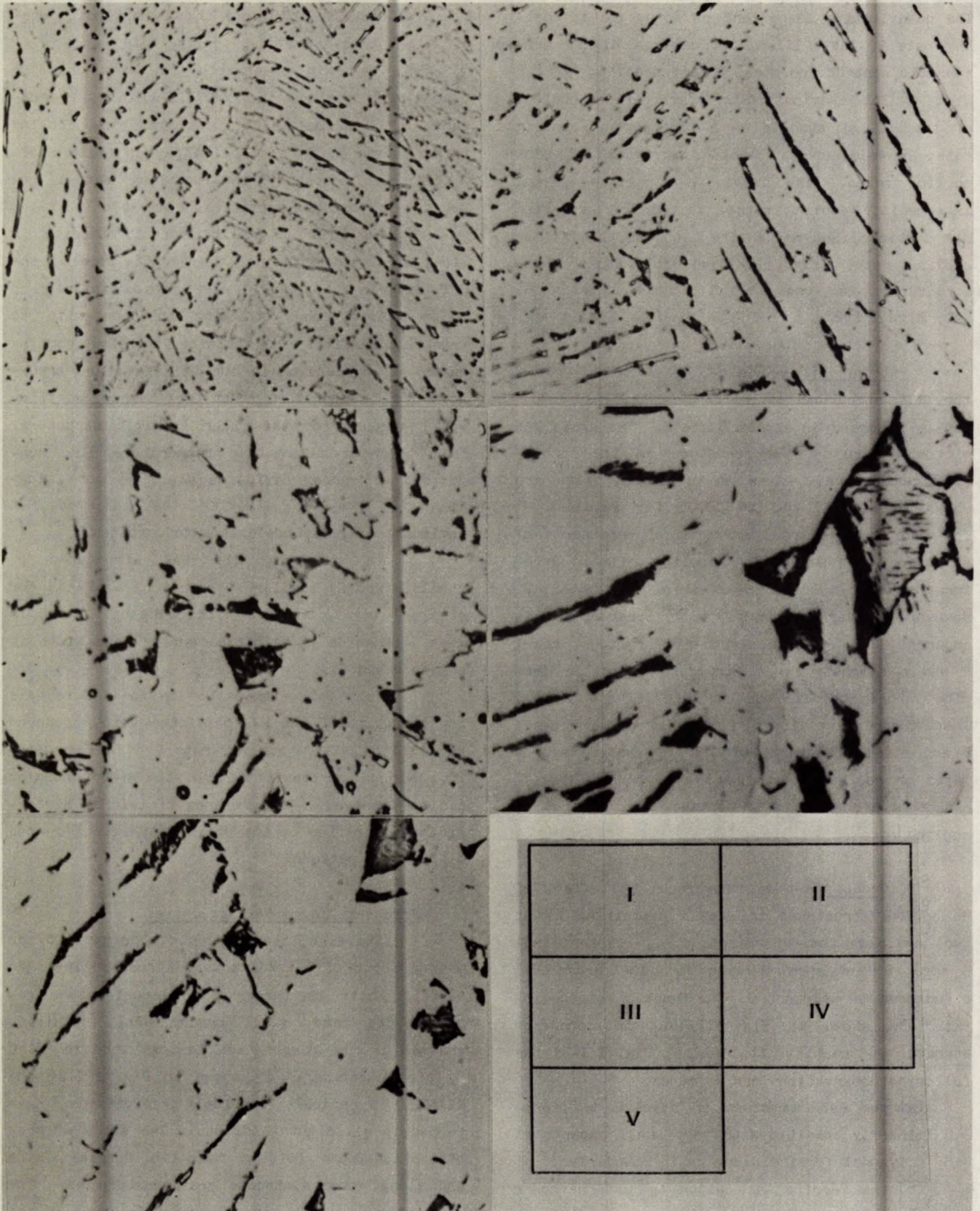


Fig. III-13 - Optical micrographs, steel E heat-affected-zone, cooling rates I-V, picral etch, x2000



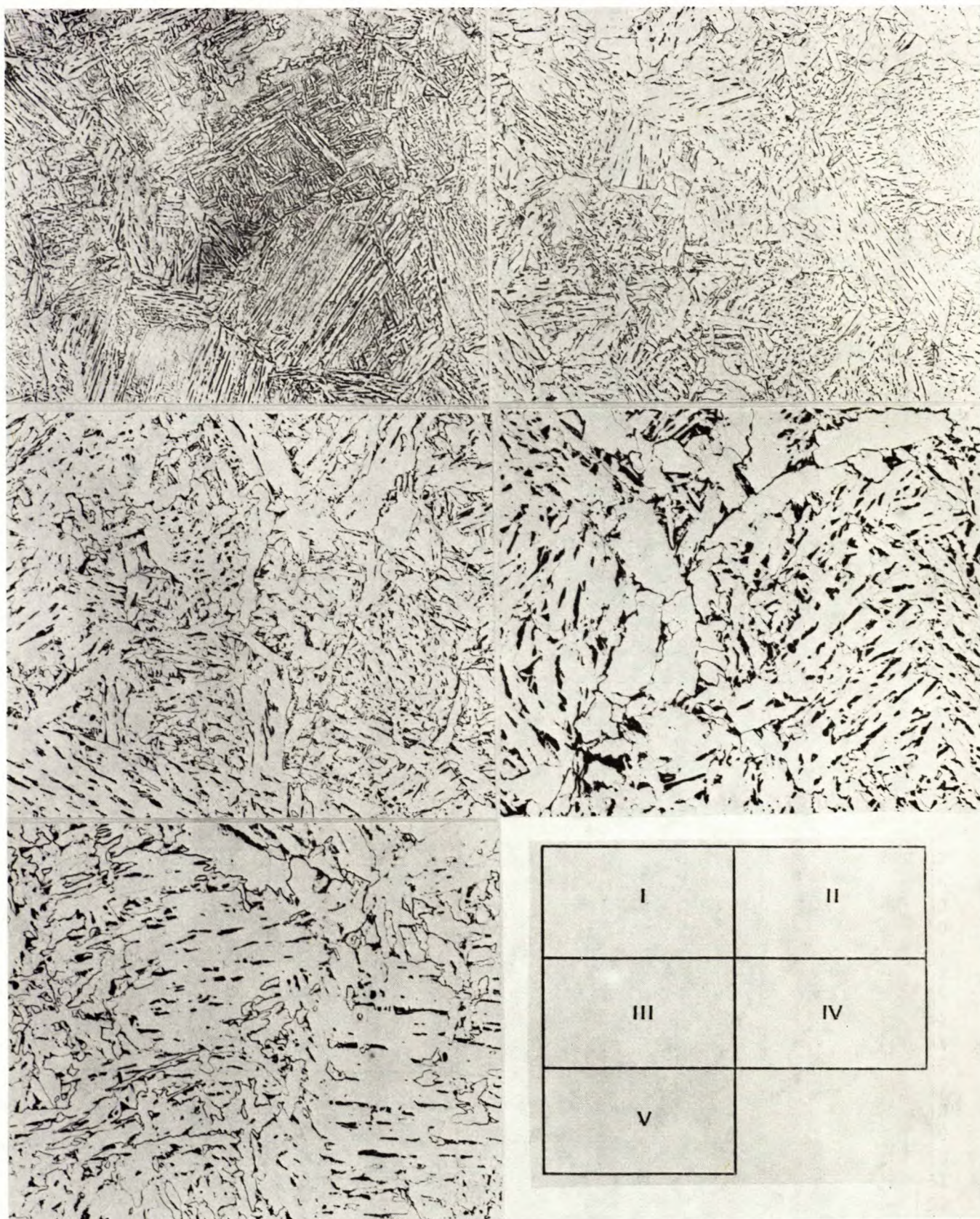


Fig. III-14 - Optical micrographs, steel F heat-affected-zone, cooling rates I-V, nital etch, x500



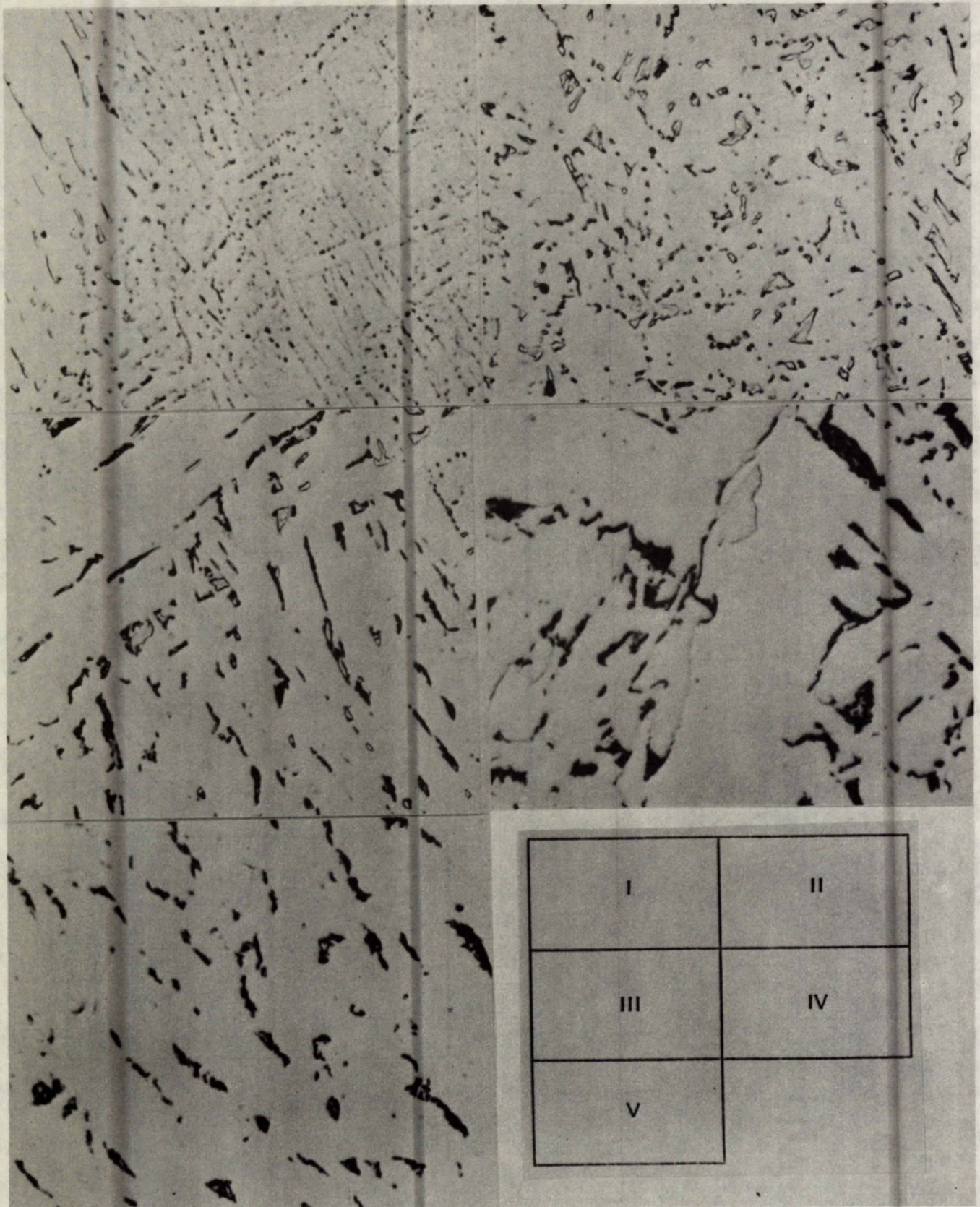


Fig. III-15 - Optical micrographs, steel F heat-affected-zone, cooling rates I-V, picral etch, x2000



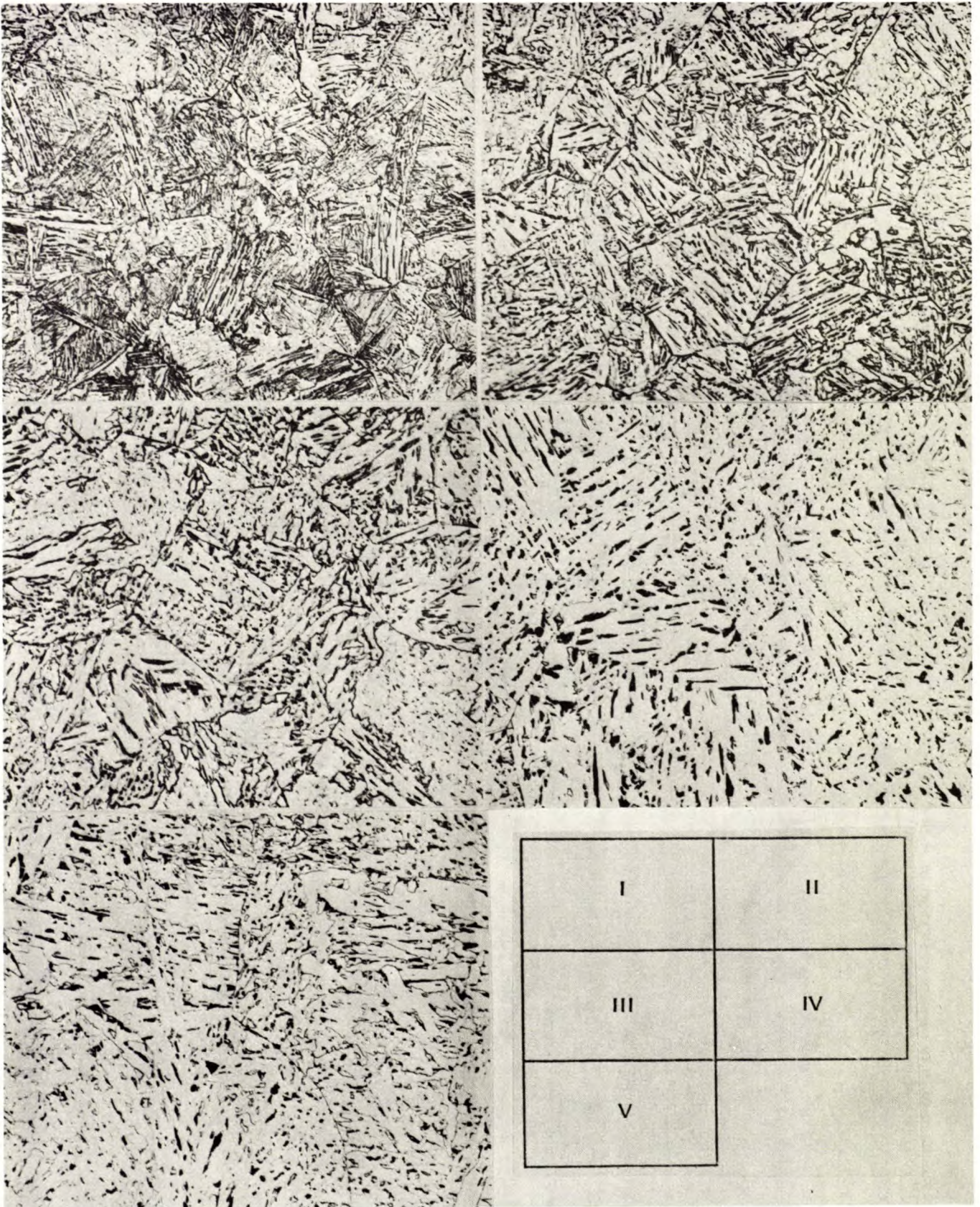


Fig. III-16 - Optical micrographs, steel G heat-affected-zone, cooling rates I-V, nital etch, x500



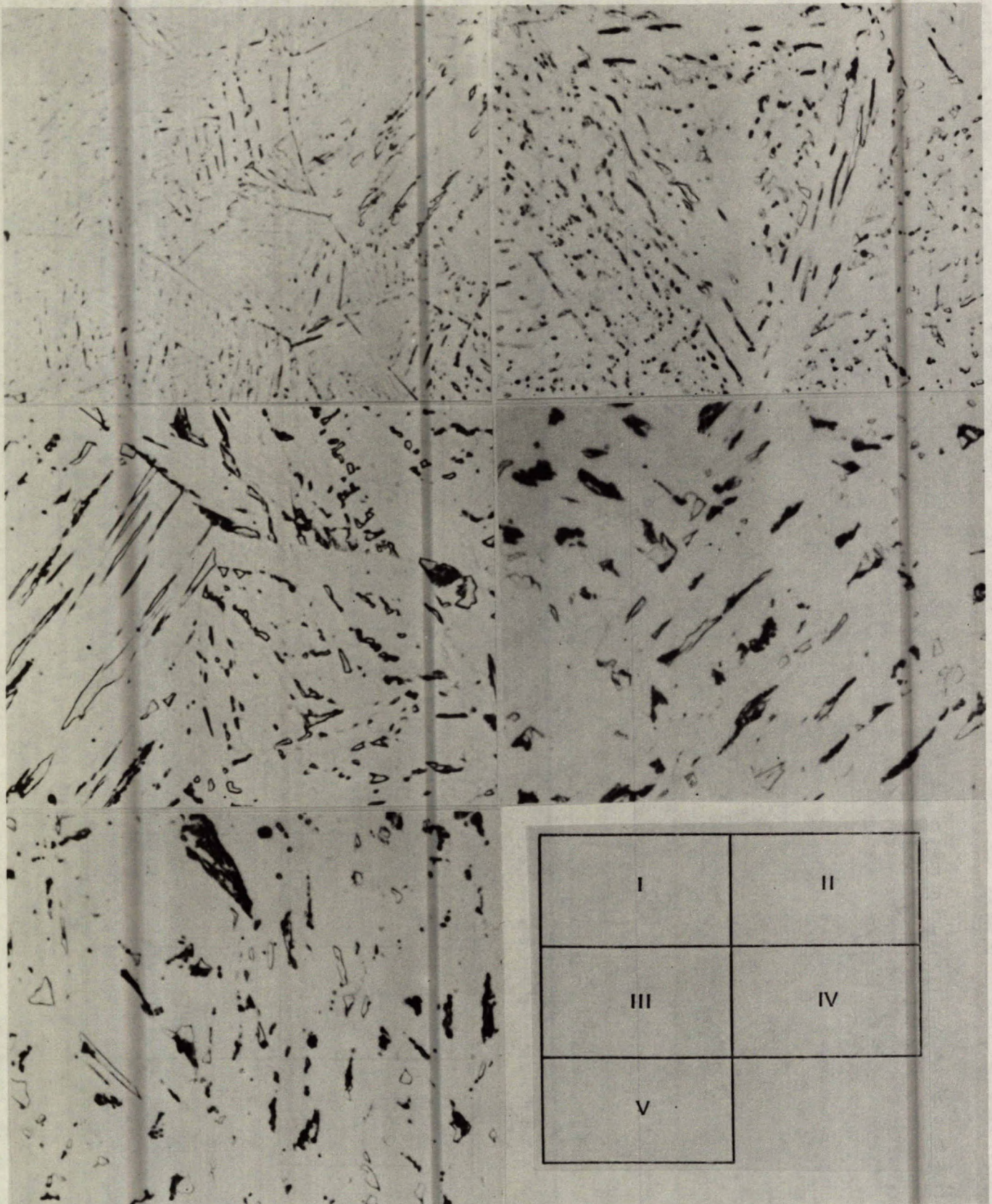


Fig. III-17 - Optical micrographs, steel G heat-affected-zone, cooling rates I-V, picral etch, x2000



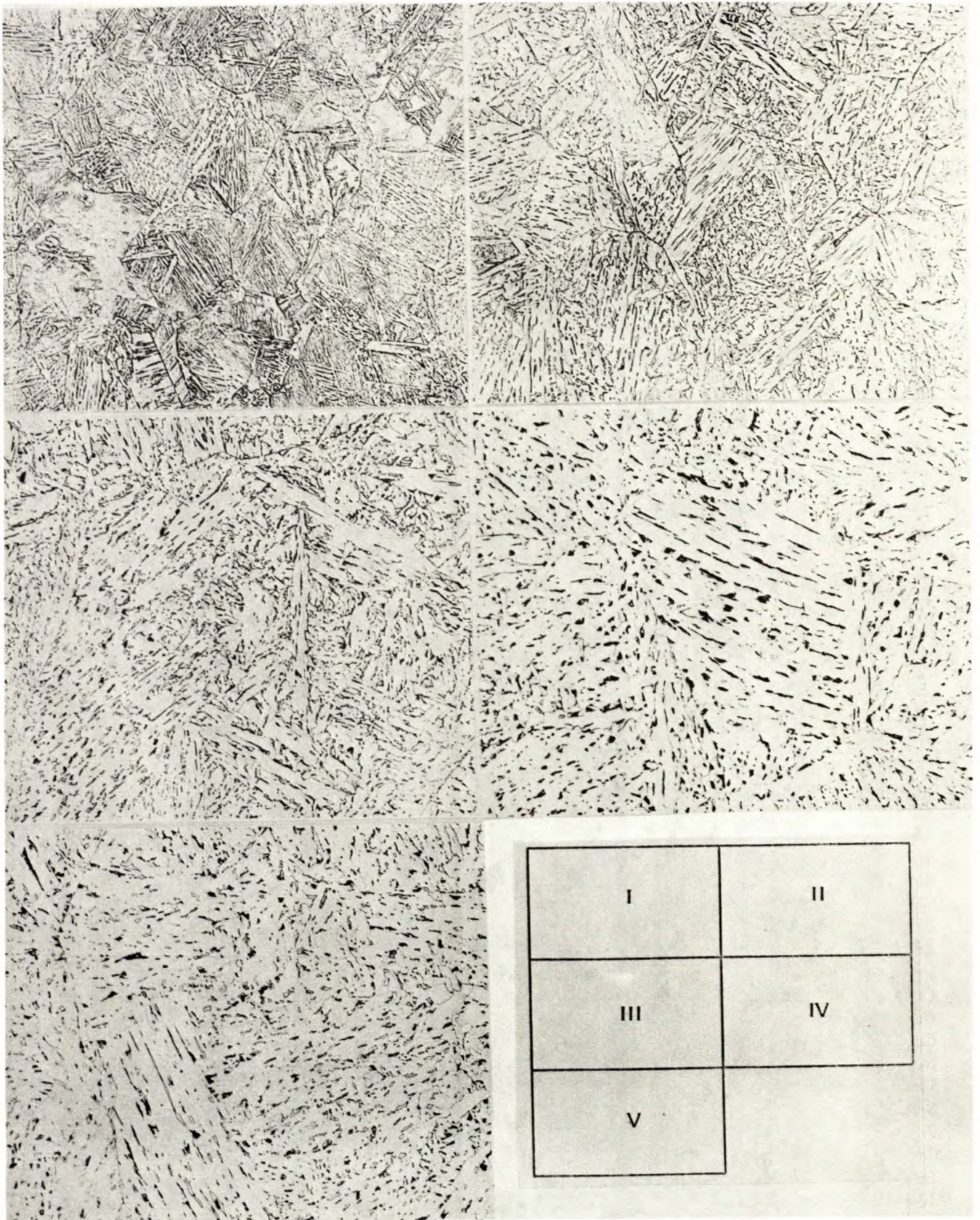


Fig. III-18 - Optical micrographs, steel H heat-affected-zone, cooling rates I-V, nital etch, x500



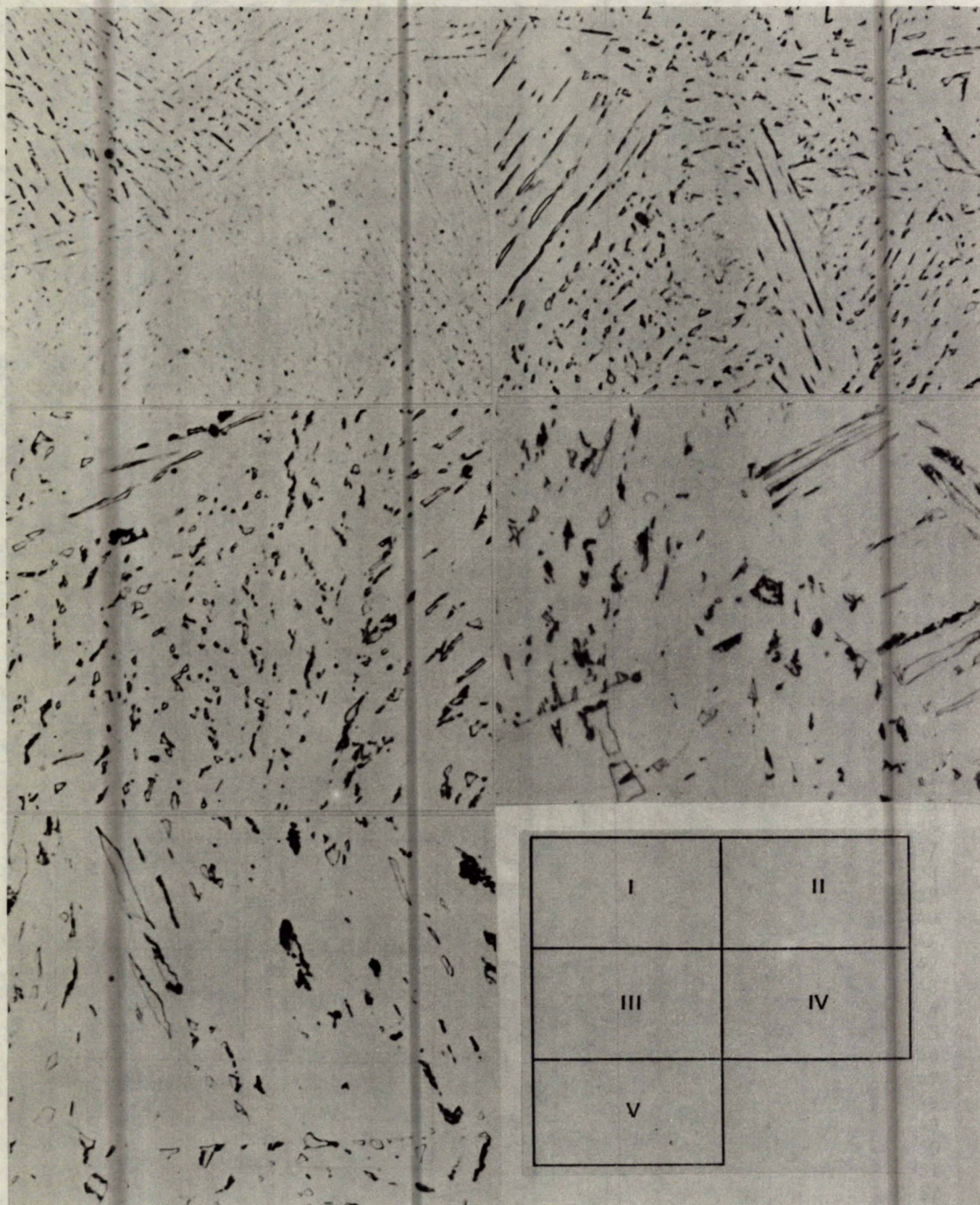


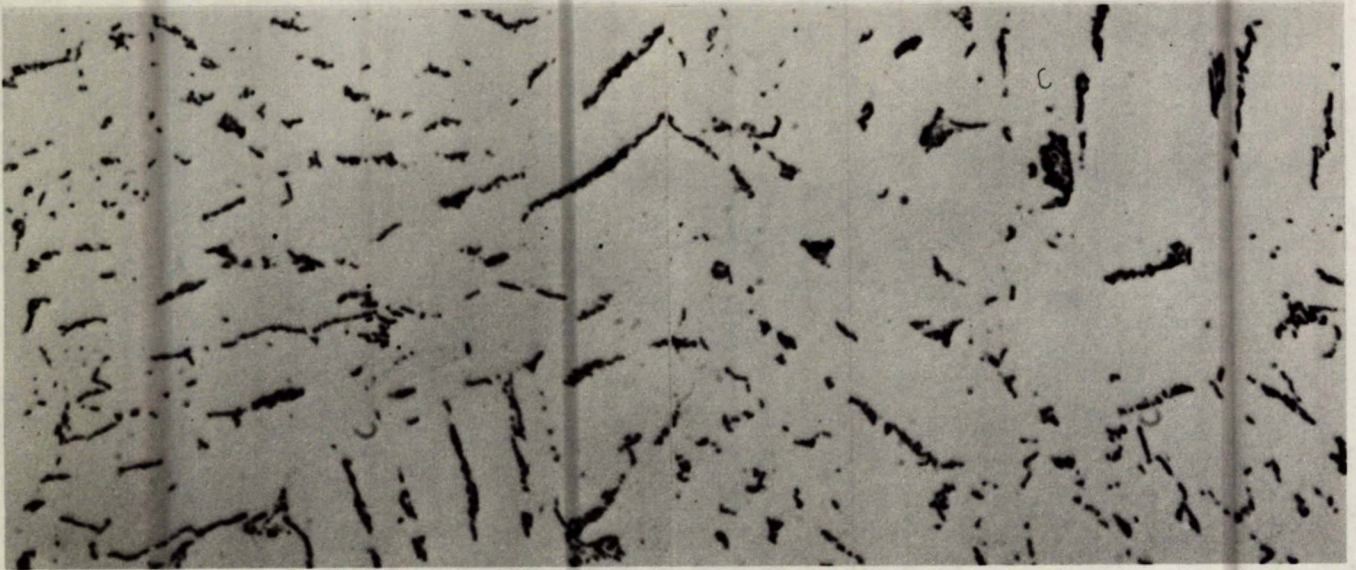
Fig. III-19 - Optical micrographs, steel H heat-affected-zone, cooling rates I-V, picral etch, x2000





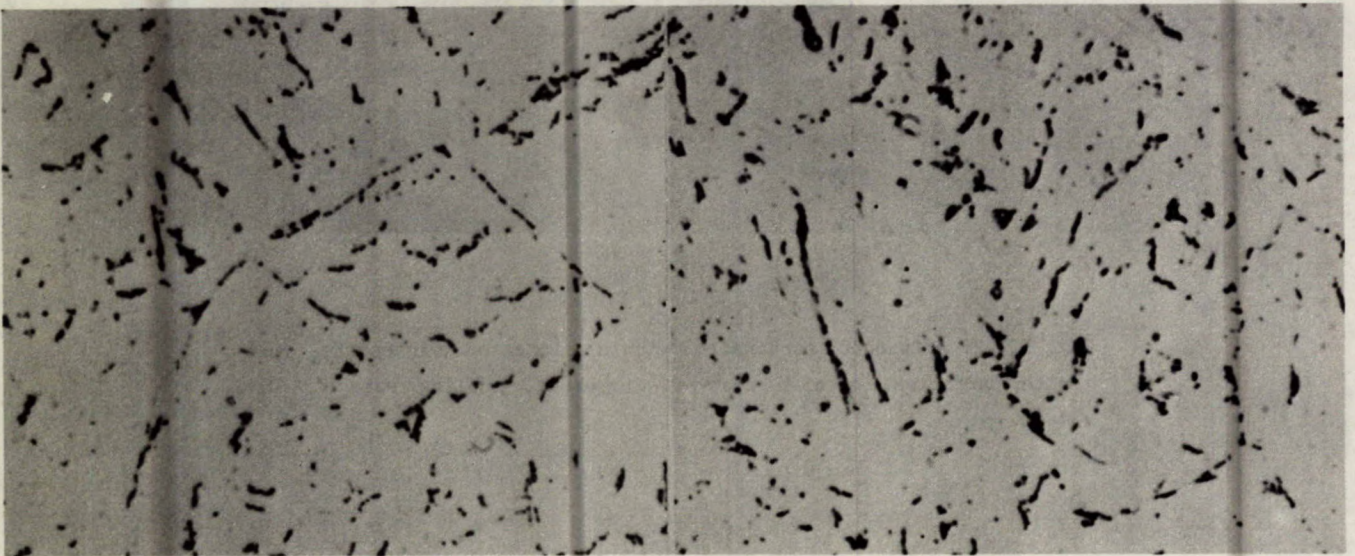
Fig. III-20 - Twinned martensite within elongated martensite- austenite particles, steel H heat-affected-zone, cooling rate V, TEM, x34 000





Steel 'A'

Steel 'B'

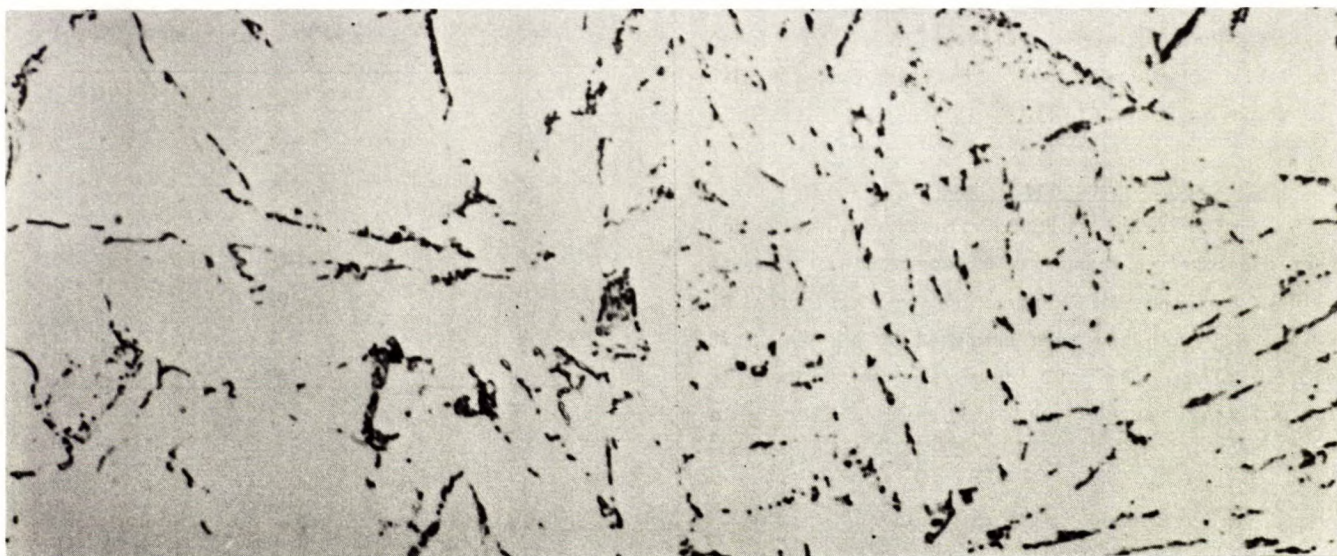


Steel 'C'

Steel 'D'

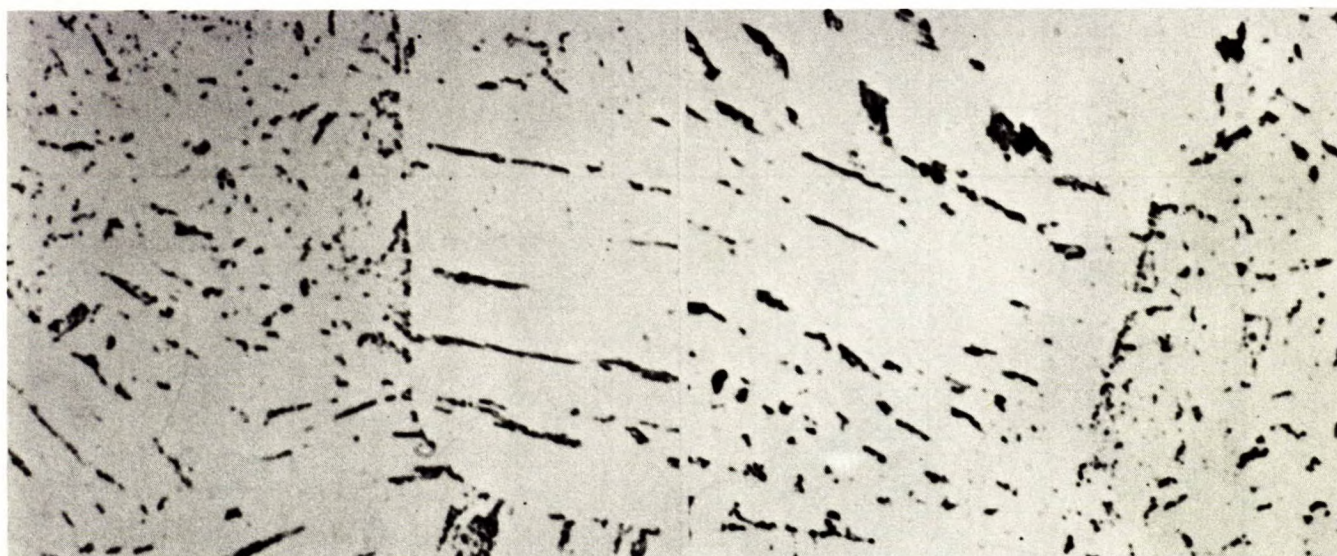
Fig. III-21 - Carbide precipitates in heat-affected-zone structure, stress-relieved at 620°C, optical micrographs, picral etch, x2000





Steel 'E'

Steel 'F'



Steel 'G'

Steel 'H'

Fig. III-22 - Carbide precipitates in heat-affected-zone structure, stress-relieved at 620°C, optical micrographs, picral etch, x2000



HAZ structures in the as-welded condition, have been replaced in every case by fine carbide precipitates.

The hardness of the coarse grain HAZ region for each stress-relieved steel is listed in Table III-5. Hardness traverses of the HAZ are shown in Fig. III-23.

#### COD fracture toughness data

The critical COD values,  $\delta_c$ , were determined over a range of temperatures down to  $-112^\circ\text{C}$  for the HAZ regions of weldments A, D, E, and H, which had been prepared at a heat input of 7.5 kJ/mm. The COD data are summarized in Table III-6. Those specimens which failed in a

Table III- 5 - Maximum HAZ hardness of stress-relieved welds

Steel	Maximum HAZ hardness $H_v(10)$
A	210
B	274
C	289
D	333
E	215
F	302
G	292
H	339

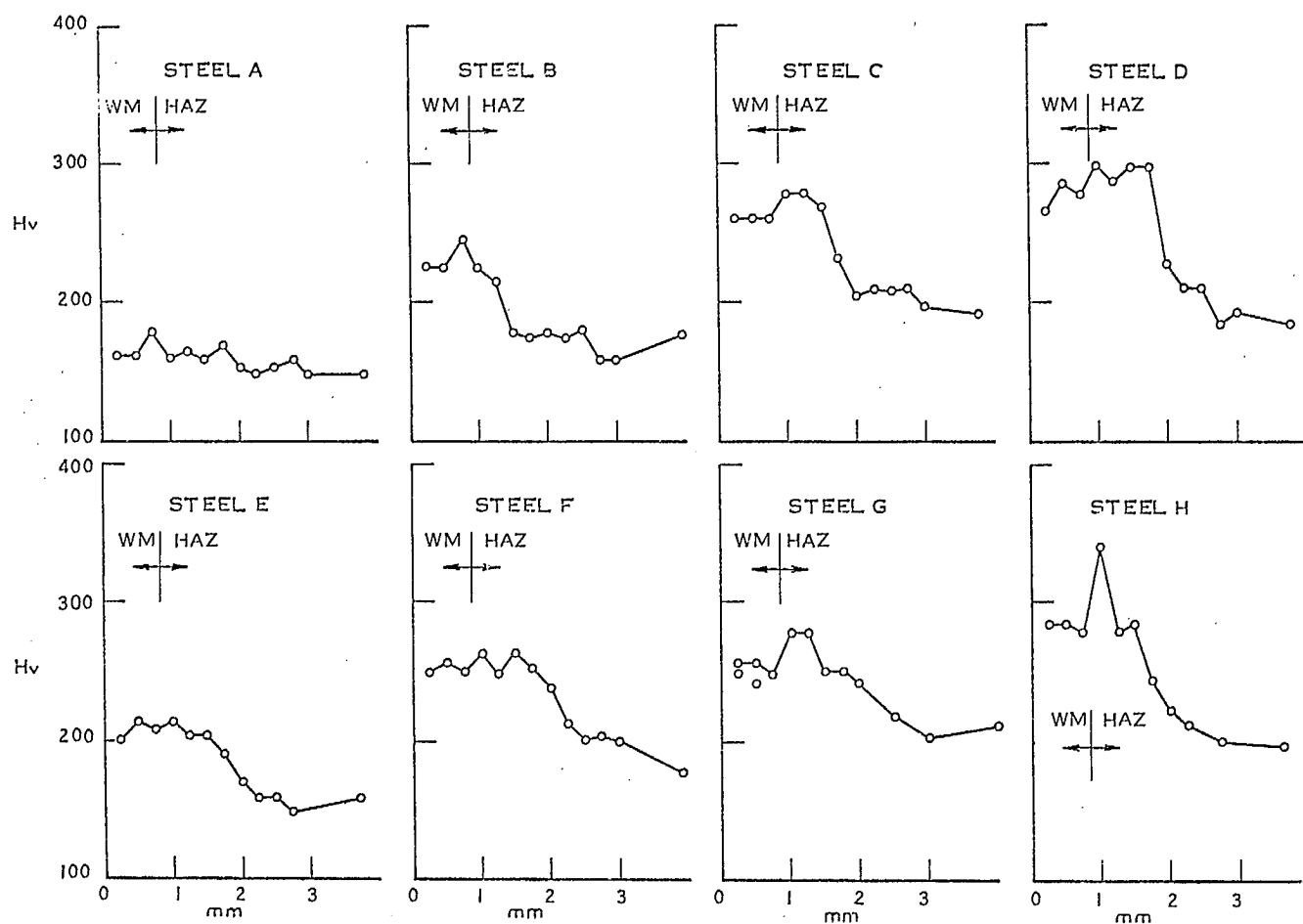


Fig. III-23 - Results of microhardness (200-g load) traverses on welds in steels A to H. Weld energy input was 2.4 kJ/mm, all welds stress-relieved at  $620^\circ\text{C}$  for one hour.



Table III-6 - COD results for  
heat-affected zone

Specimen*	Temperature	$\delta c$
	°C	mm
A150	22	1.42
	22	1.08
	0	1.34
	0	1.45
	-40	1.38
	-80	1.60
	-80	0.50
	-112	0.07
D150	22	1.30
	22	1.25
	0	1.08
	0	1.31
	-40	1.05
	-40	0.18
E150	22	1.31
	22	1.40
	-20	1.18
	-20	1.19
	-60	1.16
	-80	1.06
	-90	0.37
	-90	0.51
H150	22	1.33
	22	1.30
	10	1.19
	5	0.15
	- 5	0.07
	- 5	0.98
	-20	0.14
	-20	0.10

\*Weldments prepared at energy input of  
7.5 kJ/mm

drop in load. The temperature for the onset of cleavage failure is recorded for each weldment in Table III-7. Also recorded in Table III-7 is the yield load transition temperature as determined from the dynamic instrumented Charpy tests. The differential between the ductile-brittle transition temperature for slow bend and dynamic loading is of the order of 75 to 110°C and is in reasonable agreement with that found by other investigators in comparing toughness properties measured by slow and fast loading procedures (1).

#### Summary of results

The effects of cooling rate and composition on HAZ microstructures were the focus of a metallographic analysis. It was generally found for all steels that, as a function of increasing cooling rate, HAZ microstructures changed from mixtures of coarse bainite and polygonal ferrite at grain boundaries for the slowest cooling conditions, through fine bainite, to bainite-martensite mixes at the fastest cooling conditions. The prior austenite grain size was reduced as the cooling rate increased with lower heat inputs. Increasing the cooling rate also resulted in a change from coarse carbide aggregates between ferrite laths to M-A particles.

For Group I weldments, the effect of increasing niobium content was to reduce the width of the bainitic ferrite laths and the size of the carbide aggregates, particularly at the slow cooling rates. Prior austenite grain size was insensitive to niobium addition.

Table III-7 - Ductile/brittle  
transition temperature

Steel	Transition temperature, °C	
	COD	Instrumented Charpy
A	-80	27
D	-40	42
E	-90	20
H	5	68

ductile manner had a load/displacement curve in which the load dropped gradually after achieving a maximum. With the transition to cleavage failure, the load/displacement curve exhibited limited non-linear behaviour prior to an abrupt



Vanadium, Group II and Group III, has no significant effect on the gross HAZ structure in both niobium free and niobium containing steels at cooling rates slower than rate I. For cooling rate I, the vanadium bearing steels had a higher martensite content in the HAZ.

In Group IV, niobium containing steels, the addition of molybdenum decreases the amount of grain boundary polygonal ferrite, refines the bainitic structure, promotes the formation of M-A particles at the slowest cooling rates IV and V, and increases the martensite content at cooling rate I.

The stress relieving treatment at 620°C modifies the carbon rich regions by precipitating fine spherical carbide particles along ferrite lath boundaries and prior austenite boundaries in a predominantly bainitic HAZ structure. M-A particles were replaced by fine carbides.

The results of the COD test program indicate a differential in ductile-brittle transition temperature between slow bending and dynamic loading of the order of 75 to 110°C for the four steel HAZ structures investigated.

#### Acknowledgements

The comments of B.A. Graville on the interpretation of results are appreciated. The technical assistance of I.D. Montgomery in all phases of the metallographic investigation is gratefully acknowledged.

#### References

1. Rolfe, S.T. and Barsom, J.M. "Fracture and fatigue control in structures; applications of fracture mechanics"; Prentice-Hall; 1977.



PART III - SECTION 'B'  
PRECIPITATION EFFECTS

by

G.C. Weatherly\*

### Introduction

In Parts I, II and IIIA, instrumented impact tests, continuous cooling transformation characteristics, and microstructures of a series of microalloy steels have been dealt with. This work has shown that a significant deterioration of fracture toughness as measured by the instrumented impact test occurs at high niobium levels for the highest heat input welds, whereas vanadium has very limited effects. The deleterious effects of niobium are even more marked in the stress-relieved condition, whereas again, vanadium on its own, has little influence.

The role that niobium plays in microalloy steel welds is poorly understood, although there is general agreement that for high heat input welds and at high niobium levels, a deterioration in toughness occurs. Theories proposed to explain this can be broadly grouped into two categories:

- (i) precipitation effects and
- (ii) modification of the austenite-ferrite transformation characteristics.

The principal proponent of the former theory is Hannerz, who in a series of publications proposed that microalloy precipitation of Nb (C,N) or VN is responsible for the high hardness and poor toughness of the weld metal or HAZ (1) (2) (3).

As the direct evidence for microalloy precipitation is unconvincing, a number of other authors have suggested instead that the role of niobium is to promote the formation of a coarse lath ferrite structure which has poor toughness (4) (5) (6). Evidence for this was presented by

Levine and Hill, but again before this result can be accepted, the statistical significance of the observation must be evaluated (6). The importance of statistics in this type of work was emphasized in a recent study of Pacey and Kerr, where they showed large variations in the microstructure of a single weld in neighbouring cross sections (7).

The role of niobium in modifying the microstructure of the HAZ was assessed in Parts II and IIIA. In this part, evidence for microalloying precipitation will be presented. The single most important factor in this work is selection and development of a reliable technique for detecting fine precipitation of less than 5  $\mu\text{m}$  in size. Hannerz and colleagues used transmission electron microscopy of thin foils prepared from the weld and heat affected zone (1) (2) (3). They were able to show precipitation in the stress-relieved condition, but concluded that any precipitates formed in the as-welded condition were below the resolution limit of the electron microscope. As the resolution limit of most modern electron microscopes is below 5 $\text{\AA}$ , they presumably mean that in a typical thin foil, the available contrast mechanisms for seeing fine particles, via strain field or structure factor differences, do not permit observation of very fine particles (8). This inherent limitation of thin foil studies is exacerbated in the present case by the high dislocation density and high internal stresses of a weld which lead to buckling of the foil. In the early stages of this investigation, thin foil samples were prepared but the results were inconclusive.

---

\*Dept. of Metallurgy & Material Sciences,  
Toronto, Canada.



For these reasons, the technique of carbon extraction replication was used. The major advantage of this technique is that the extracted crystalline particles sit on a thin amorphous carbon film, and particles as small as  $20\text{\AA}$  can be detected. In addition, diffraction patterns of the precipitates are readily obtained. The disadvantage of carbon extraction replicas lies in the uncertainty of the efficiency of the replication process, particularly for very small particles, and the difficulty of taking a replica from a very narrow HAZ which may be only 200-300  $\mu\text{m}$  wide.

#### Experimental procedure

Carbon extraction replicas were prepared by standard techniques. The weld, HAZ, and parent plate regions, were polished with fine alumina and etched with 2% nital. In preliminary experiments the etching time was varied from 1 s to 30 s to test the efficiency of the replication process. Increased etching times lead to pick-up of a greater volume fraction of fine precipitates, Fig. III-24. This is useful for identification of the crystal structure of the precipitates, but gives an unrealistically high value for the volume fraction of the precipitation and leads to "clumping" of precipitates in the replica, an artifact of replication. Despite these drawbacks, a fairly long etching time of  $\sim 10$  s was used in the rest of the work. Although Gray et al comment that a very light etch is required to extract very fine NbC (9), it was found that particles down to  $20\text{\AA}$  in size could be extracted this way. After etching, a thin film of carbon  $\sim 300\text{--}400\text{\AA}$  thick, was deposited on the surface in a vacuum evaporator. After carbon deposition, all regions of the surface except the area of interest were protected by microstop, with the remaining exposed part of the replica being cut into suitable rectangular shapes. The carbon films were then floated off by electropolishing the underlying metal and were then collected and washed in alcohol and alcohol-water solutions. The samples studied are listed in Table III-8.

#### Results

The reliability and efficiency of the extraction process alluded to above is indicated in Fig. III-24. The base plates all contained a distribution of both coarse and very fine NbC clearly shown by dark field electron microscopy in Fig. III-25a. This bimodal size distribution presumably results from the processing of the steel plate, with precipitation both in the austenite and ferrite giving a range of precipitate sizes. This distribution in steel D should be compared with that for the HAZ of sample D 112 in Fig. III-25b which shows a distribution of very fine particles only, i.e.,  $\sim 50\text{\AA}$  in size. No large NbC particles are visible in this area or in adjacent areas of the same replica, convincing evidence that all the NbC had gone into solution during this thermal cycle and had reprecipitated on cooling. This conclusion is reinforced by observations of coarser NbC particles in some of the lower heat input welds which apparently spent insufficient time at the highest temperatures to allow complete dissolution.

With the exception of sample A, which had no microalloy constituents, precipitation was found in all of the samples studied for the highest heat inputs ( $\Delta t_{800-500^\circ\text{C}} = 160$  s). The effect of increasing niobium content is shown in Fig. III-26 for steels A-D. There appears to be a slight decrease in average NbC particle size

Table III-8 - Samples examined for  
microalloy precipitation

---

CODE 150*	- A, B, C, D, E, G, H
CODE 112*	- C, D, H
CODE 60*	- C, D, G
N - D - III	(from dilatometry studies)
D 60T, H60T	(stress relieved samples)
CODE 150	7.5 kJ/mm ( $\Delta t_{800-500^\circ\text{C}} = 160$ s)
CODE 112	4.4 kJ/mm ( $\Delta t_{800-500^\circ\text{C}} = 80$ s)
CODE 60	2.4 kJ/mm ( $\Delta t_{800-500^\circ\text{C}} = 39$ s)

---



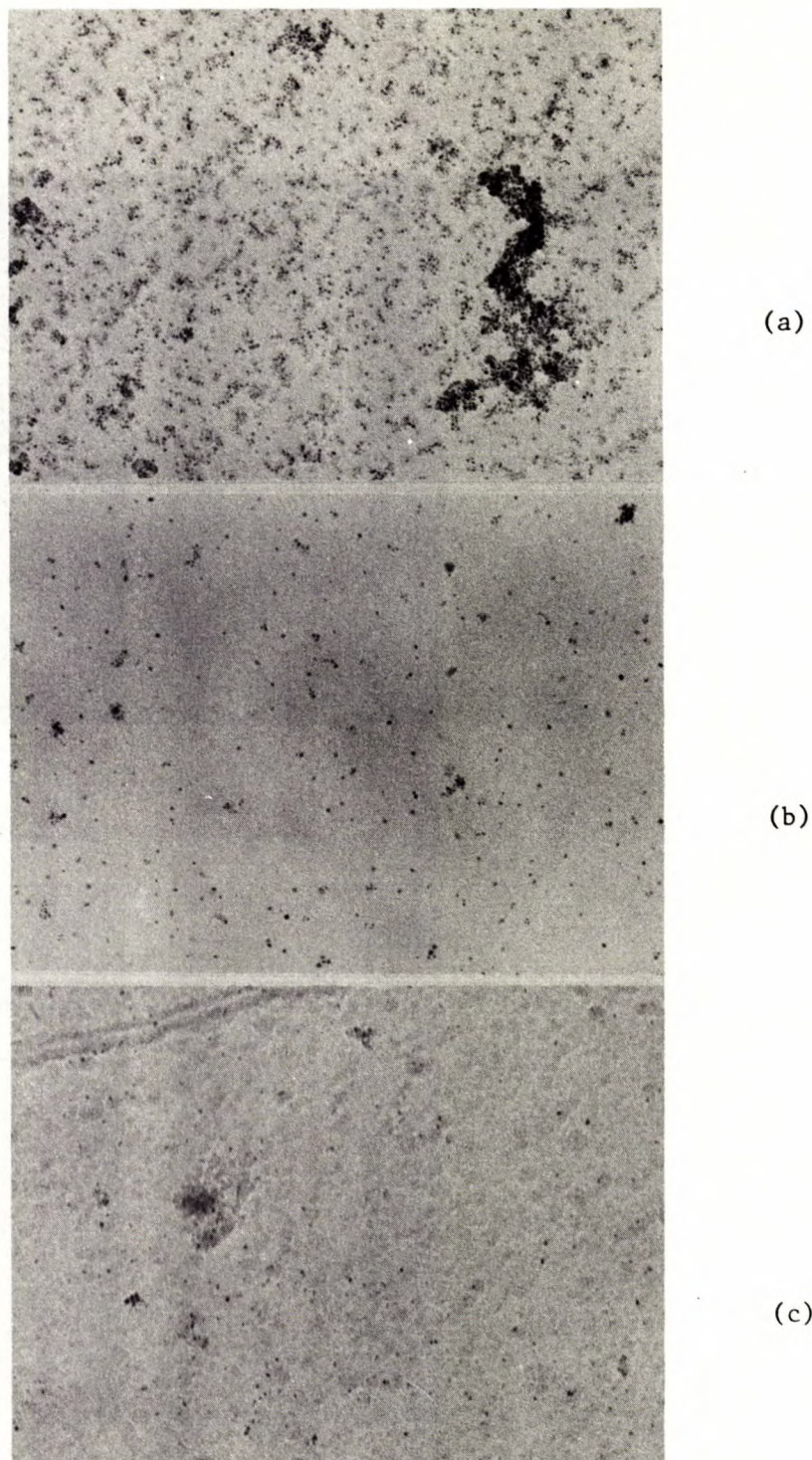


Fig. III-24 - Illustrating the effect of increasing etching time on the extraction of fine NbC particles - base plate D (x55 500)

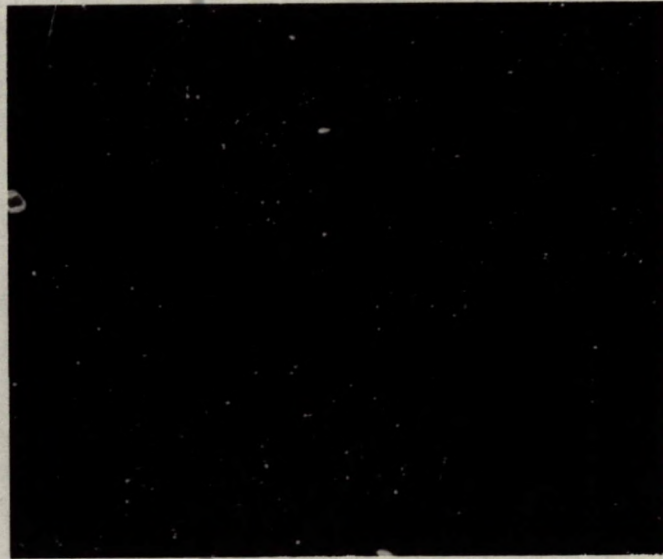
(a) Etching time = 30 s, Vol Fraction NbC = 8.5%

(b) Etching time = 5 s, Vol fraction NbC = 2.2%

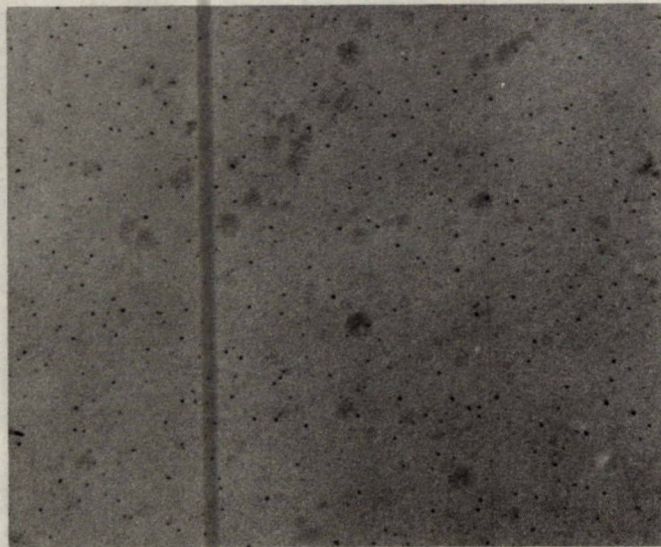
(c) Etching time = 1 s, Vol fraction NbC = 1.2%

These figures should be compared with a calculated volume fraction of 0.12%.





(a)



(b)

Fig. III-25 - Comparing the size and distribution of NbC particles in:  
(a) the base plate, dark field micrograph  $g = (111)$ ; and  
(b) the coarse grained HAZ. (NbC Sample D 112), (x55 500).



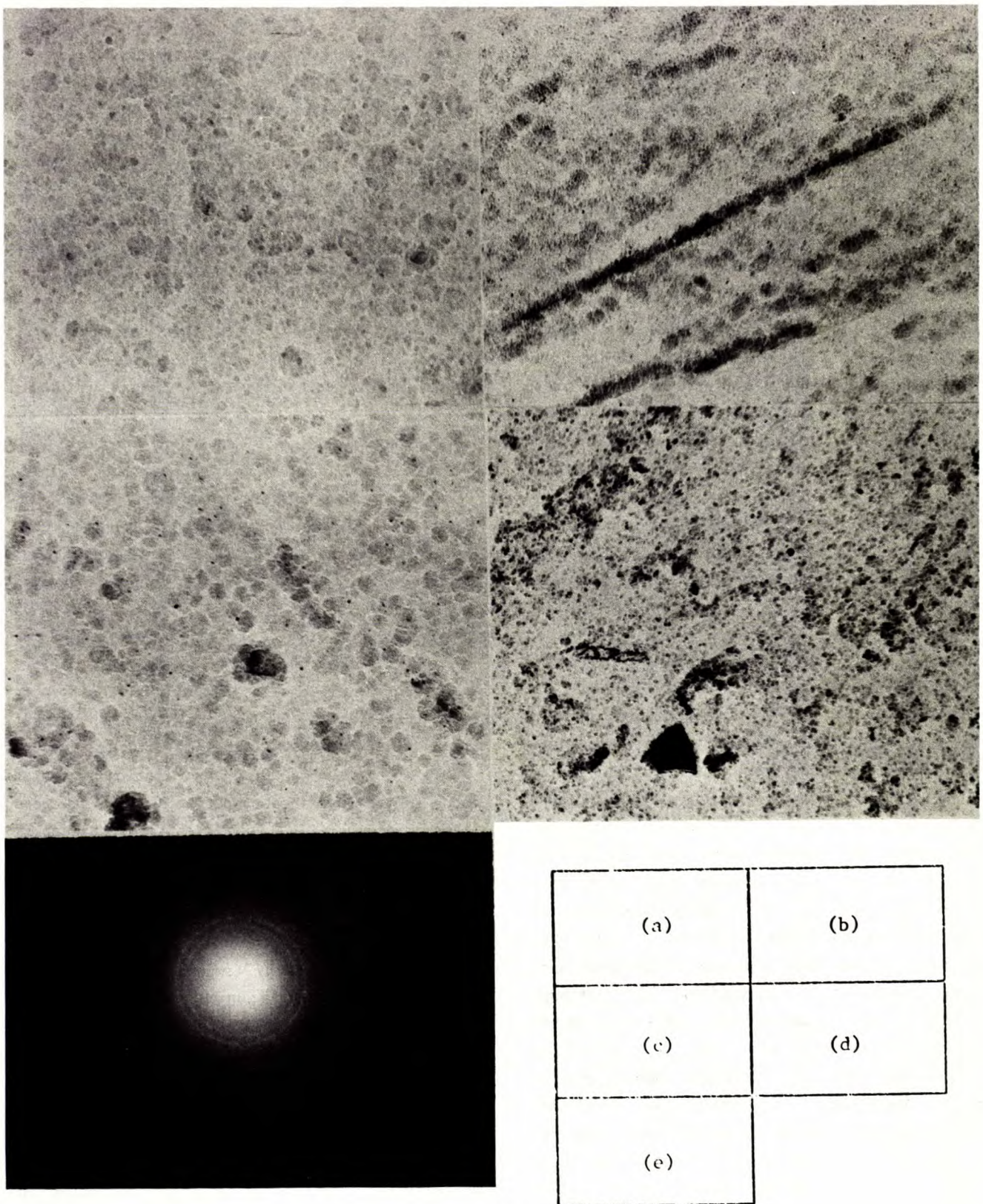


Fig. III-26 - Fine distribution of NbC particles in samples B150 (Fig. 26b), C150 (Fig. 26c) and D150 (Fig. 26d). Note the absence of particles in A150 (Fig. 26a). The identification of these particles as NbC is confirmed by the electron diffraction pattern for D150 (Fig. 26e), (x55 500).



as the niobium content varies from 0.14% to 0.034%. Sample E 150, containing 0.09% vanadium, had extremely fine particles with a maximum size  $\approx 40\text{\AA}$  which are just visible in Fig. III-27. These presumably are V (C, N), although no diffraction patterns could be obtained from them as were obtained for the NbC particles, Fig. III-26e.

For the second highest heat input welds, ( $\Delta t_{800-500^\circ\text{C}} = 80\text{ s}$ ) only samples C, D, and H were examined. All showed examples of fine precipitation as in Fig. III-28, the precipitates being comparable in size with those of Fig. III-26. Although there were some problems with these specimens in locating the coarsest grain structure of the HAZ, this could be done by examining the replica at the lowest possible magnification, i.e.,  $\sim 1500\times$  and comparing the replica structure with that seen in the optical microscope.

The problem of locating the replica with respect to the HAZ becomes even more acute for the lower heat input welds. Samples C60, D60 and G60 were all examined, but the only evidence of precipitation was the relatively coarse NbC particles seen in Fig. III-29 for samples C60 and D60. The particle size and distribution are more characteristic of those found in the base plate than those expected from precipitation during cooling, Fig. III-25a. Thus, it is concluded that these are the result of incomplete dissolution during the thermal cycle associated with welding. As the coarse grained HAZ is very narrow in these samples, it is not certain that the particular examples shown in Fig. III-29 have come from regions that experienced the peak austenitic temperature ( $\sim 1350^\circ\text{C}$ ). An attempt was made to see whether precipitation is possible at this cooling rate ( $\Delta t_{800-500^\circ\text{C}} = 39\text{ s}$ ) by examining the highest niobium sample used in the dilatometry work to establish the transformation characteristics of the steel as a function of cooling rate. The whole midsection of these samples was raised to  $1320^\circ\text{C}$  in 10 s and cooled to give a cooling rate comparable to that of Code 60, Table III-8. As pointed out in Part II of this report, this time of 10 s is slightly longer

than that experienced during welding, and may be sufficient to take all the NbC particles into solution. An extremely fine distribution of particles identified as NbC was found in these samples and, in agreement with this hypothesis, no coarse particles of NbC, Fig. III-30a.

The final part of this study was an evaluation of precipitation in the stress-relieved samples D60T and H60T. These again are difficult to examine because of the very narrow HAZ. The experiment would have been more successful on thermally simulated samples. Precipitation was observed in both samples but varied tremendously in density from one area to the next. The effect, which could be corroborated by thin film studies may be genuine, but it could also be an artifact of replication. Precipitation was apparently enhanced at ferrite boundaries as shown in Fig. III-31b. Electron diffraction again identified this precipitate as NbC.

#### Discussion

The most gratifying aspect of this work was the clear evidence of dissolution followed by reprecipitation of NbC in the two highest heat input welds, and the evidence of V (C,N) precipitation in sample E 150. Precipitation may also occur in the lower heat input welds, but it seems likely that there is insufficient time at temperatures  $> 1000^\circ\text{C}$  when NbC may be expected to go into solution to dissolve all the NbC.

The thermodynamic driving force for precipitation depends on the total Nb, C and N content in solution at any temperature, but kinetic factors must also play an important role. For example, for steel D, the austenite to ferrite transformation start temperature only drops from  $740^\circ\text{C}$  to  $700^\circ\text{C}$  as the cooling time from  $800-500^\circ\text{C}$  decreases from 80 s to 39 s; but at a cooling rate of 16 s drops drastically to  $580^\circ\text{C}$ . As NbC precipitation is always sluggish in austenite, and as the rate is very slow in ferrite at temperatures below  $600^\circ\text{C}$ , no precipitation would be expected for the lowest heat input welds. However, for a cooling time of



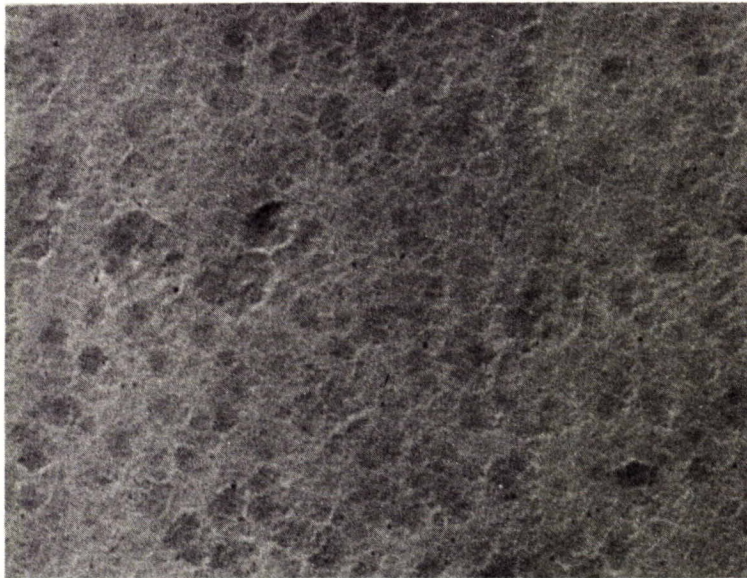
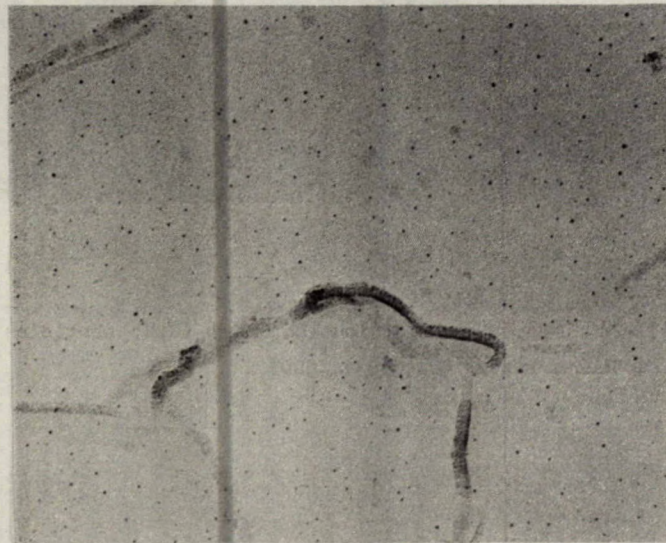


Fig. III-27 - Very fine distribution of V (C,N) particles in sample E150; particles size  $\sim 40\text{\AA}$ , (x111 000)





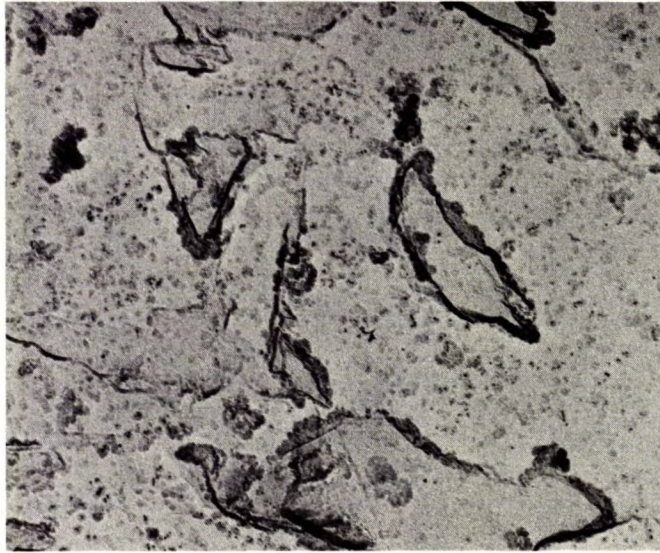
(a)



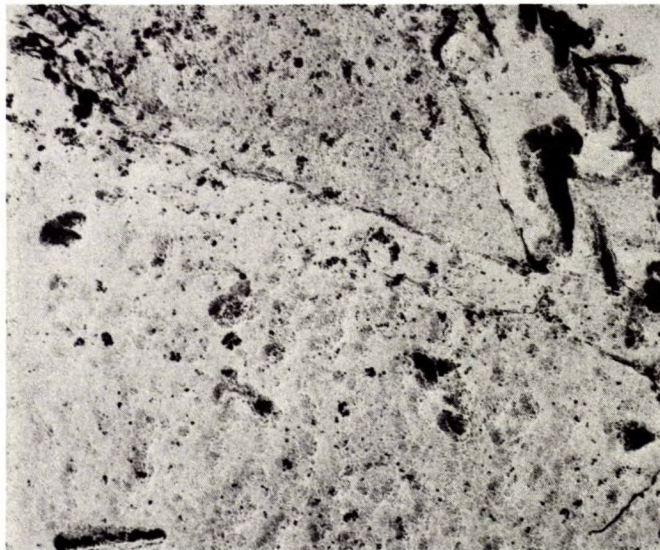
(b)

Fig. III-28 - Comparison of low magnification and high magnification shots of same area of sample C112 showing coarse grained HAZ (with carbides) in Fig. 28(a) (x8000) and fine NbC particles at high magnification in Fig. 28(b), (x55 500)





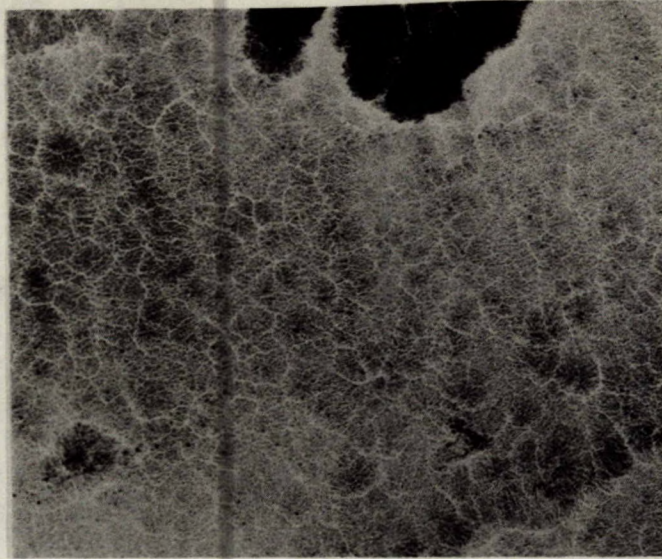
(a)



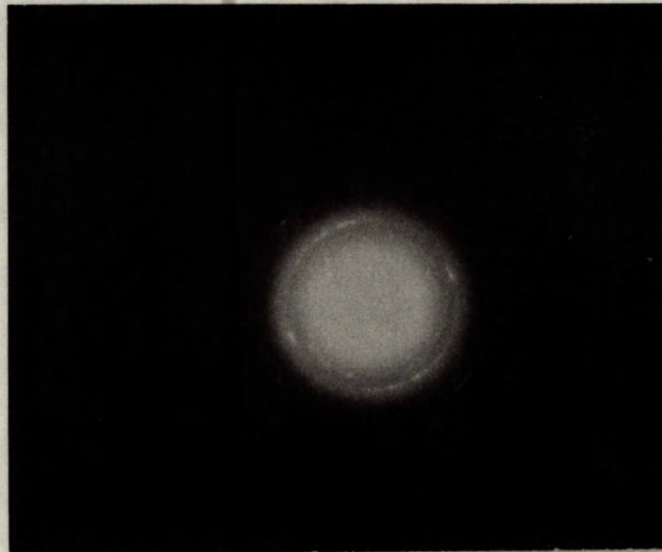
(b)

Fig. III-29 - Distribution of coarse and fine NbC particles in samples C60 (Fig. 29a) and D60 (Fig. 29b); this distribution is probably the result of incomplete dissolution during the weld thermal cycle, (x21 500)





(a)



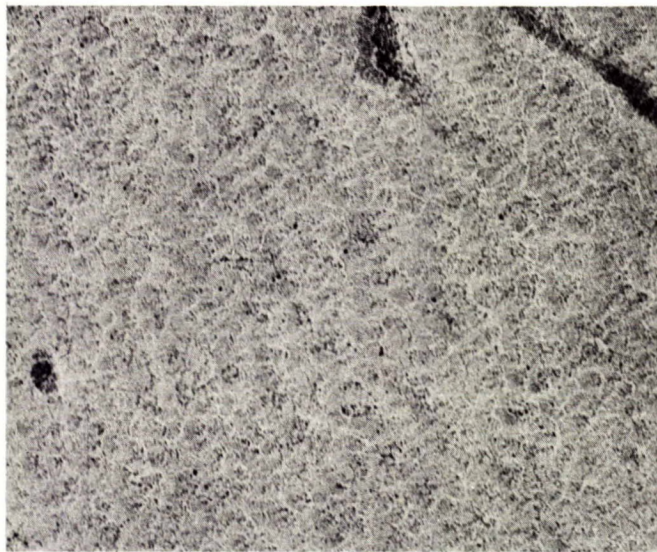
(b)

Fig. III-30 - Fine distribution of NbC in sample N-D III (thermally simulated); sufficient time was spent at peak temperature to allow all NbC to go into solution and reprecipitate at this cooling rate ( $\Delta t_{800-500^\circ\text{C}} = 39 \text{ s}$ ); (a)  $\times 55\,500$  and (b) diffraction pattern confirming NbC structure for the fine precipitates.





(a)



(b)

Fig. III-31 - Distribution of NbC in stress-relieved samples; (a) D 60T, dark field micrograph and (b) H 60T; the dark field micrograph shows the effect of clustering of the particles at ferrite boundaries, (x55 500).



39 s, NbC should be at the threshold of precipitating if there is sufficient time for it to dissolve in the parent plate. The results of the present study do not allow a definite conclusion to be reached on this point.

The influence of precipitation on the strength and toughness of the HAZ will be discussed in Part IV, but it is worth re-emphasizing that the present studies indicate only the occurrence or absence of fine precipitates. Unfortunately, replicas provide no good information on the volume fraction of precipitates which determine the hardening increment expected from a given particle size distribution. Even for the highest heat input welds on niobium bearing steels, it is unlikely that all the available niobium will have precipitated as the 50% transformation temperatures are all 600°C or lower.

#### Acknowledgement

This work was done in conjunction with G. Shek and F. Neub, whose valuable contributions are gratefully acknowledged.

#### References

1. Hannerz, N.E. "Weld metal and HAZ toughness and hydrogen cracking susceptibility of HSLA steels"; Rome Conference on Welding of HSLA Structural Steels; Nov. 1976.
2. Hannerz, N.E. and Jonsson-Holmquist, B.M. "Influence of vanadium on the heat-affected-zone properties of mild steel"; Metal Sci J, 8:228-234; 1974.
3. Hannerz, N.E. "Effect of Cb on HAZ ductility in constructional H.T. Steels"; Weld J; 1625-1685; 1975.
4. Jesseman, R.J. Proceedings Microalloy 75; Union Carbide Corp.; 566; 1977.
5. Levine, E. and Hill, D.C. Metal Construction; 9:346; 1977.
6. Levine, E. and Hill, D.C. Mt Trans, 8A: 1453; 1977.
7. Pacey, A.J. and Kerr, H.W. Dept of Mechanical Eng, University of Waterloo; Submitted to Welding Journal.
8. Ashby, M.F. and Brown, L.M. Phil Mag, 8: 1649; 1963.
9. Gray, J.M., Webster, D. and Woodhead, J.H. J Iron and Steel Inst; 203:812; 1965.



## PART IV: GENERAL DISCUSSION

A.G. Glover\*, B.A. Graville\*, J.T. McGrath\*,

A.B. Rothwell\*\* and G.C. Weatherly\*\*\*

Introduction

Previous sections of this report have dealt with the results of instrumented Charpy impact tests, Part I, a dilatometric investigation of transformation characteristics, Part II, and a detailed metallographic examination, Part III, on the heat-affected zones of welds in eight experimental steels. The purpose of this final section is to relate the observed variations in toughness to transformation behaviour and microstructure; in particular, the evidence pertaining to the role of microalloy carbide or carbo-nitride precipitations will be examined in some detail as this point remains controversial (1). The significance of the dilatometric results will first be considered. Variations of weld HAZ hardness and toughness, and the effect of stress relief heat-treatment will then be discussed together with relevant microstructural observations.

DiscussionDilatometry

Before considering the significance of the dilatometric results, it is necessary to show that the technique allows a sufficiently close reproduction of HAZ microstructures at equivalent cooling rates if valid conclusions are to be drawn. There are a number of factors it is not possible to take into account when attempting to determine the transformation characteristics of weld HAZs using conventional dilatometers. Firstly, the limited programming capabilities of such instruments will not reproduce an exact simulation of weld thermal cycles. Typically, natural or forced gas-cooling is used to produce fast cooling rates, whereas linear cooling is the only option available at slower cooling rates. Neither of these cooling modes exactly match the

temperature-time profile of any region of a real weld. In addition, such are the limitations of temperature control, that peak temperatures close to the melting point are not normally possible in the dilatometer because of the dangers of overshoot and specimen melting. As the peak temperature achieved and total time above the microalloy carbide solution temperature may have important effects on the extent of precipitate dissolution, these differences may be significant. In addition, there are geometrical factors which must, in principle, be considered. Whereas a dilatometer specimen is assumed to be at a uniform temperature throughout the thermal cycle, any point in the weld HAZ is always in contact with regions at higher and lower temperatures. Particularly at low heat inputs, when the HAZ may be extremely narrow and the instantaneous temperature gradient correspondingly steep, high-temperature grain growth behaviour may be affected. It is also important to remember that transformation does not occur simultaneously throughout the HAZ, and possible effects of the surrounding regions on transformation at any given point should be borne in mind.

Despite these difficulties, the results of this and previous investigations suggest that dilatometric techniques do give a reasonable indication of the transformation characteristics of real weld HAZs, and the compromise peak temperature, in this case, 1320°C and cooling conditions do lead to microstructures very similar to those in real welds. To illustrate, Fig. IV-1 shows a sequence of micrographs from both weld HAZs and dilatometer samples for steel B. Without prior knowledge, it is difficult to distinguish the real welds from the simulated microstructures.

\*Canadian Welding Development Institute

\*\*Noranda Research Centre

\*\*\*Dept. of Metallurgy &amp; Material Sciences, University of Toronto.





(a)



(b)



(c)



(d)

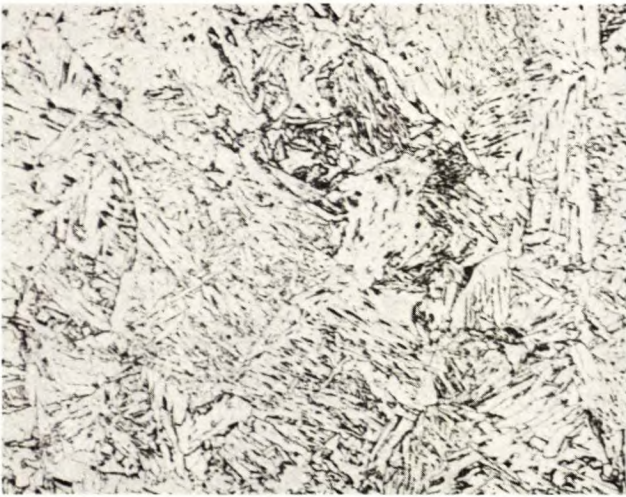


(e)

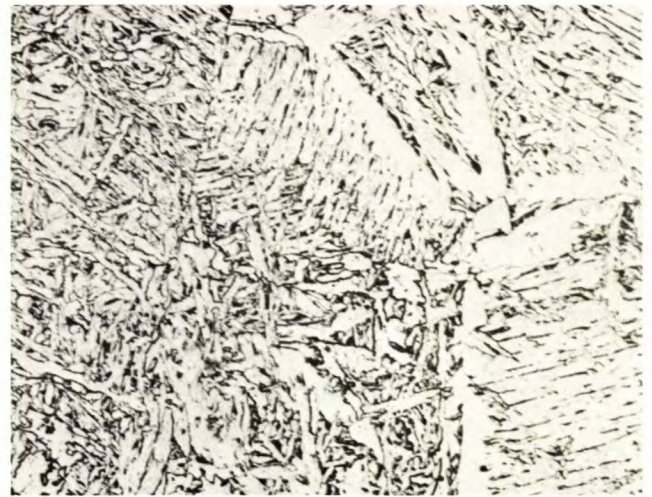
Fig. IV-1 - Microstructures of dilatometer samples and weld HAZs, steel B, x 200.

(a) Dilatometer,  $t_{500}^{800}$ , 3 s (b) Weld,  $t_{500}^{800}$ , 6.5 s  
 (c) Dilatometer,  $t_{500}^{800}$ , 10 s (d) Weld,  $t_{500}^{800}$ , 16 s  
 (e) Dilatometer,  $t_{500}^{800}$ , 30 s

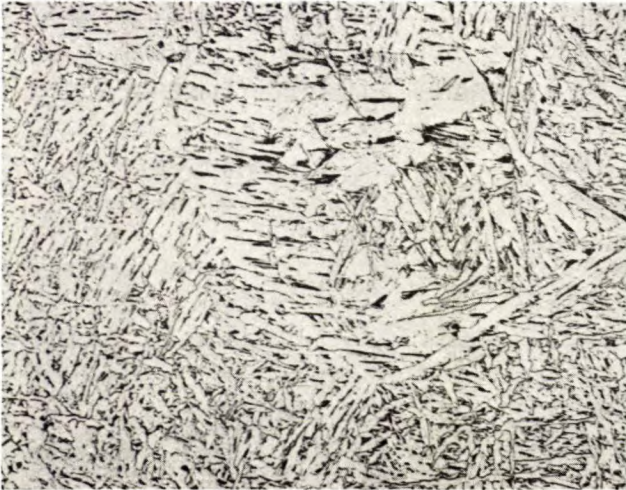




(f)



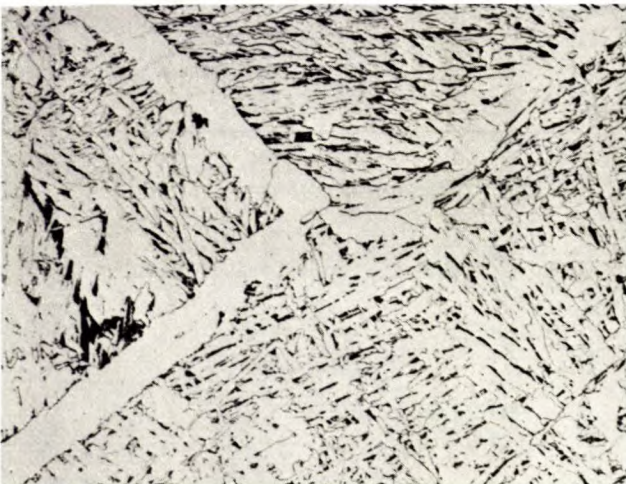
(g)



(h)



(i)



(j)

Fig. IV-1(cont'd) - Microstructures of dilatometer samples and weld HAZs, steel B, x 200.

(f) Weld,  $t_{500}^{800}$ , 39 s (g) Weld,  $t_{500}^{800}$ , 80 s

(h) Dilatometer,  $t_{500}^{800}$ , 100 s (i) Weld,  $t_{500}^{800}$ , 160 s

(j) Dilatometer,  $t_{500}^{800}$ , 300 s



The variation of hardness with composition and cooling conditions tends to reflect microalloy carbide dissolution and re-precipitation as well as general transformation behaviour. In Part II, Fig. II-28 and II-29 show that the dilatometer results follow similar trends to those observed in the welds, though at somewhat lower hardness levels. Hence, it is worth noting that the average macrohardness measured in the coarse-grained HAZ is commonly 20 to 30 HN below the highest value. The figures obtained in this work are a "mean maximum", i.e., the average of the highest individual readings from a number of sections of a given weld.

The variation of hardness with cooling conditions in each steel may be examined for consistency with the hypothesis of a precipitation-hardening reaction. In this respect, dilatometric results are particularly valuable because of the close metallurgical control the technique provides. The foregoing considerations suggest that any deductions made on the strength of dilatometric results may by extension be applied to the HAZs of welds. Figure IV-2 shows the variation of hardness with 50% transformation temperature for each steel. This method of presenting the results is based on the assumption that to a first approximation, for this group of steels, austenite transformation at a given temperature leads to similar microstructures and, thus, to similar hardnesses. In steel A, hardness falls steadily with increasing transformation temperature. For steels B, C and D, the curves appear to run parallel to that for steel A up to a temperature in the range of 520–540°C, after which hardness falls less rapidly in these niobium-containing steels. In steels B and C, there is some evidence of a return to a steeper slope at high transformation temperatures. Steels E, F, G and H show broadly similar behaviour, although the hardnesses of steels E and F do not appear to differ significantly from that of steel A at the lowest transformation temperatures. If these

results are replotted as the difference in hardness at a given transformation temperature between the micro-alloyed steels and steel A, the curves of Fig. IV-3 are obtained. Although some

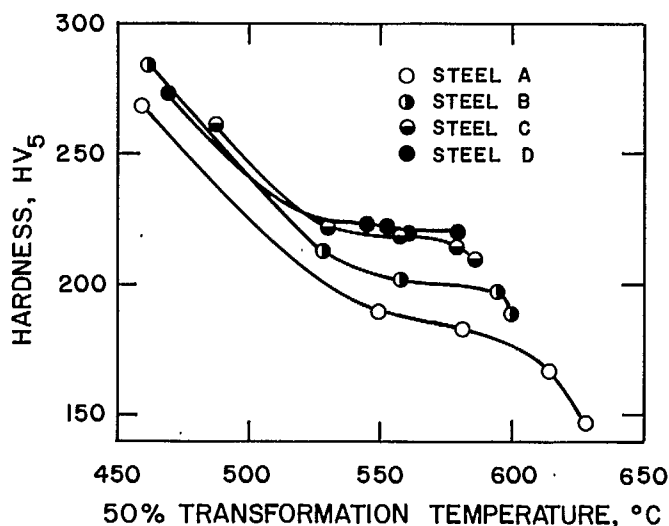


Fig. IV-2a - Hardness of dilatometer samples as a function of 50% transformation temperature, steels A-D.

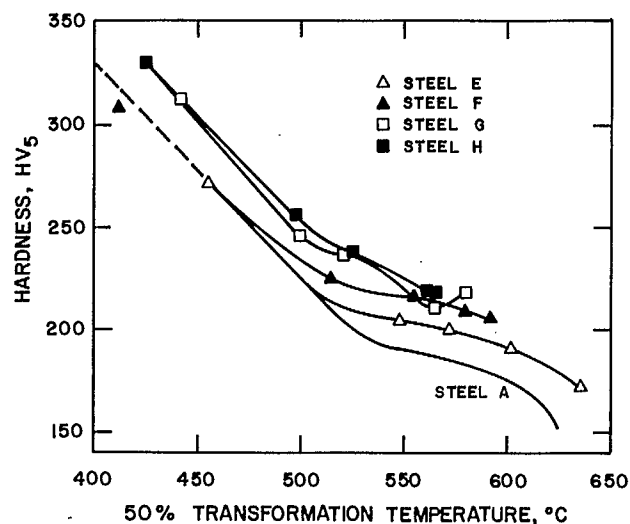


Fig. IV-2b - Hardness of dilatometer samples as a function of 50% transformation temperature, steels E-H.



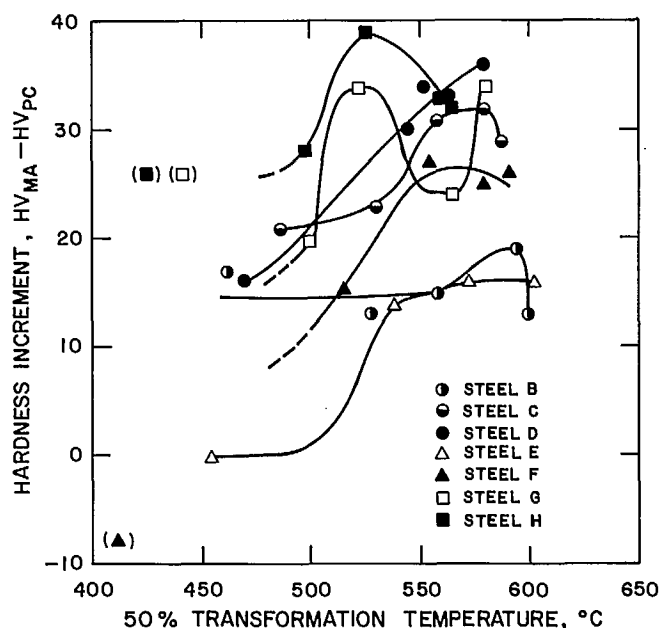


Fig. IV-3 - Hardness increment due to microalloying additions as a function of 50% transformation temperature.

are irregular, the form of these curves is suggestive of precipitation hardening behaviour, with some steels showing indications of peak hardening at temperatures in the range of 560-590°C. This is a very reasonable range for a maximum in microalloy carbide precipitation. It must be borne in mind, however, that the curves of Fig. IV-2 and IV-3 are not a simple reflection of the effect of temperature on hardening as, for each steel, a change in transformation temperature is brought about by a change in cooling rate. Both time and temperature are thus involved. However, attempts to take this factor into account, for example, by the use of a time-temperature parameter of the Holloman-Jaffe type, are not particularly successful. The reason for this is that the thermodynamics and kinetics of the precipitation reaction in austenite are very different from those in ferrite.

For all practical purposes, precipitation of microalloy carbides is not expected to occur in undeformed austenite during continuous cooling. The precipitation reaction will thus be confined at any temperature to that portion of

the sample which has already transformed or is currently transforming. The interactions between cooling conditions, transformation, and precipitation are thus too complex for any simple formalism to account for all variations in hardness. All that can be said is that the differences in hardness between steel A and the microalloyed steels at transformation temperatures above 530°C can plausibly be accounted for by reprecipitation of alloy carbides dissolved during the high-temperature portion of the thermal cycle. The differences which persist at lower transformation temperatures could conceivably be due to precipitate dispersions which survive the rapid thermal cycles. The short times available at high temperature shown in Part II, lend force to this argument. The fact that steels E and F, containing only the readily soluble vanadium carbide or a vanadium rich mixed carbide, show no hardness increment, is not inconsistent with the hypothesis of reprecipitation.

Finally, Fig. IV-4 shows the variation of hardness with 50% transformation temperature for the weld HAZs, the transformation temperatures being taken from the CCT diagrams in Part II, using the measured weld cooling times. The hardness variations are clearly broadly similar to those in Fig. IV-2, although, not unexpectedly, there are greater irregularities in these curves. Here too, the observed hardness variations are consistent with the dissolution and reprecipitation of microalloy carbides during thermal cycles characterized by 50% transformation temperatures above 530°C. In general, the variations of hardness with cooling rate of both welds and dilatometer samples provide strong, albeit circumstantial support for the hypothesis of hardening due to the precipitation of microalloy carbides during the cooling portion of the slower thermal cycles.

#### Toughness, hardness and microstructure in as-welded and stress-relieved HAZs

Closer analysis of the hardness and toughness changes associated with stress relieving will allow further conclusions to be drawn



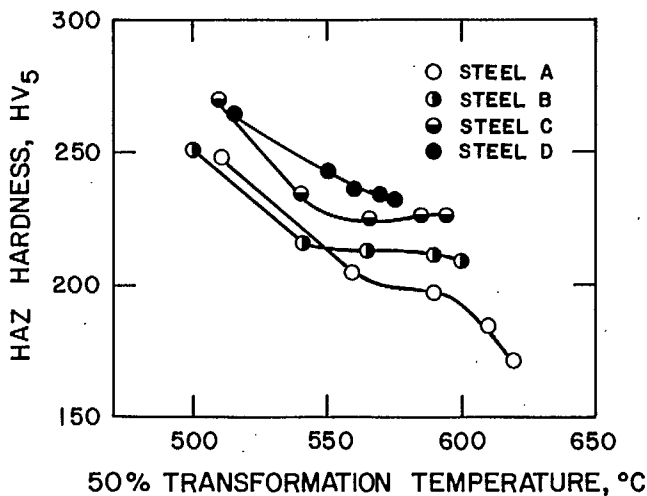


Fig. IV-4a - Hardness of weld HAZ as a function of 50% transformation temperature, steels A-D.

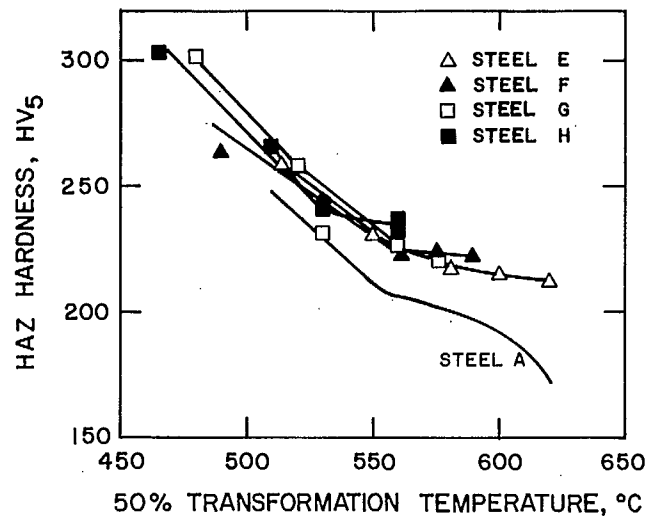


Fig. IV-4b - Hardness of weld HAZ as a function of 50% transformation temperature, steels E-H.

concerning the role of microstructure in determining toughness. In Part III of this report, some of the hardness results referred to measurements using a Vickers machine with a 10-kg load, while others were made on a microhardness tester with a 200-g load. For consistency and to allow

more detailed analysis of the results, further tests were carried out using the microhardness tester on stress relieved welds and as welded samples of the 2.4 kJ/mm set. The results are given in Fig. IV-5 and IV-6, where hardness traverses are shown for the four steels A, C, F and

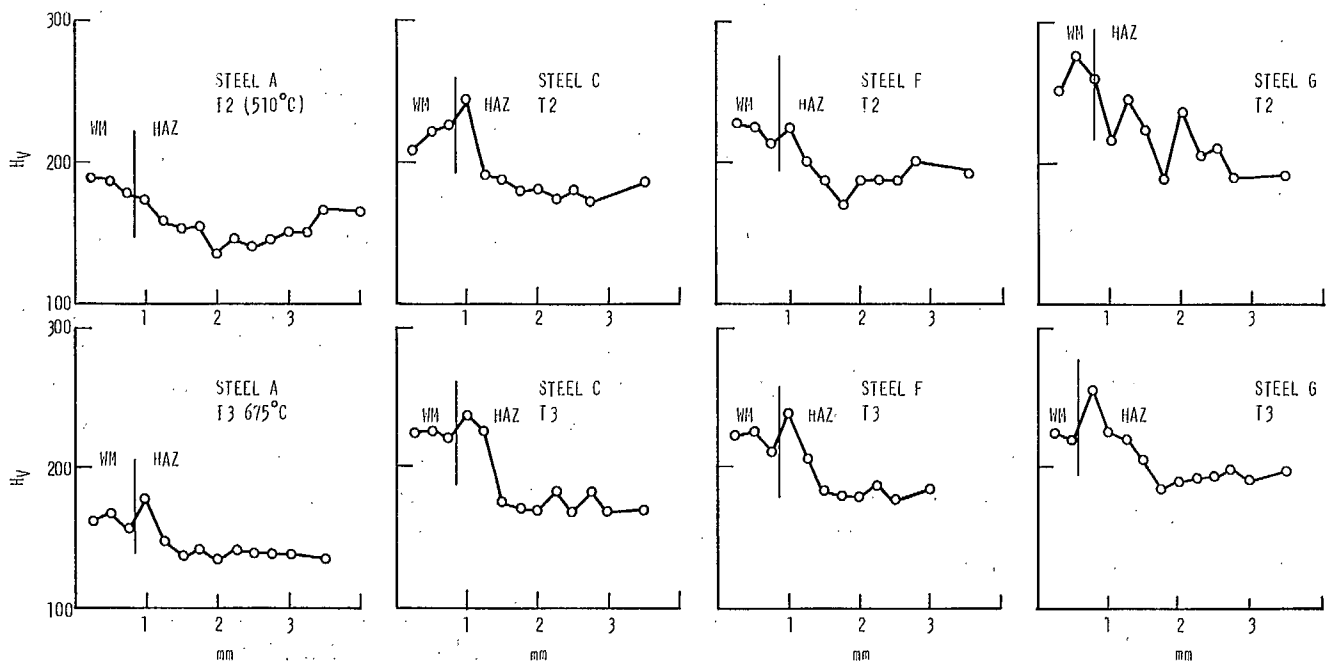


Fig. IV-5 - Microhardness results (200 g) for four steels after stress relief at 510°C and 675°C



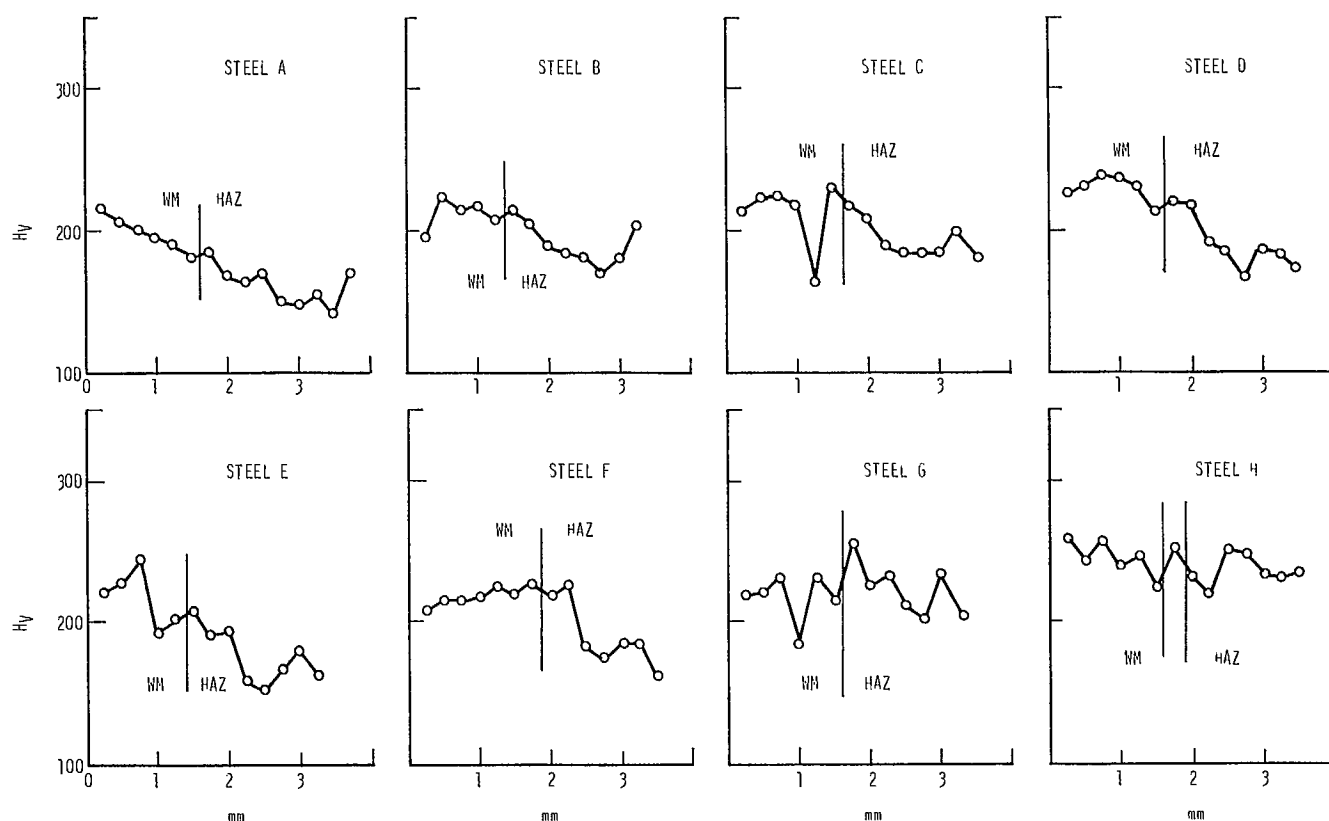


Fig. IV-6 - Microhardness (200 g) results for all steels in the as-welded condition for the 2.4 kJ/mm heat input at cooling time (800°C - 500°C) of 39 s

G, stress-relieved at temperatures T2 and T3 (nominally 510 and 675°C, respectively), after welding at a heat input of 2.4 kJ/mm. In Fig. IV-7, the results are replotted as maximum HAZ hardness against stress relief temperature. For the unalloyed A steel, the hardness decreases slightly with increasing temperature, in both HAZ and parent material. In steels, C, F and G, where hardness results for three stress-relief temperatures were available, a peak in the hardness is noted at T1, 620°C.

In all steels, the HAZ hardness is considerably higher than that in steel A after stress relief. To determine the relation between shift of transition temperature and change of hardness, two types of plots were made. In the first, the transition temperature of steel A is subtracted from that of the other steels and plotted against the HAZ hardness less that of steel A. The plot

thus shows the increase of transition temperature and hardness due to alloying.

Results are shown in Fig. IV-8 for both the stress relieved and as welded conditions. The points fit a straight line quite well and the slope of 1.2°C per unit of hardness equivalent to 1.7-2.1 MPa increase in yield strength is in reasonable agreement with reported values of the precipitation hardening vector (2). It is noted that the line does not appear to pass through the origin, indicating that there is a component due to alloying that shifts the transition temperature downwards without being associated with a change in hardness. This component cannot be identified from the data available, but may be associated with a change in the effective bainite colony size. In Fig. IV-9, the macrohardness of all welds is plotted and although there is considerable scatter, it is clear that, once again,



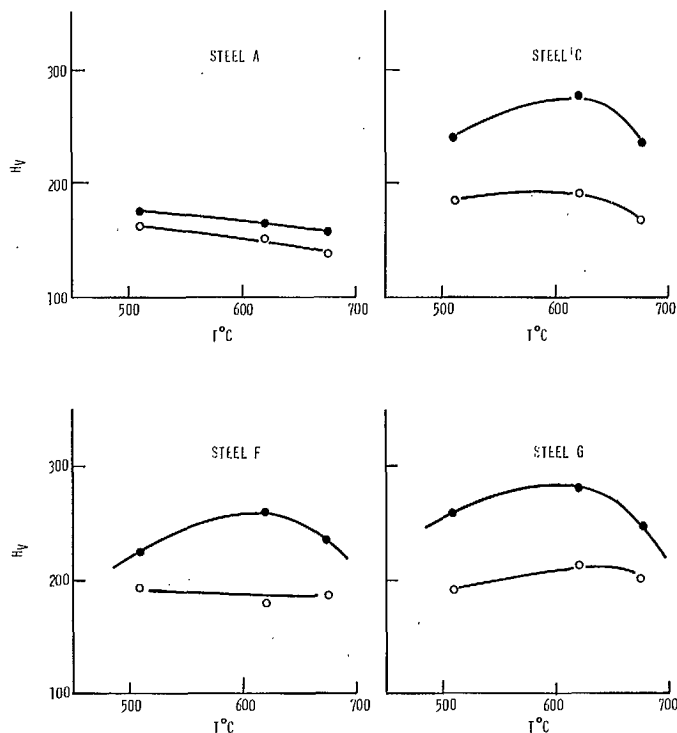


Fig. IV-7 - Effect of stress-relief temperature on hardness. Solid points are for the HAZ and open points for the parent metal. All welds 2.4 kJ/mm heat input.

the trend is not through the origin. This emphasizes the non-precipitation hardening component, although its magnitude may vary with the energy input during welding, as well as with steel composition.

In the second type of analysis, the effects of stress relieving are examined by subtracting the as welded results from the stress relieved results for each steel. The transition temperature shift is plotted against the hardness change due to stress relief in Fig. IV-10. Although results are scattered, a clear trend exists and the slope of the line is similar but a little higher than that in Fig. IV-8. The line clearly passes through the origin and indicates that all changes of transition temperature due to stress relief are associated with a change in hardness. The only mechanism which could lead to an increase in hardness on stress relief is precipitation hardening. For steel A, however, stress relief brings softening.

These results show that the change in transition temperature due to alloying in high energy welds and after stress-relieving results from an increase in the HAZ hardness, precipitation hardening being the principal mechanism involved. In the as welded condition, even with quite high energy welds, only a small part of the full precipitation hardening potential available in the niobium steels is revealed, whereas large increases in hardness can result from stress relieving. The niobium free vanadium steel E, on the other hand, appears to show no significant increase in precipitation strengthening on stress relief; and no deterioration in toughness occurs.

The effects of alloying are further illustrated in Fig. IV-11, where the difference between the HAZ hardness of the seven alloy steels and steel A is plotted against cooling time for the as welded samples. For steels B to F, the difference increases with longer cooling times, as more time is available for precipitation.



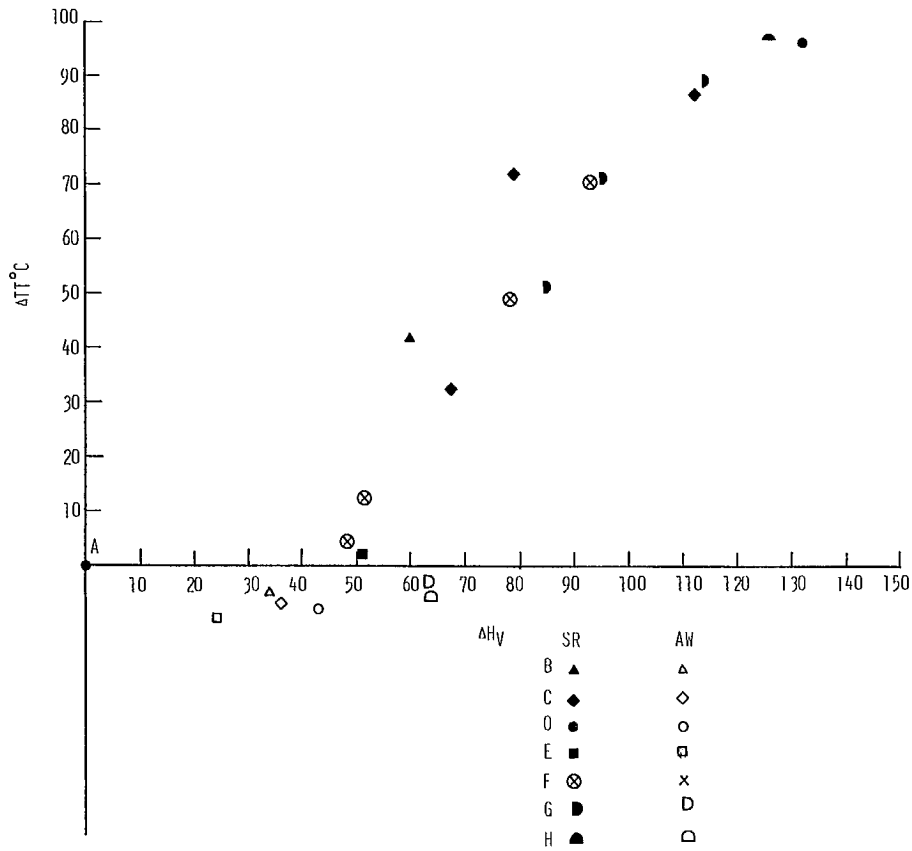


Fig. IV-8 - Plot of transition temperature shift against hardness increase relative to steel A. Both stress-relieved and as-welded data are included; all points for 2.4 kJ/mm and microhardness (200 g) values.



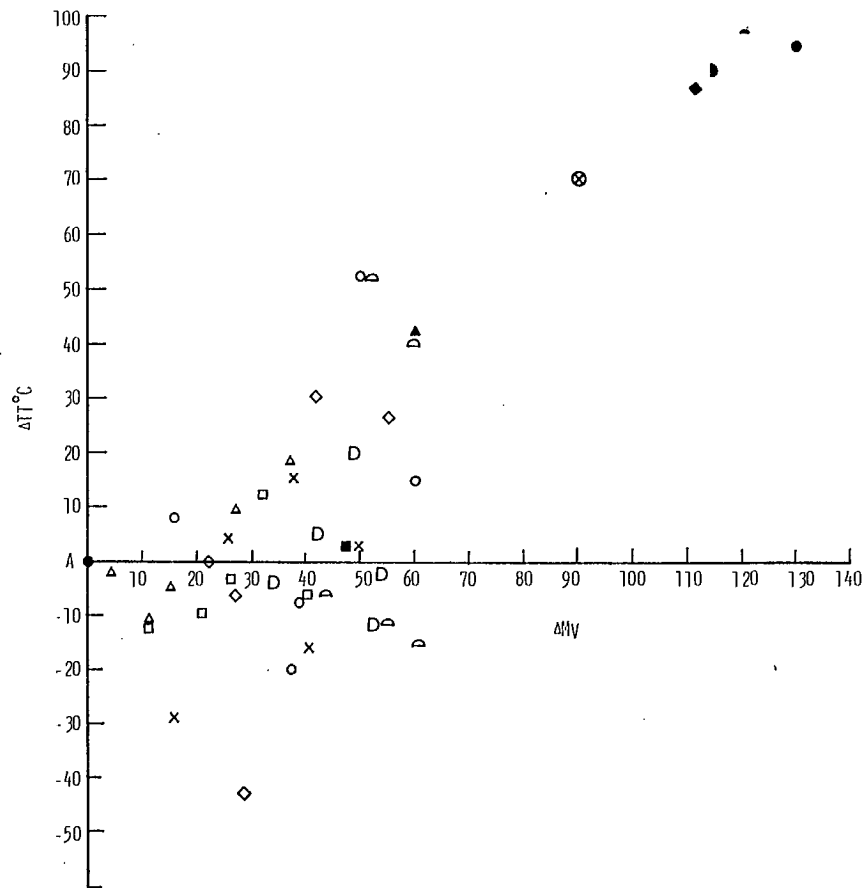


Fig. IV-9 - Plot of transition temperature shift against hardness increase relative to steel A; all results from all welds, both as-welded and stress relieved, included; all points are macro-hardness (10 kg) values.



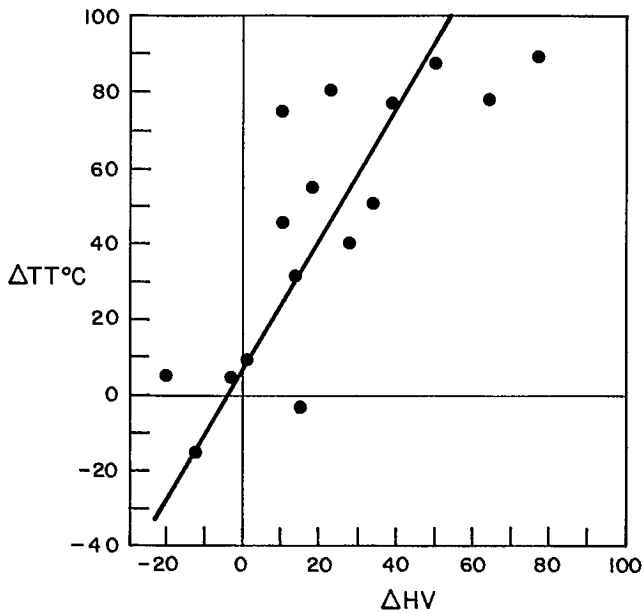


Fig. IV-10 - Plot of transition temperature shift against hardness increase in stress-relieved welds relative to as-welded values; 2.4 kJ/mm welds and microhardness (200 g) values.

The hardness data in Fig. IV-11 reflect the combined contributions to hardness of austenite transformation as well as carbide/nitride precipitation. Thus, the  $\Delta H N$  values are generally higher than for corresponding data in Fig. IV-4, where to a first approximation, transformation effects have been eliminated. For example, as was shown in Fig. II-27, Part II, niobium suppresses the transformation temperature at longer cooling times and, in this way results in increased hardness. The effect is evident in Fig. IV-11. Again, with the addition of molybdenum in steels G and H, the increase in hardness remains roughly constant at all cooling times. This simply reflects the effect of molybdenum on hardenability at short cooling times. As the hardenability decreases at longer cooling times, its effect on hardness is replaced by precipitation hardening.

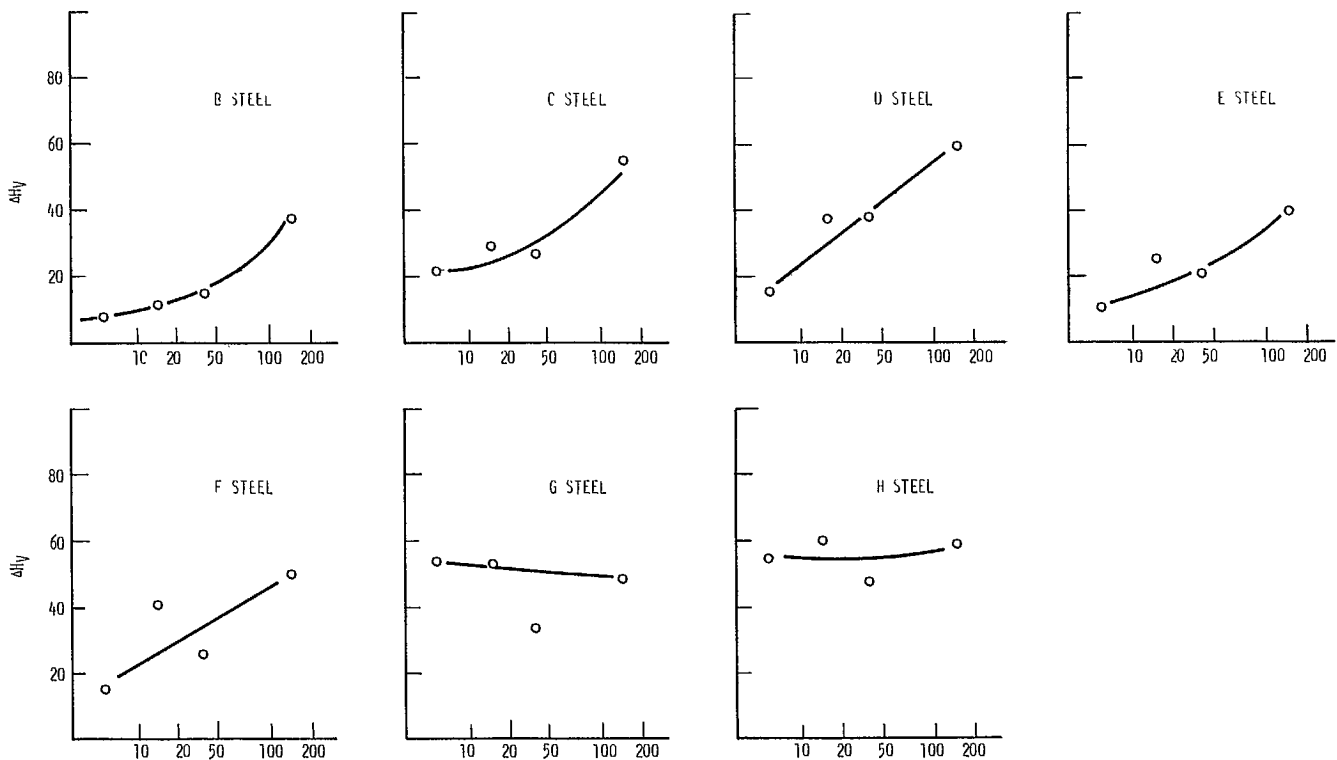


Fig. IV-11 - As welded HAZ macrohardness relative to steel A as a function of cooling time between 800°C - 500°C.



### Summary of microstructural effects

The combination of chemical composition and thermal cycle can interact in a number of ways to influence microstructure, strength, and toughness. For example, the importance of grain size is well known. In structures consisting of packets of parallel laths, however, the microstructural features must be chosen appropriately, as the effective grain size for strength is different from that for toughness (2). Yield strength increases with decreasing distance between lath boundaries, but these low angle boundaries are not effective obstacles to fracture (3), and hence, toughness can only be improved by decreasing the size of the packets or colonies. This leads to two conclusions of significance for weld HAZs. A refinement in colony size will normally only result from a refinement in austenite grain size, which in turn depends primarily on the thermal cycle, particularly in the high-temperature regime as explained in Part III. Low heat inputs, leading to short times at high temperature and, perhaps equally important, steep thermal gradients close to the fusion boundary, will lead to a finer austenite grain size. Under some conditions, the presence of microalloy carbide or carbonitride precipitates could conceivably exercise restraint on austenite grain size. No significant differences were noted in the present work at constant cooling rate, Part III, Table III, but dispersions of particles are known to be achievable, for example, in steels containing titanium and nitrogen, and worthwhile improvements in toughness result (4).

By contrast, a decrease in lath size with no change in packet size, which will normally result from decreasing transformation temperature, should lead to a deterioration in toughness, as it will raise the yield strength without increasing the resistance to fracture.

Dislocation density will generally increase with decreasing transformation temperature, for example as a result of increasing cooling rate or hardenability, and this will lead to an increase in strength and concomitant de-

crease in toughness. The toughness/strength vector for dislocations has been estimated as  $0.25\text{--}0.4^\circ\text{C}/\text{MPa}$ , i.e., of the same order as that for precipitation strengthening (2,5).

As discussed above, hardening resulting from the dissolution of carbides or carbonitrides at high temperatures, followed by reprecipitation during cooling, is expected to lead to a deterioration in toughness. According to the Ashby-Orowan formalism, a decrease in average particle size, or an increase in volume fraction precipitated, will lead to an increase in strength (2). A rapid thermal cycle may not allow sufficient time for dissolution at high temperature, and, as precipitation in undeformed austenite under continuous cooling conditions is expected to be negligible, the associated low transformation temperature should suppress any tendency toward precipitation. Slower thermal cycles, leading to higher transformation temperatures, will allow more complete solution and precipitation, although particle sizes may ultimately become coarse. Stress relief heat treatment in the range of  $500\text{ to }700^\circ\text{C}$  will generally lead to the precipitation of whatever microalloy remains in solution with a resulting increment in hardening. As regards the quantitative aspects, the following calculations, based on the Ashby-Orowan equation, may be of interest.

Hardness increments owing to microalloy precipitation in the as welded state were about 30-40 HV. The corresponding yield strength increment is about 50-65 MPa, and the accompanying deterioration in impact transition temperature around  $25\text{--}30^\circ\text{C}$ . The volume fraction of 0.025 wt % niobium as 5 nm NbC particles is  $\sqrt{0.00028}$  which would be sufficient to account for hardness and strength increases of this order. Complete precipitation of 0.14 wt % niobium as 5  $\mu\text{m}$  precipitates, as could occur during stress relieving, would give an increase in yield strength of  $\sqrt{120}$  MPa and a deterioration in transition temperature of  $\sqrt{60}^\circ\text{C}$ . Clearly, the results of the experimental work and these foregoing estimates are consistent although it is not suggested

than an exact numerical match should exist (1).

Apart from precipitation, low-carbon martensite formed at fast cooling rates is generally held to be intrinsically tougher than the bainitic structures which follow intermediate cooling rates. Presumably, one reason is the elimination of coarse, brittle, lath-boundary carbides or martensite-austenite (M-A) aggregates, although fast thermal cycles also usually reduce austenite grain size. The replacement of bainitic structures by more randomly oriented ferrite at the longest cooling times would be expected to improve toughness, but this in turn may be offset by coarse austenite grain size and enhanced precipitation hardening.

Figure IV-12 illustrates schematically the way in which the principal microstructural effects can combine to determine toughness. Evidently, with practical alloy systems, the outcome of a particular thermal history depends sensitively on the balance achieved between these several factors.

#### General conclusions

1. For thermal cycles giving cooling times 800 to 500°C of 40 or less, toughness is

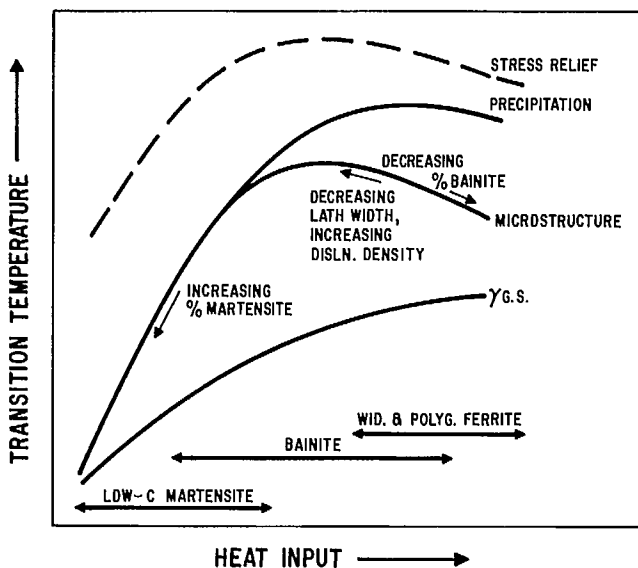


Fig. IV-12 - Schematic illustration of effects of microstructural parameters on HAZ toughness.

not expected to suffer unduly when making single-pass welds in microalloy steels of commonly adopted compositions. This cooling time corresponds to a heat-input of 2.4 kJ/mm on a  $\sqrt{12}$  mm plate. With plate of  $\sqrt{50}$  mm thickness, a heat input greater than  $\sqrt{8}$  kJ/mm would be needed to exceed this limit.

2. The observed toughness is a complicated function of many microstructural variables but, in the range of cooling times  $\geq 40$ s, precipitation hardening due to microalloy carbides or nitrides does contribute to a deterioration in toughness. The effect appears to be small in the as-welded condition, but with niobium steels, it becomes serious on stress relief.

3. The effects of austenite transformation are superimposed on the effects of precipitation, and the result is a complex variation in toughness with thermal cycle. The apparent contradictions in the literature are thus not surprising, and every effort must be made to assure comparability of base composition, welding conditions and test technique when attempting to predict the effects of microalloy elements on toughness. However, the effect of multiple pass welding remains to be clarified, although existing results suggest that, in typical microalloy compositions, toughness will be at least as good as that achieved in single pass welds made under similar cooling conditions (6,7).

#### References

1. McGrath, J.T., Glover, A.G. and Weatherly, G.C. "Heat-affected-zone toughness of welded joints in micro-alloy steels, Part III"; April, 1978.
2. Gladman, T., Dulieu, D. and McIvor, I.D. "Microalloying 75"; p 32. Union Carbide, New York; 1977.
3. Rothwell, A.B., Glover, A.G., McGrath J.T. and Weatherly, G.C.; Proc 5th Bolton Landing Conf 1978; Schenectady, N.Y., GEC; in press.
4. Rothwell, A.B., Glover, A.G., McGrath, J.T. and Weatherly, G.C.; to be published.
5. Pickering, F.B. "Microalloying 75"; New York; Union Carbide; p 9; 1977.



6. Bonomo, F., Centro Sperimentale Metallurgico,  
1203R; 1972.

7. Bonomo, F. and Capoccia, G., Centro Sperimentale Metallurgico; 1837R; 1974.

## APPENDIX A

## INSTRUMENTED IMPACT TRANSITION CURVES

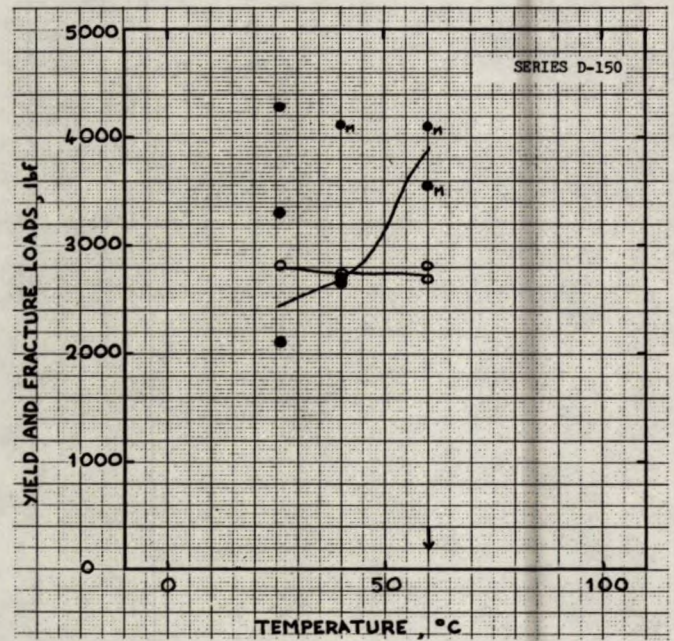
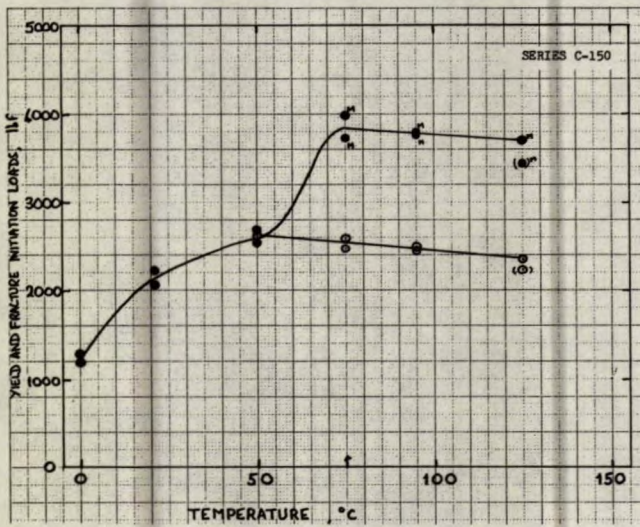
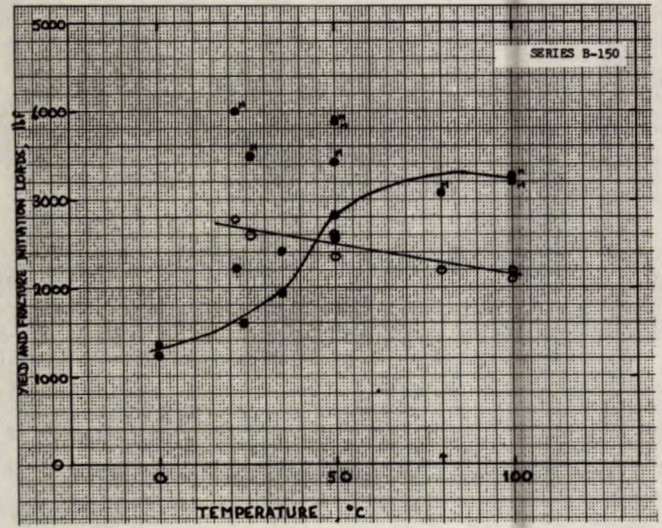
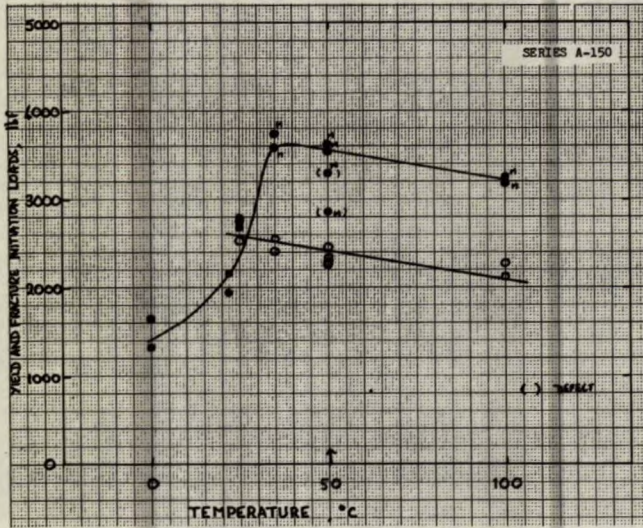
This appendix contains the individual transition curves for the eight experimental steels welded with five levels of heat input and also the sixteen curves pertaining to the stress-relieved condition. All experimental details will be found in Part I of this report.

Key

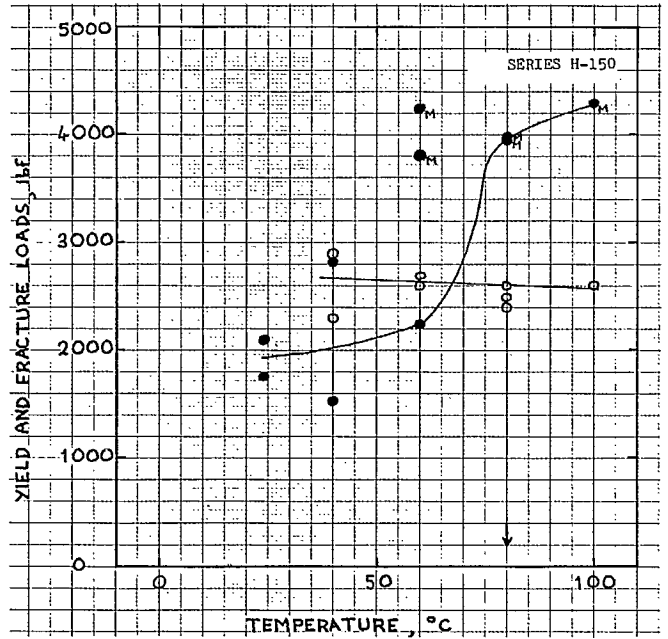
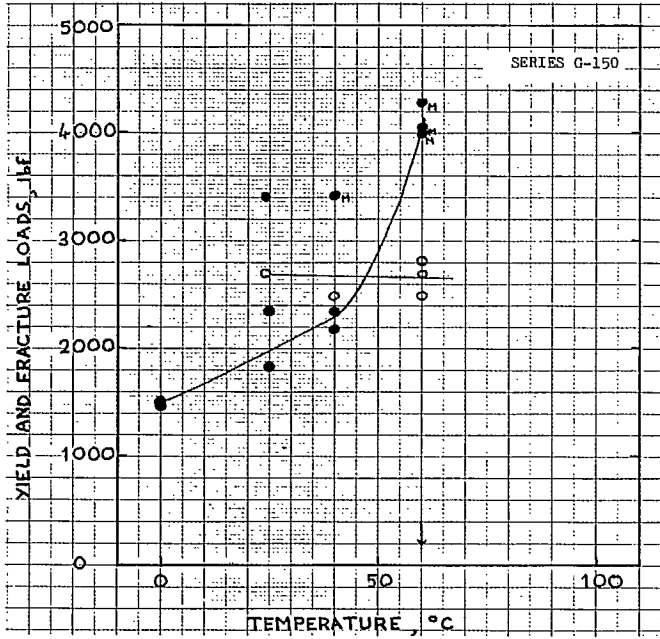
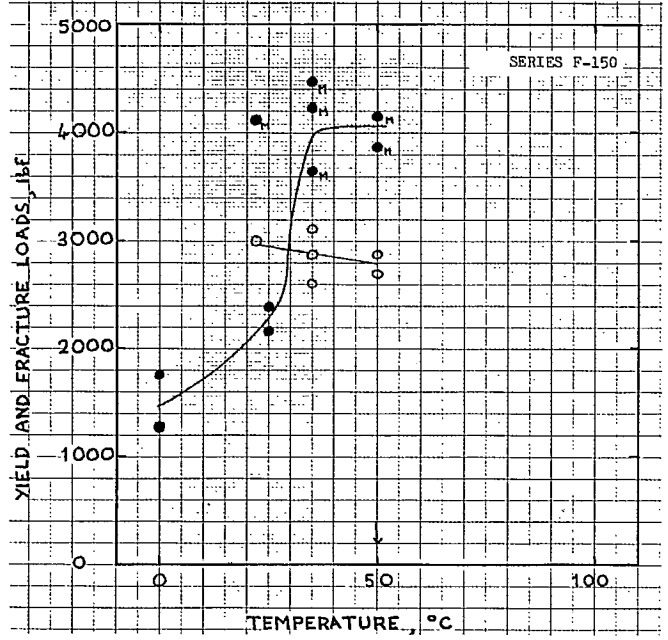
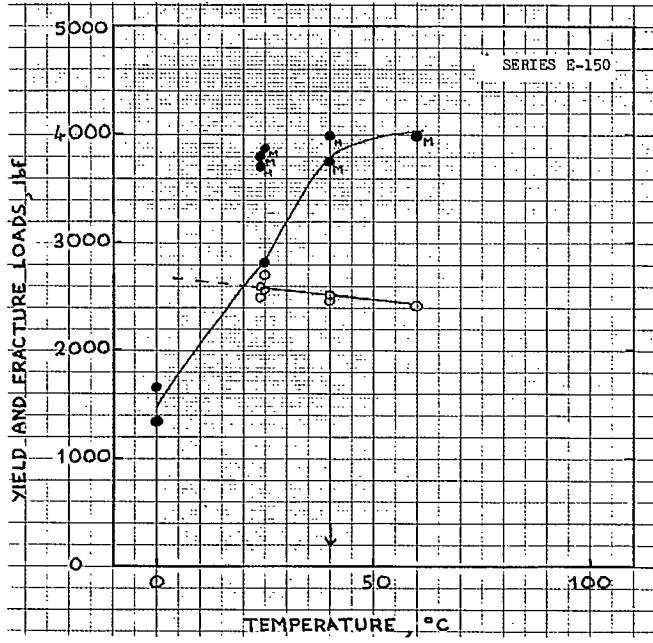
- Yield load
- Fracture load
- Maximum load
- Brittle crack extension, no load instability
- ↑ Minimum temperature for fully ductile initiation

Nominal stress relief temperatures: T1 620°C  
T2 510°C  
T3 675°C

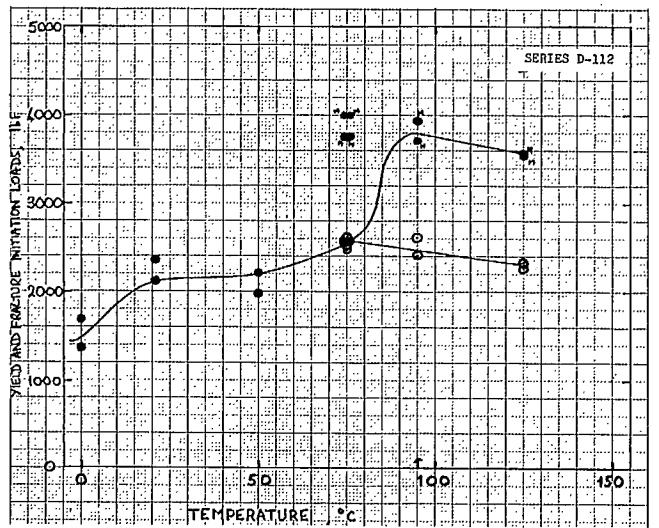
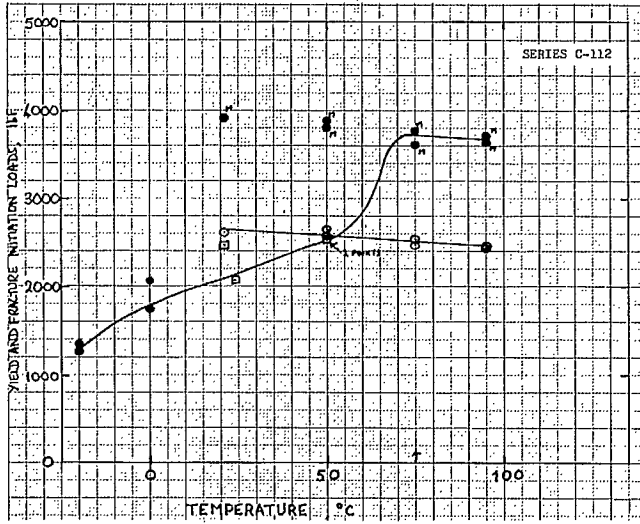
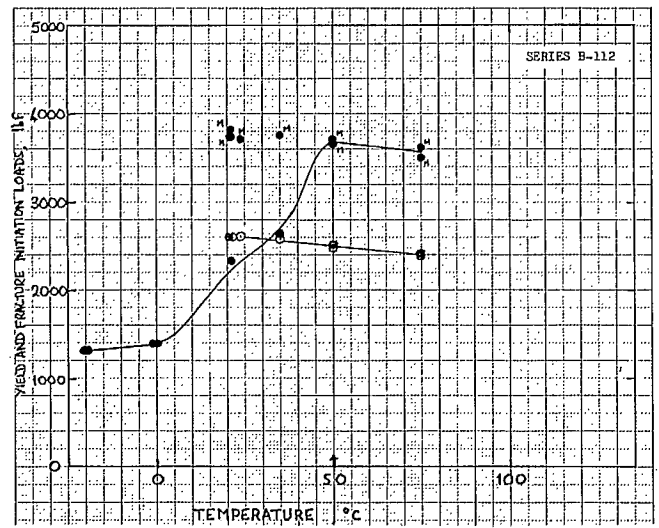
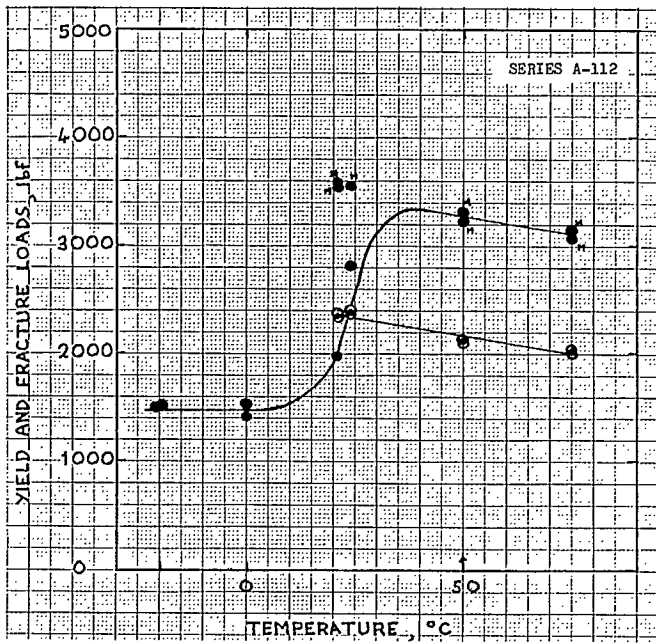


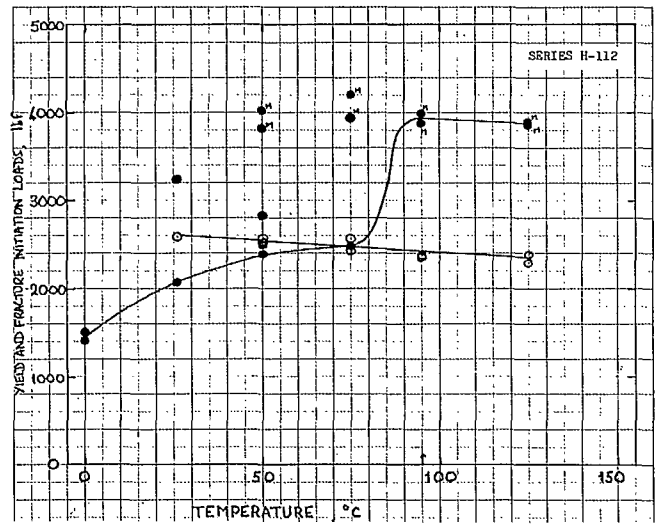
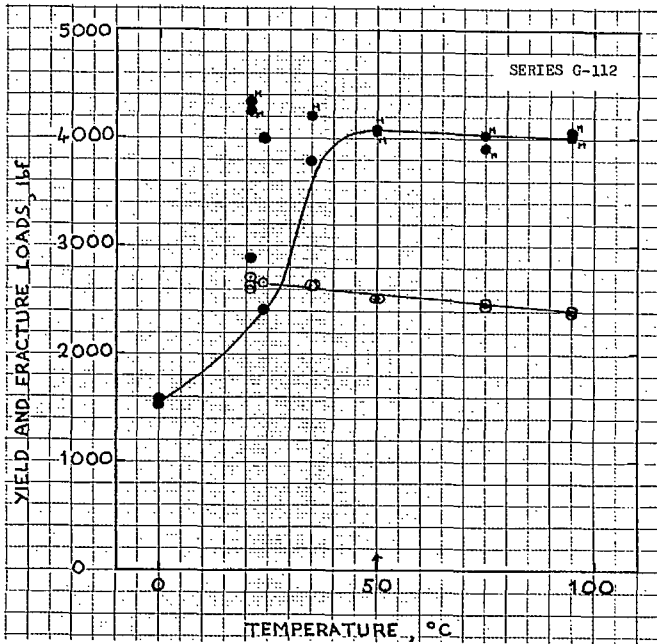
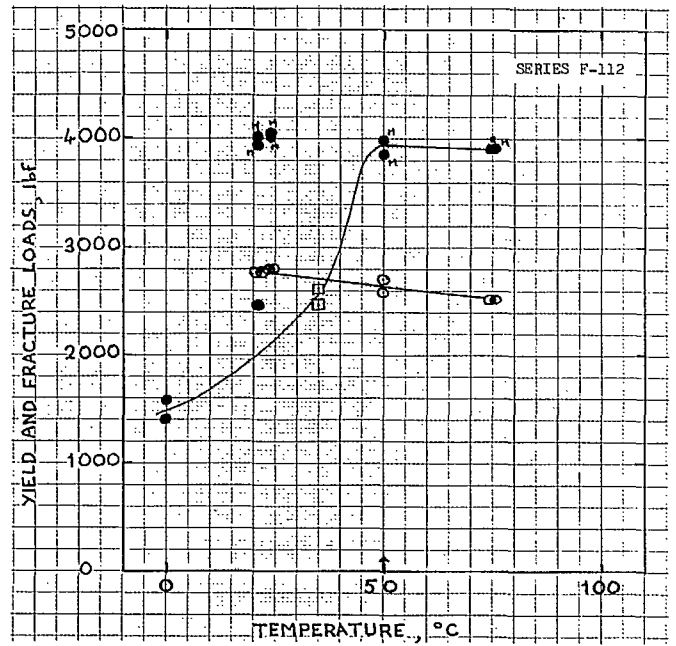
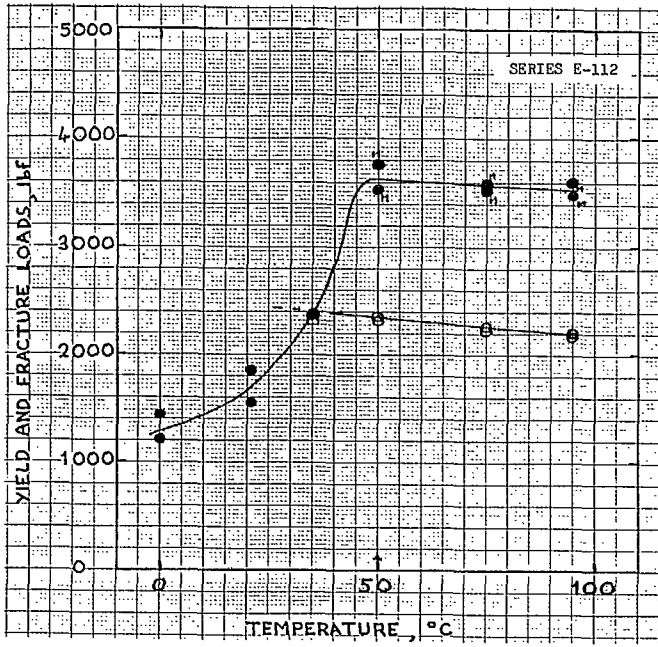




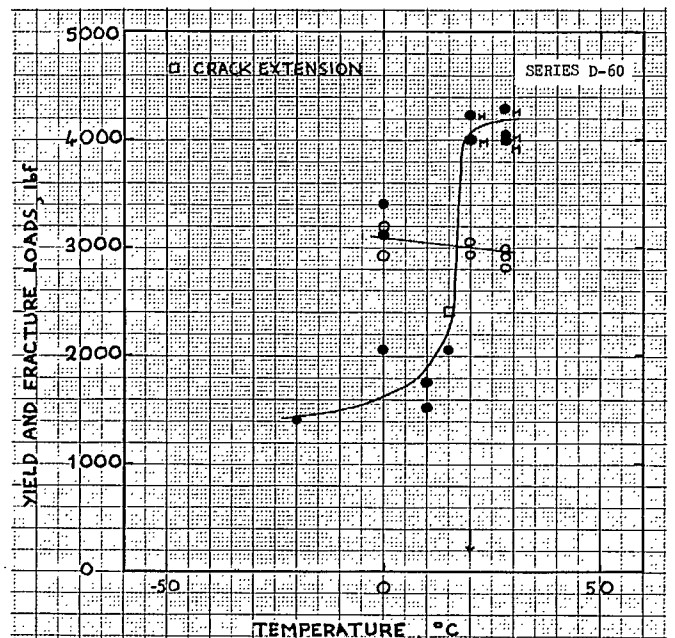
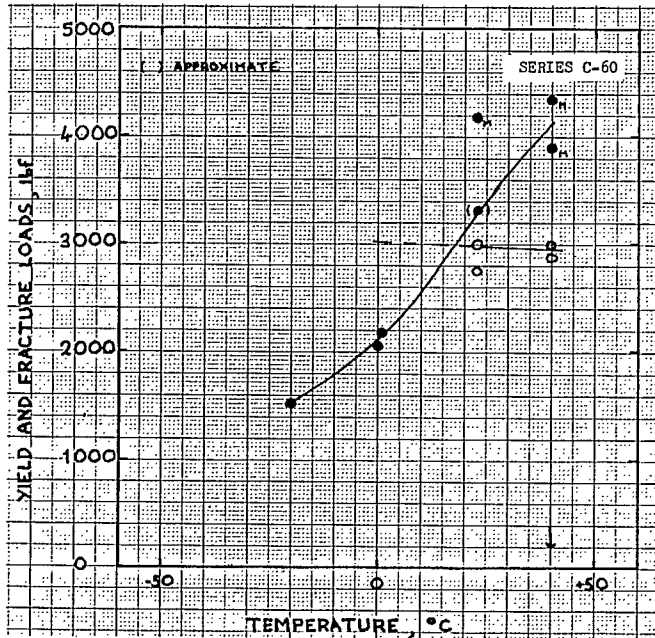
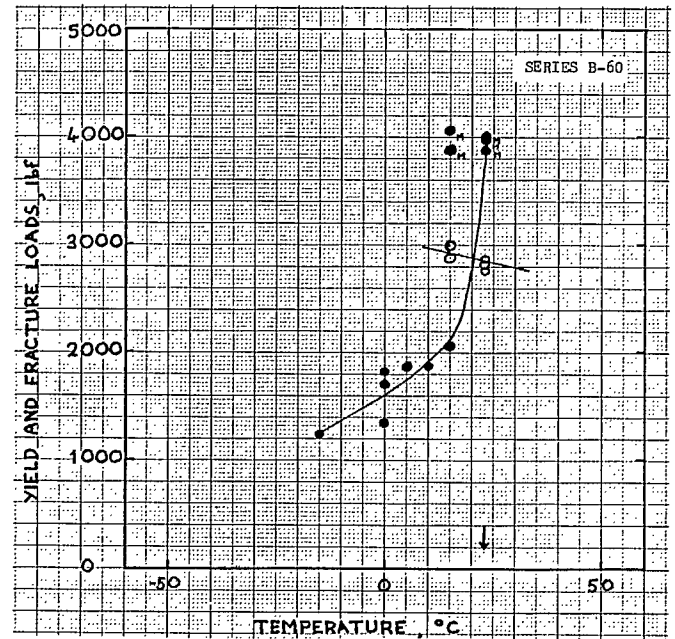
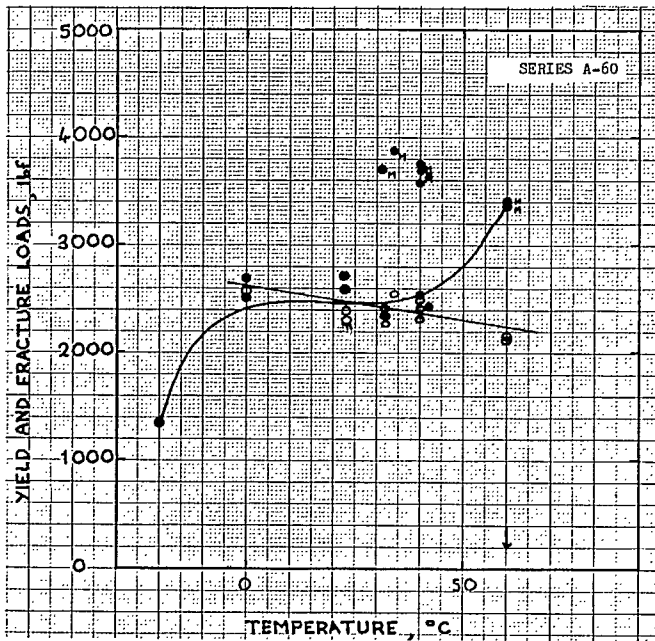


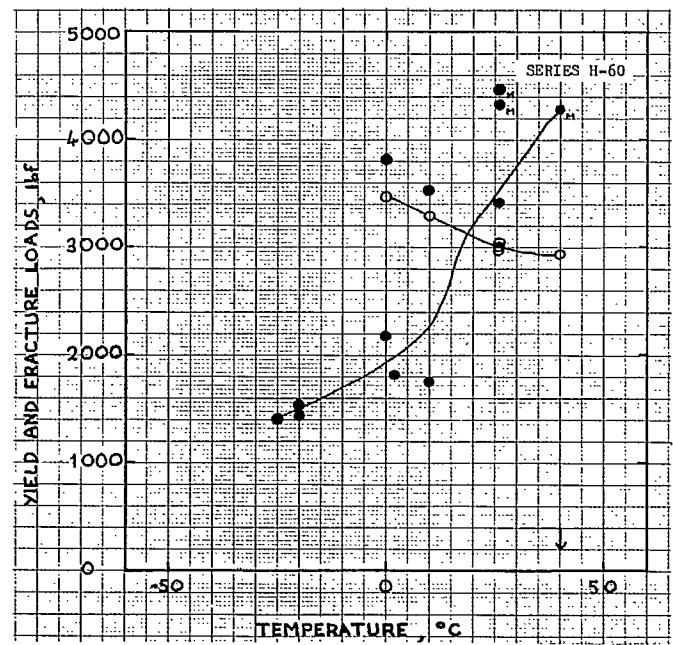
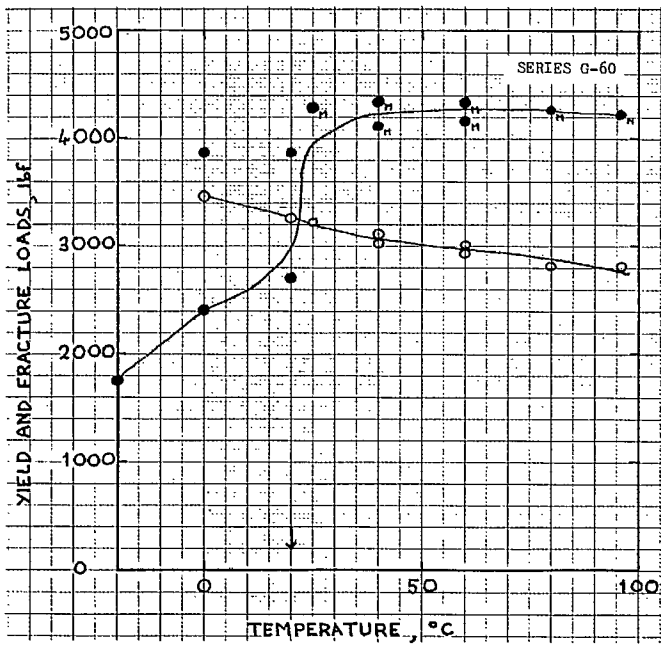
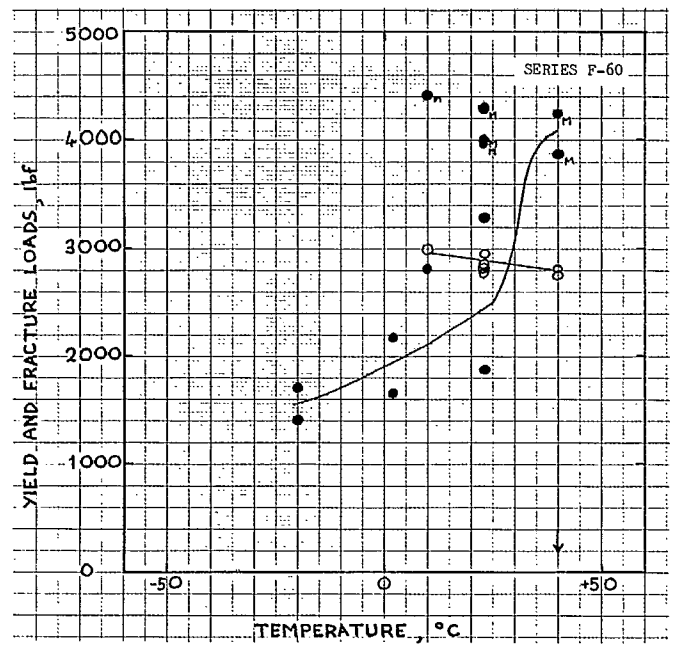
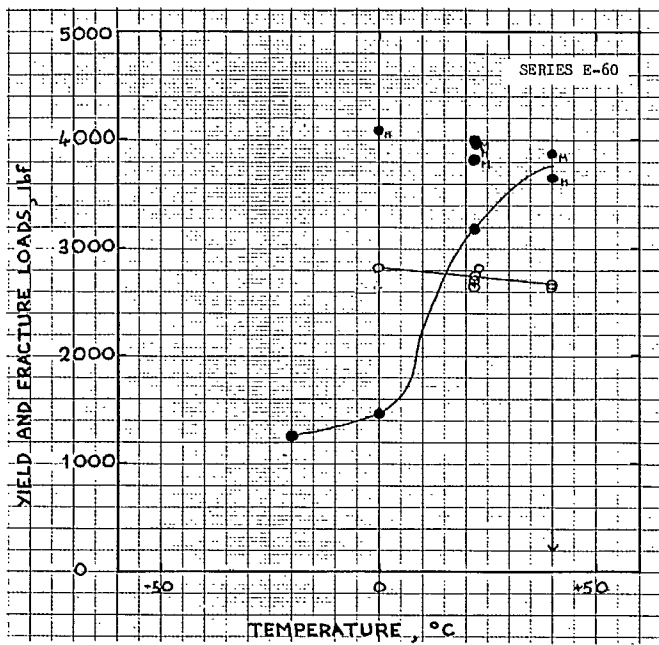




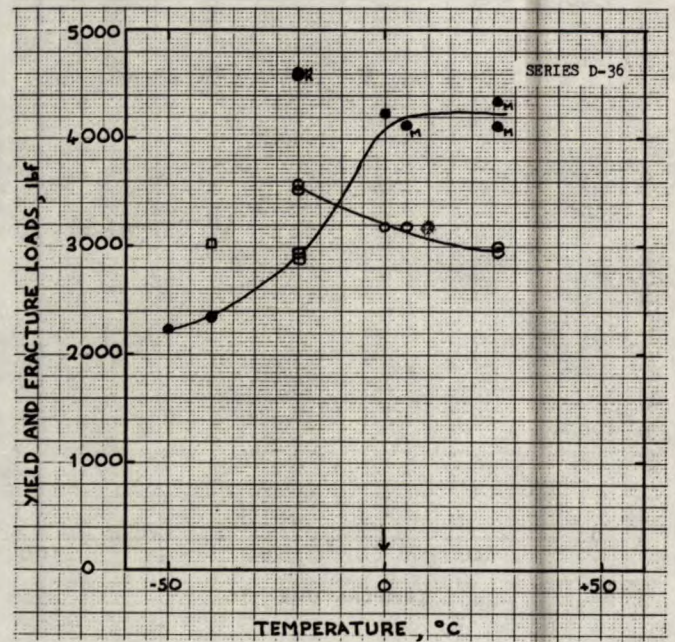
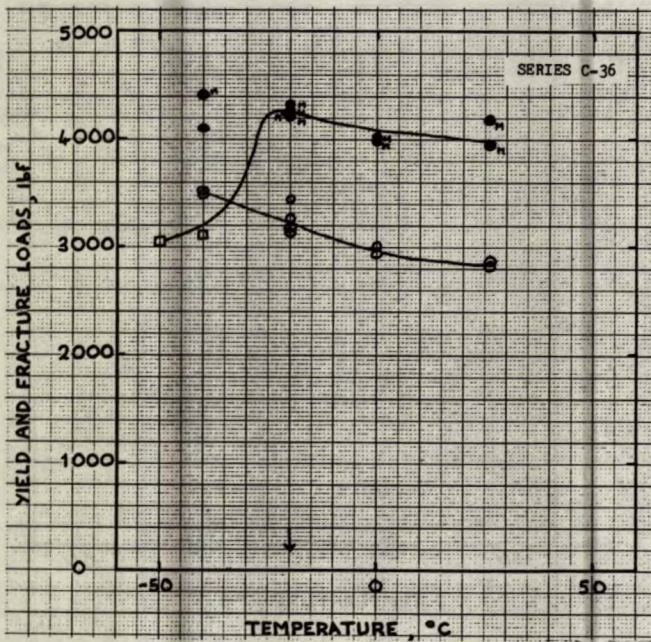
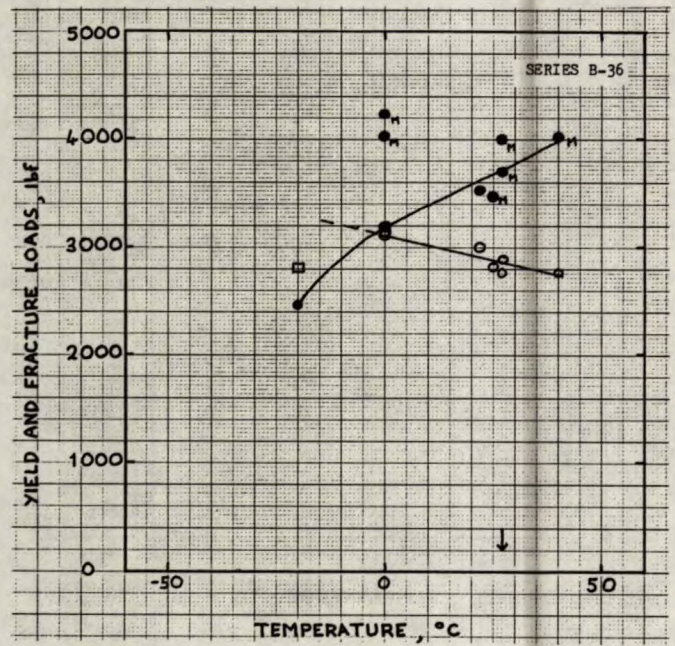
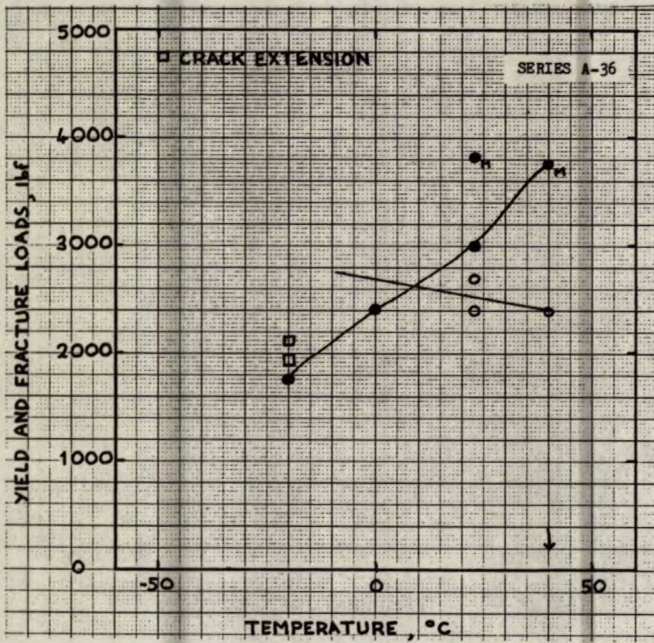




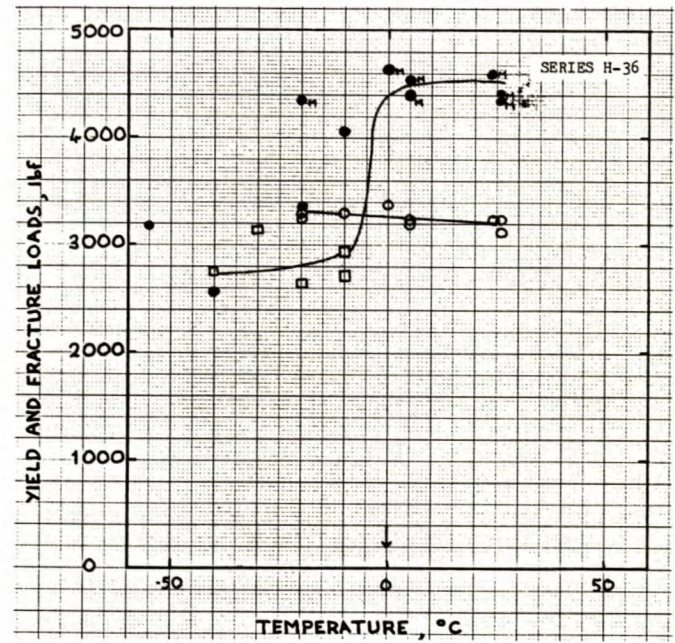
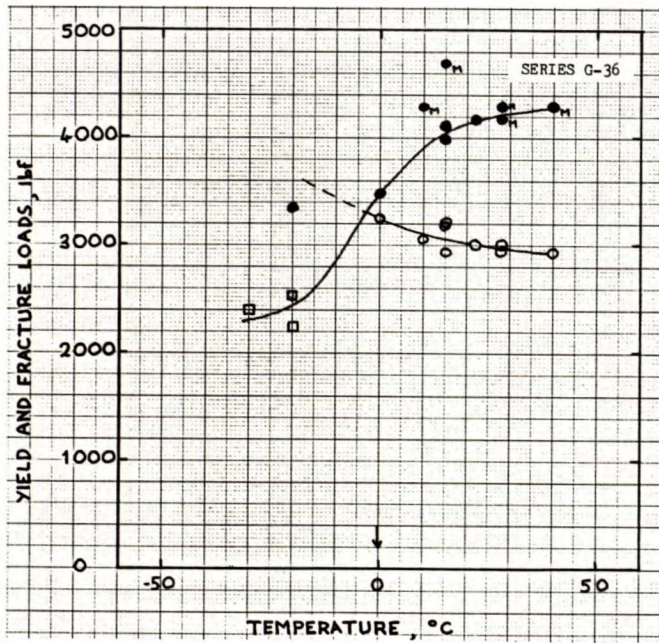
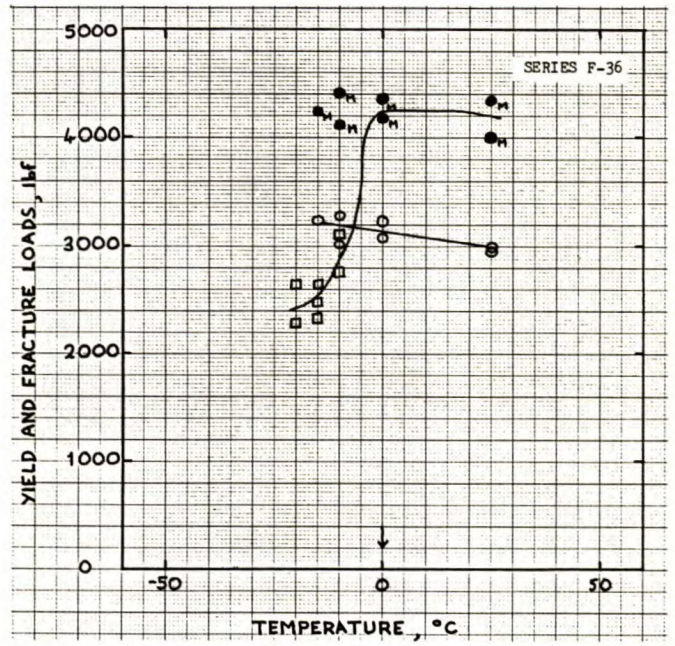
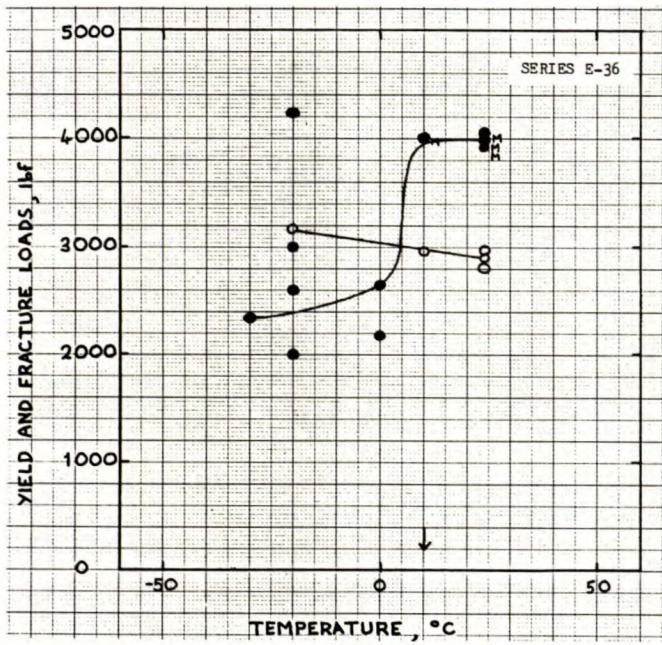




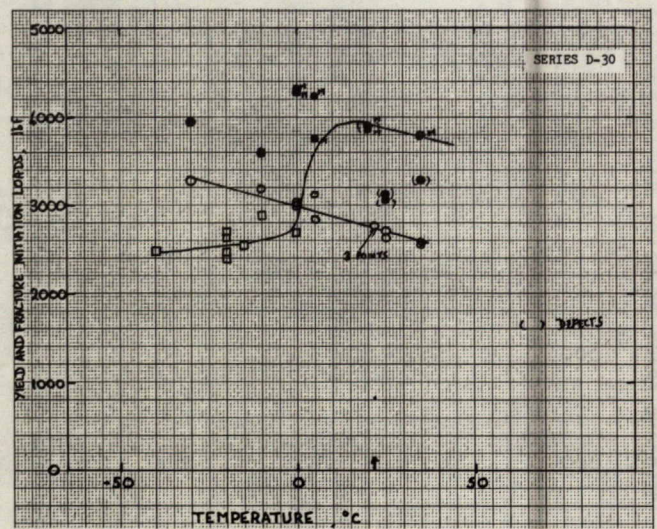
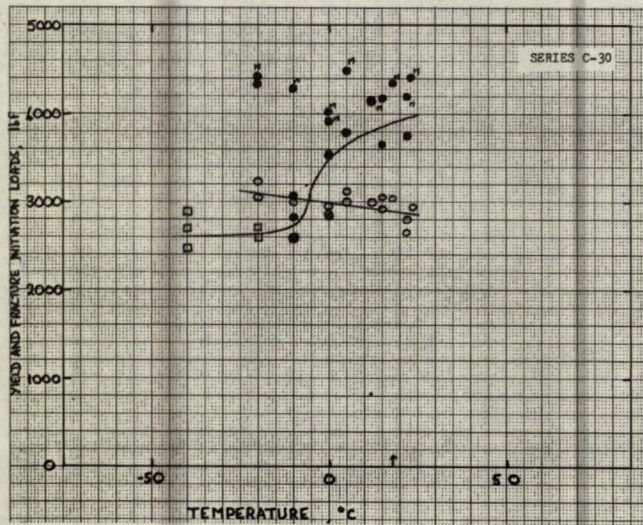
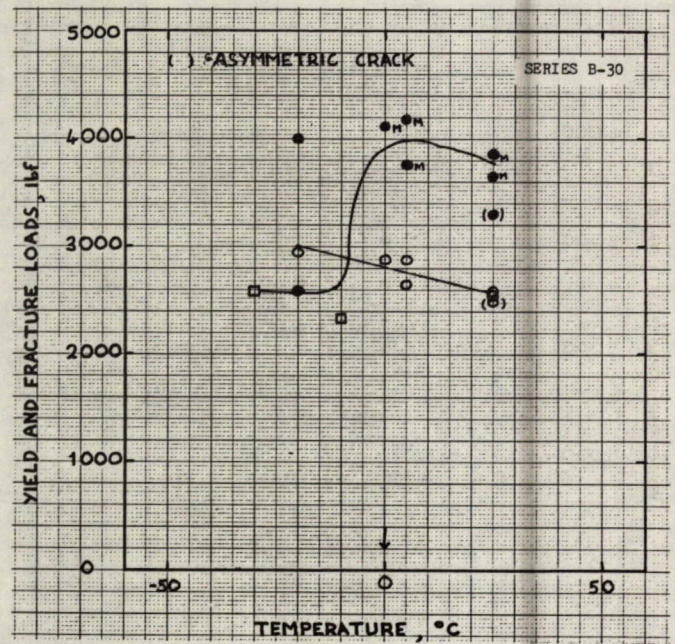
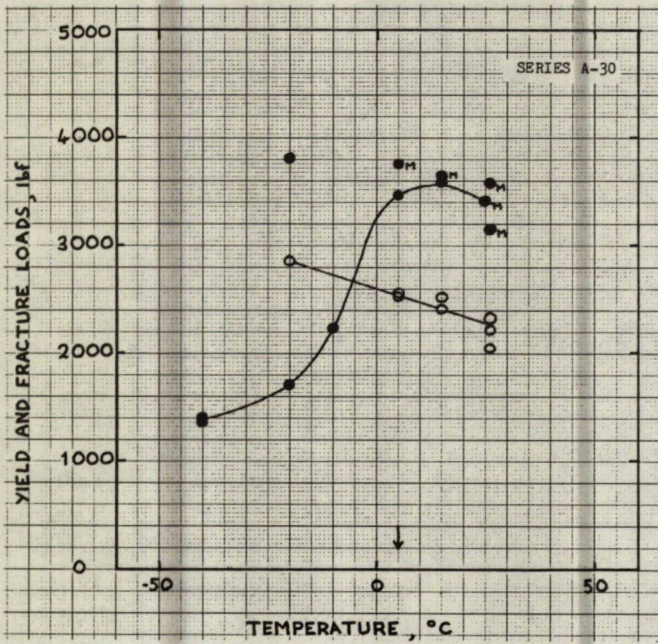




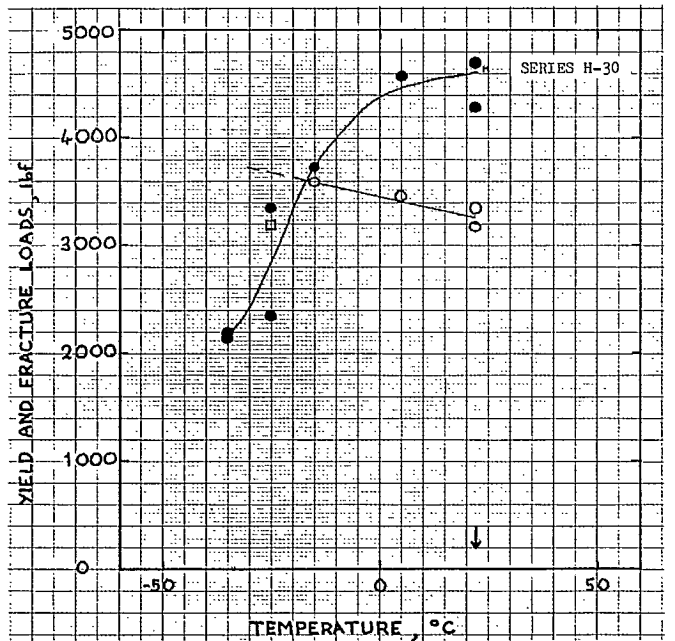
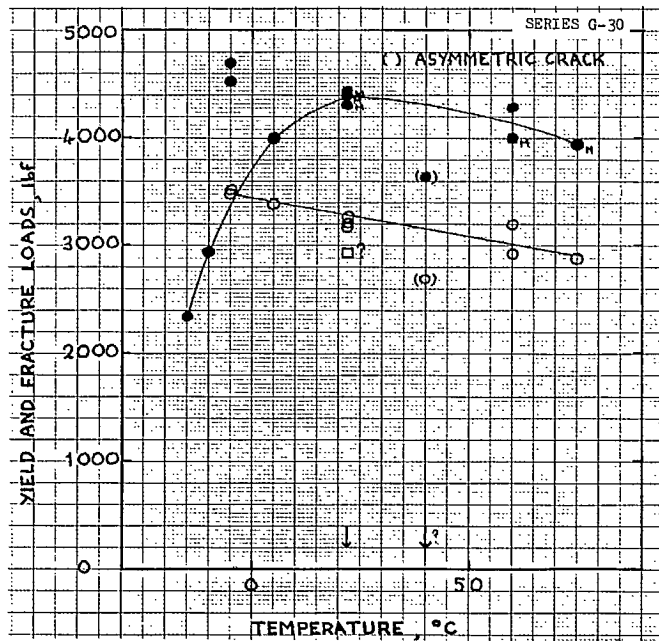
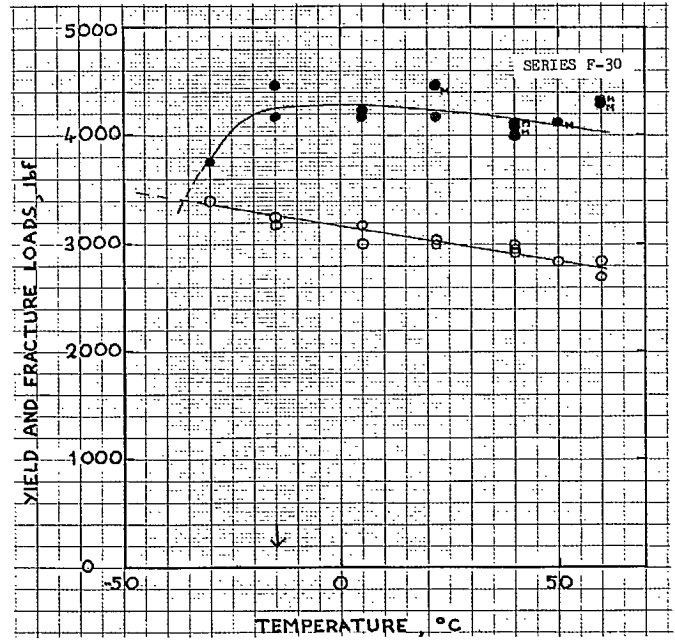
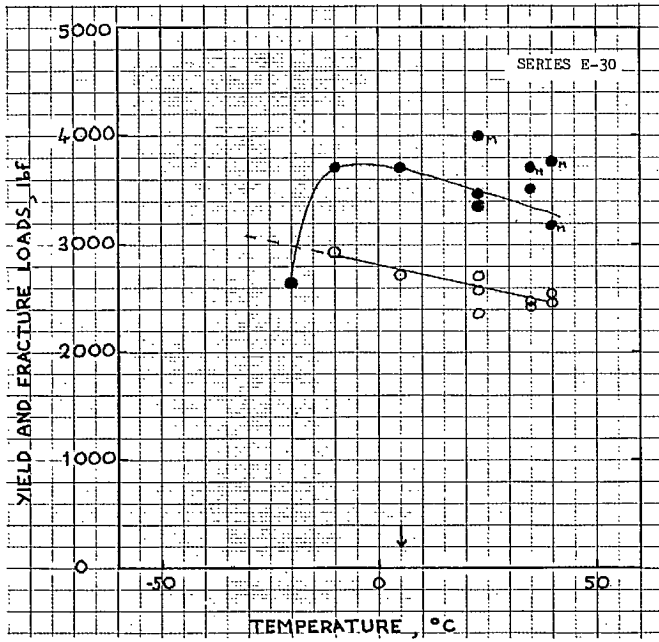




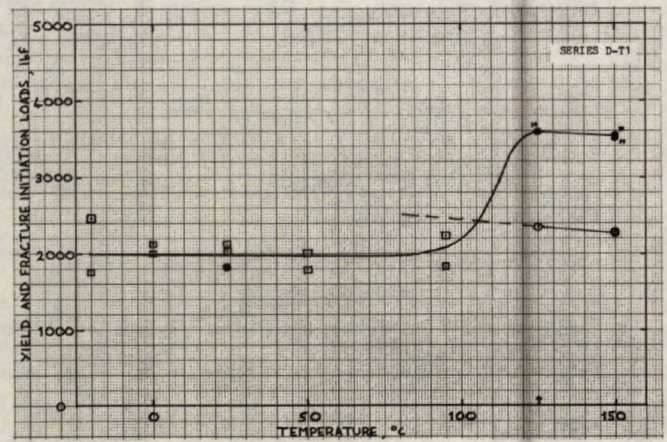
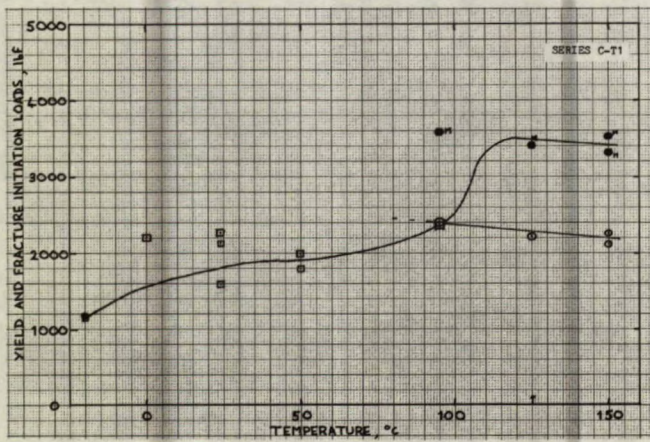
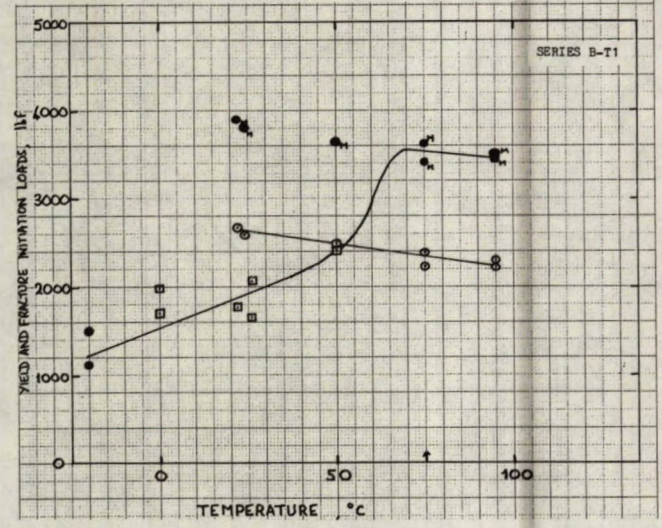
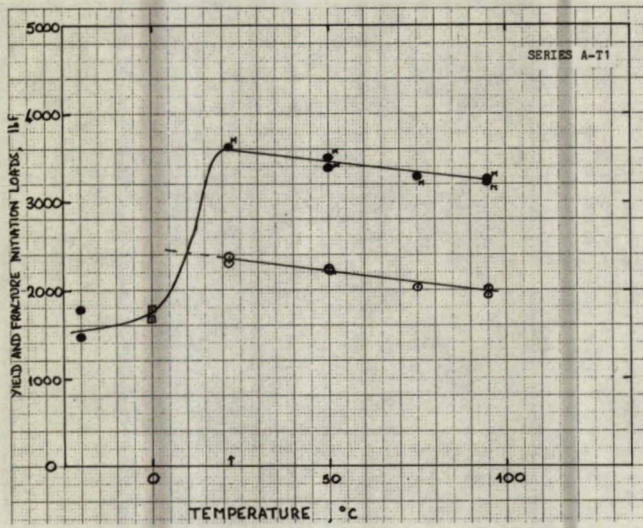




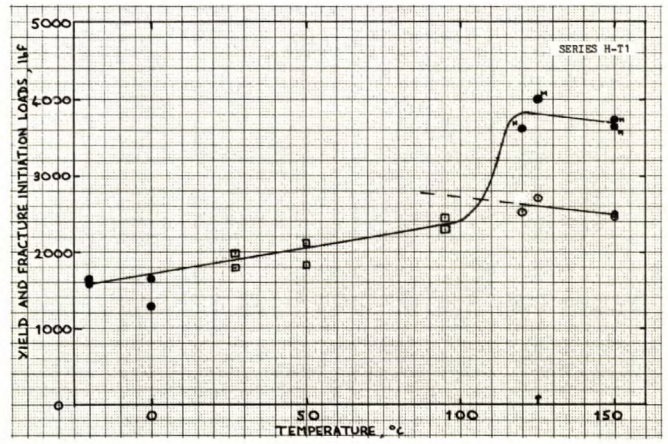
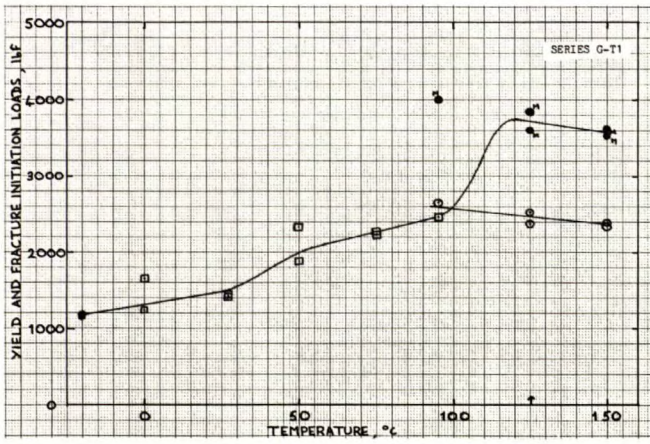
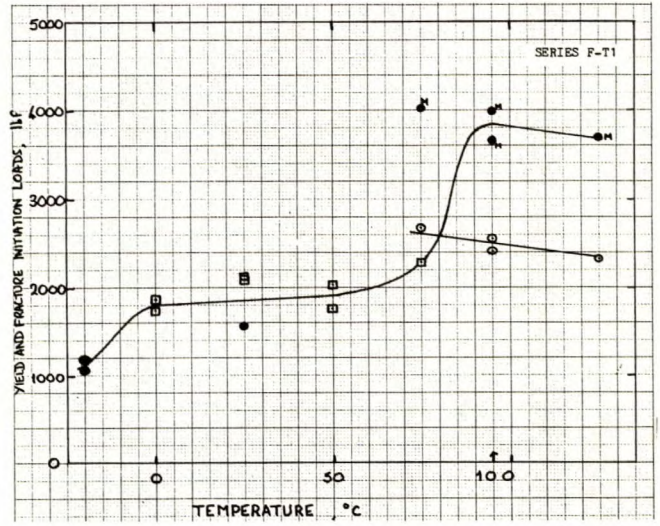
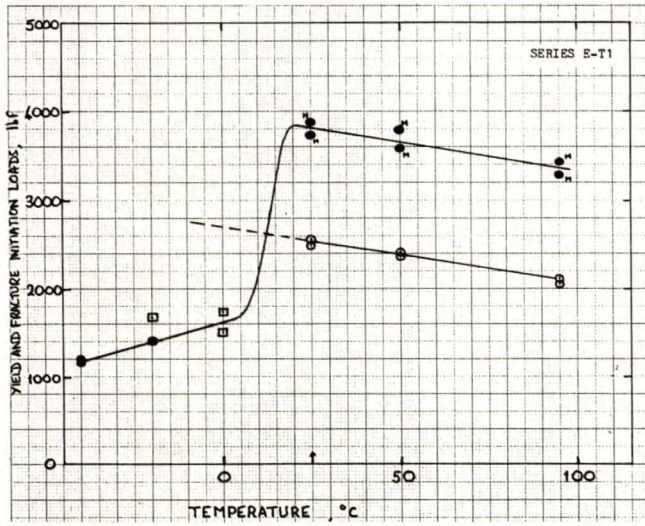




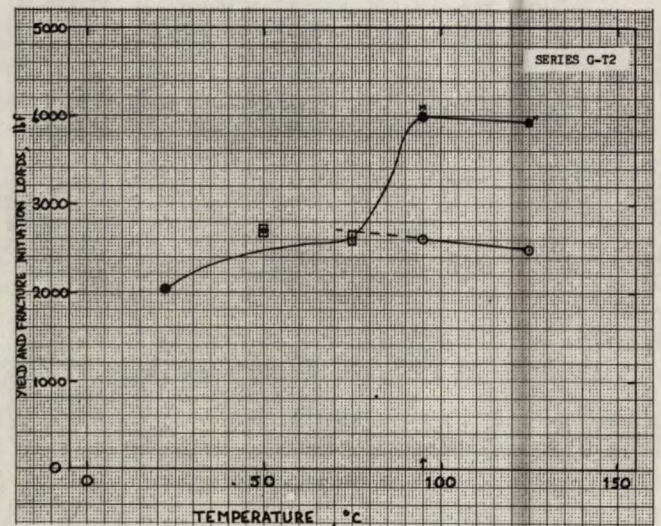
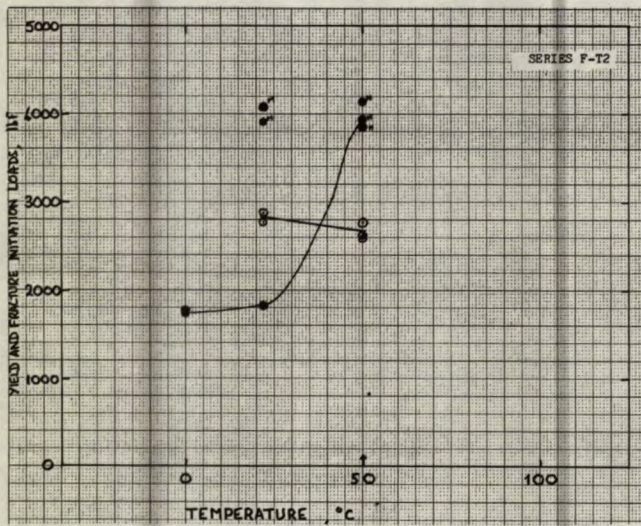
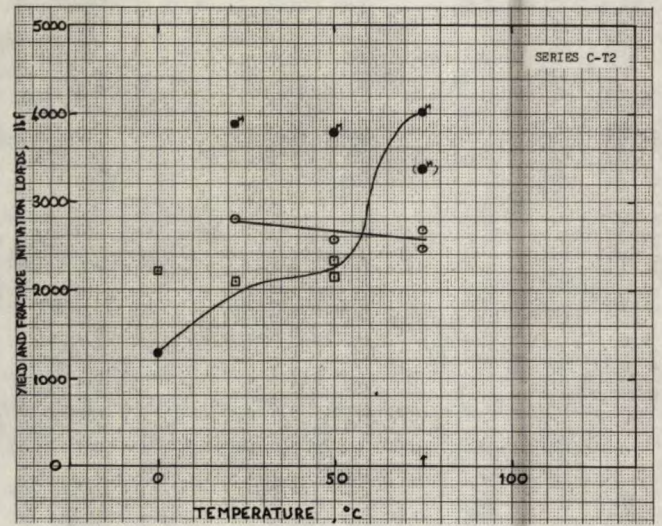
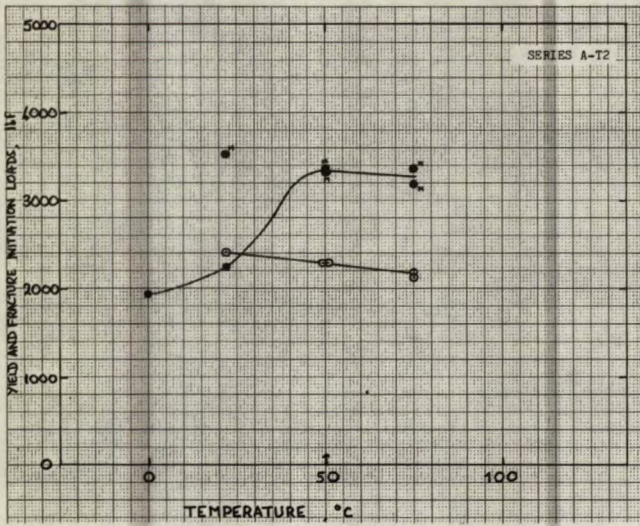




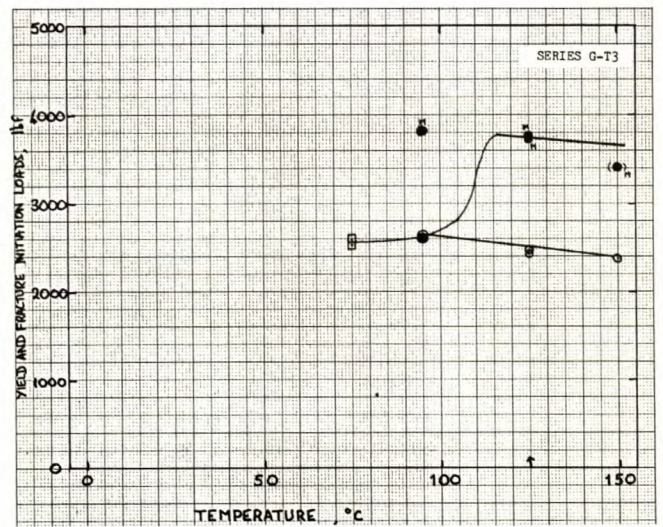
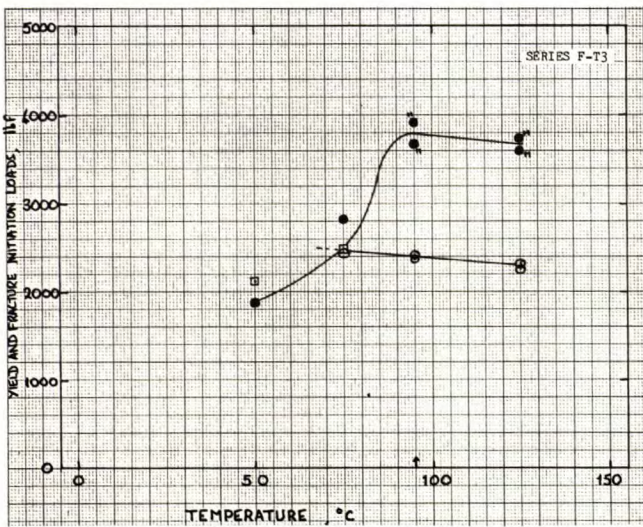
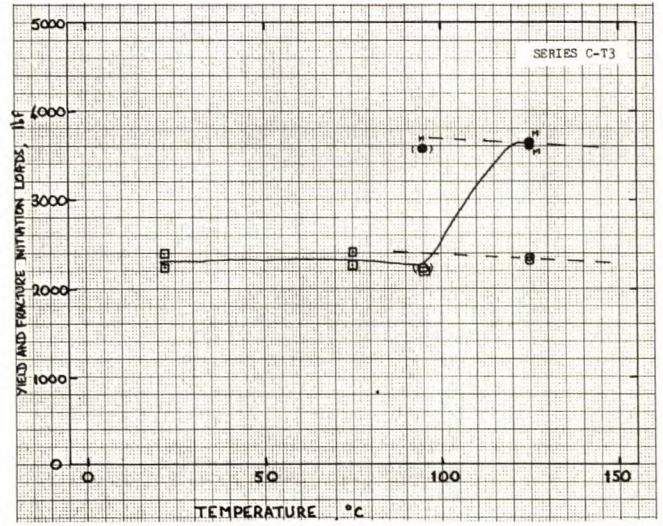
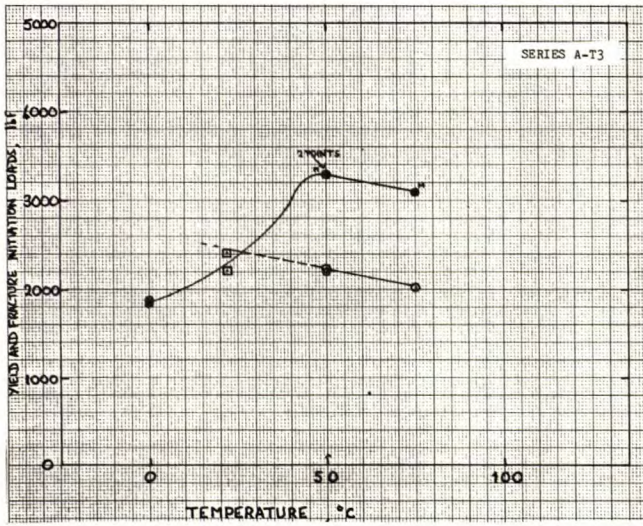














#### CANMET REPORTS

Recent CANMET reports presently available or soon to be released through Printing and Publishing, Supply and Services, Canada (addresses on inside front cover), or from CANMET Publications Office, 555 Booth Street, Ottawa, Ontario, K1A 0G1:

Les récents rapports de CANMET, qui sont présentement disponibles ou qui ce seront bientôt peuvent être obtenus de la direction de l'Imprimerie et de l'Édition, Approvisionnement et Services, Canada (adresses au verso de la page couverture), ou du Bureau de Vente et distribution de CANMET, 555 rue Booth, Ottawa, Ontario, K1A 0G1:

- 78-4 Thermal hydrocracking of Athabasca bitumen: Computer simulation of feed and product vaporization; D.J. Patmore, B.B. Pruden and A.M. Shah;  
Cat. no. M38-13/78-4, ISBN 0-660-10021-5; Price: \$1.75 Canada, \$2.10 other countries.
- 78-7 Mine dust sampling system - CAMPEDS; G. Knight;  
Cat. no. M38-13/78-7, ISBN 0-660-10211-0; Price: \$3.50 Canada, \$4.20 other countries.
- 78-12 CANMET review 1977-78; Branch annual report;  
Cat. no. M38-13/78-12, ISBN 0-660-10143-2; Price: \$2.25 Canada, \$2.70 other countries.
- 78-16 Fly ash for use in concrete part II - A critical review of the effects of fly ash on the properties of concrete; E.E. Berry and V.M. Malhotra;  
Cat. no. M38-13/78-16, ISBN 0-660-10129-7; Price: \$2.25 Canada, \$2.70 other countries.
- 78-20 Comparison of thermal hydrocracking with thermal cracking of Athabasca bitumen at low conversions; R.B. Logie, R. Ranganathan, B.B. Pruden and J.M. Denis;  
Cat. no. M38-13/78-20, ISBN 0-660-10182-3; Price: \$1.25 Canada, \$1.50 other countries.
- 78-21 Ceramic clays and shales of the Atlantic Provinces; K.E. Bell, J.G. Brady and L.K. Zengals;  
Cat. no. M38-13/78-21, ISBN 0-660-10214-5; Price: \$3.00 Canada, \$3.60 other countries.
- 78-22 Radiochemical procedures for determination of selected members of the uranium and thorium series; Edited and compiled by G.L. Smithson;  
Cat. no. M38-13/78-22, ISBN 0-660-10081-9; Price: \$4.25 Canada, \$5.10 other countries.
- 78-26 Effect of hydrocracking Athabasca bitumen on sulphur-type distribution in the naphtha fraction; A.E. George, B.B. Pruden and H. Sawatzky;  
Cat. no. M38-13/78-26, ISBN 0-660-10216-1; Price \$1.25 Canada, \$1.50 other countries.
- 78-30 Reduction rates of iron ore-char briquets used in cupola-smelting; J.F. Gransden, J.T. Price and N.J. Ramey;  
Cat. no. M38-13/78-30, ISBN 0-660-10215-3; Price: \$1.25 Canada, \$1.50 other countries.
- 78-31 Coal associated materials as potential non-bauxite sources of alumina; A.A. Winer and T.E. Tibbetts;  
Cat. no. M38-13/78-31, ISBN 0-660-10217-X; Price: \$1.25 Canada, \$1.50 other countries.